UNIVERSITY OF OKLAHOMA

GRADUATE COLLEGE

COMPUTATIONAL ANALYSIS OF FLUID FLOW, HEAT TRANSFER, AND PHASE CHANGE IN CAPILLARY CHANNELS

A DISSERTATION

SUBMITTED TO THE GRADUATE FACULTY

in partial fulfillment of the requirements for the

Degree of

DOCTOR OF PHILOSOPHY

By

MOHAMMAD NAGHASHNEJAD
Norman, Oklahoma
2021

COMPUTATIONAL ANALYSIS OF FLUID FLOW, HEAT TRANSFER, AND PHASE CHANGE IN CAPILLARY CHANNELS

A DISSERTATION APPROVED FOR THE
SCHOOL OF AEROSPACE AND MECHANICAL ENGINEERING

BY THE COMMITTEE CONSISTING OF

Dr. Hamidreza Shabgard, Chair

Dr. Feng C. Lai

Dr. Dibbon K. Walters

Dr. Jivtesh Garg

Dr. Dimitrios V. Papavassiliou

This dissertation is dedicated to my dear parents, whose love and support have always been unconditional and enthusiastic.

ACKNOWLEDGEMENTS

First and foremost, I would like to express my sincere gratitude to my academic supervisor, Prof. Hamidreza Shabgard, who has provided invaluable guidance, insightful advice, and consistent support throughout my Ph.D. program.

I acknowledge Prof. Feng C. Lai, Prof. Dibbon K. Walters, Prof. Jivtesh Garg, and Prof. Dimitrios V. Papavassiliou to participate on my Ph.D. committee and contribute to my dissertation. Special thanks to Prof. Theodore L. Bergman for his precise comments and commitment to be a great coauthor of my publications. It was an honor for me to have his name as a coauthor on my papers.

I am grateful to the University of Oklahoma's School of Aerospace and Mechanical Engineering, the Dolese Teaching Fellowship, and the Jim and Bee Close Scholarship for their longstanding and gracious financial support.

In particular, I would like to express my thanks and appreciation to Farzaneh Family for their financial support and generous scholarships.

I am thankful to the School of Aerospace and Mechanical Engineering staff members who have always been nice, supportive, and helpful.

I would like to express my sincere regards and thanks to all my fantastic friends and schoolmates at OU and elsewhere, who enriched my life immensely not only when things were going well but also during tough times. Most of all, I give my special thanks to Dr. Mahyar Pourghasemi and Dr. Mehdi Famouri for their helpful discussions, constant encouragement, and generous help at various stages of my research work.

Last but not least, I truly appreciate the perpetual support and blessing of my father (Mr. Hossein Naghashnejad) and my mother (Mrs. Khadijeh Nozari), which reinforced my determination throughout my Ph.D. journey thousands of miles being away from home over the past years. Even to think of thanking them is to trivialize all they have done for me. My profound debt to them, therefore, remains silent and unacknowledged. Also, I am grateful to the rest of my family members for believing in me and their unconditional love and support at all stages of my life. Despite the distance, they always knew how to strengthen me and help me achieve my goals. Thanks for always being by my side.

TABLE OF CONTENTS

LIST OF TABLES

LIST OF FIGURES

LIST OF SYMBOLS

A	Surface area (m^2)
Ag	Silver
c_p	Specific heat at constant pressure (J/kg·K)
F	Force (N)
g	Gravitational acceleration (m/s^2)
$\mathbf{g}$	Gravity vector (m/s^2)
h	Capillary height (m)
h_{fg}	Latent heat of vaporization (J/kg)
j	Interfacial mass flux ($kg/s \cdot m^2$)
k	Thermal conductivity (W/m·K)
K	Curvature of the liquid-gas interface
M_w	Molecular mass (kg/kmol)
$\mathbf{n}$	Outward normal unit vector
$\hat{n}$	Normal unit vector
N	Number of cells along the channel width
NOA	Normalized oscillation amplitude $NOA = 2(h_{max,i} - h_{min,i})/\lvert h_{max,i} + h_{min,i} \rvert$
p	Pressure (Pa)
p^*	Dimensionless capillary pressure
p_{recoil}	Recoil pressure (Pa)
$PTFE$	Teflon
q_{cond}	Conduction heat rate (W)

$q"$	Heat flux (W/cm^2)
R_u	Universal gas constant (J/mol·K)
r	Distance (m)
S_{mass}	Mass source term (kg/m^3·s)
t	Time (s)
T	Temperature (K)
$Theor$	Theoretical
V	Velocity (m/s)
$\mathbf{V}_m$	Mesh velocity vector (m/s)
V_{cell}	Computational cell volume (m^3)
w	Wall spacing (m)
w^*	Dimensionless channel width $w^* = x/w$
x	x-coordinate
x^*	Dimensionless channel width
y	y-coordinate

Greek symbols

α	Accommodation coefficient
Δ	Difference
ε	Volume fraction
Γ	Interface of computational subdomains
θ	Contact angle between liquid and solid surface (°)
μ	Dynamic viscosity (kg/m·s)
ρ	Density (kg/m^3)

σ	Liquid-gas surface tension (N/m)
Ω	Computational sub-domain

Subscripts

0	Initial
avg	Average
b	Boundary
cap	Capillary
$cond$	Conduction
e	Equilibrium state
evp	Evaporation
g	Gas
int	Interface
i	Counter for capillary height peak or valley
l	Liquid
m	Mesh
max	Maximum
min	Minimum
mr	Related to mass removal
$node$	Computational node
ref	Referential domain (moving with the dynamic mesh)
sat	Saturated
ss	Steady state
sup	Superheated

v	Vapor

ABSTRACT

The fluid mechanics and heat transfer associated with capillary-driven flows are of great interest for modeling transport phenomena in micro/miniature devices. Currently, a deeper understanding of this area is necessary for the design of more effective products. The primary objective of this dissertation is to develop a novel computational fluid dynamics model to study the dynamics of meniscus formation, capillary flow, heat transfer, and phase change between vertical parallel plates. To do so, an arbitrary Lagrangian-Eulerian (ALE) approach is employed to predict and reconstruct the shape of the meniscus with no need to employ implicit interface tracking schemes. The developed model is validated by comparing the equilibrium capillary height and meniscus shape with those predicted by available theoretical models. The model was used to predict the capillary flow of water in hydrophilic (silver) and hydrophobic (Teflon) vertical channels with wall spacings ranging from 0.5 mm to 3 mm. It is shown that the computational model accurately predicts the capillary flow regardless of the channel width, whereas the theoretical models fail at relatively large wall spacings. The model captures several important hydrodynamic phenomena that cannot be accounted for in the theoretical models, including the presence of developing flow in the entrance region, time-dependent formation of the meniscus, and the inertial effects of the liquid in the reservoir.

In the next step, the previously developed ALE model was extended to directly track the formation and evolution of the evaporating meniscus during spontaneous liquid penetration within a capillary channel. The two-dimensional time-dependent conservation equations for mass, momentum, and energy were solved in a finite-volume

framework implemented on a moving and deforming grid. The sharp interface tracking method developed here enables direct access to the flow variables and transport fluxes at the meniscus with no need for averaging techniques. The model was validated by comparing the predicted dynamic response of the capillary height subject to interfacial evaporation against theoretical results. The effects of wall spacing and liquid superheat on the capillary flow, and the evaporation rate were studied. It was found that thermal diffusion adjacent to the meniscus has a critical effect on the evaporation rate, and neglecting it leads to significant overprediction of the evaporation rate. Results show that, in general, the inclusion of evaporation causes a reduction of the liquid column height compared to the non-evaporating case. It was also observed that the equilibrium capillary height is inversely proportional to the liquid superheat. Analyses of the transient regime show that evaporation tends to dampen the oscillatory flow regime compared to the non-evaporating meniscus case.

CHAPTER 1: INTRODUCTION

1.1 Background

Capillary-driven flows play a significant role in many natural and engineering systems. Examples include water transport and transpiration in plants, capillary transport of groundwater in the field of hydrology, two-phase heat-transfer devices such as heat pipes, electronics cooling, and propellant management devices, as shown in Fig. 1.1. Although a large amount of research has been carried out to study capillary transport, there is still a lack of fundamental understanding of the complex physical phenomena involved. The broad range of applications and the various physical phenomena involved has led researchers from various disciplines such as mathematics, physics, mechanical engineering, chemical engineering, material science, and biology to study the capillary flow and heat transfer processes. In the following, the fundamental phenomena involved in the capillary flow process are reviewed.

1.2 Fundamentals of Wetting and Capillarity

Capillary penetration/depression refers to the spontaneous liquid rise/fall in a porous medium due to capillary action. The forces that lead to the liquid flow result from the free energies of the interfaces. It is noted that the interfaces are deformable and are free to change their shape or surface area in order to minimize the total surface energy.

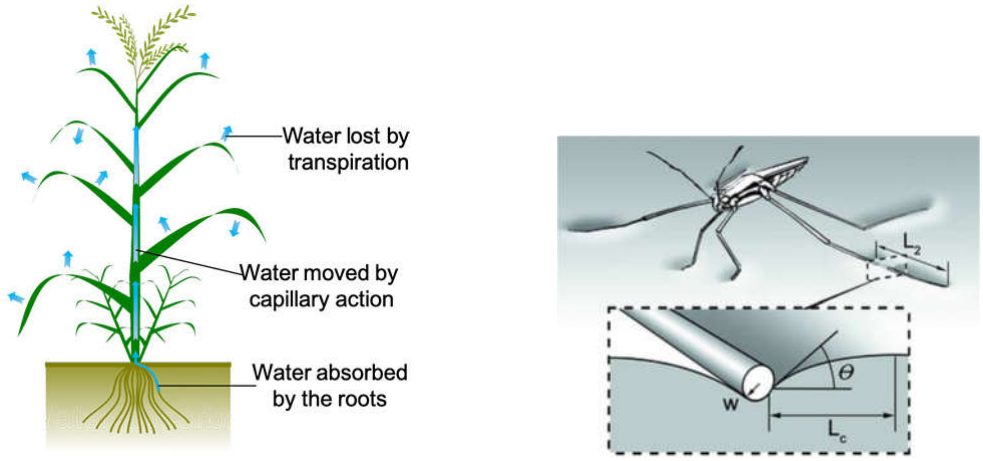

Fig. 1.1 Examples of capillary action in natural and engineering systems: (a) water transport in plants, (b) a static strider resting on the water free-surface and the curvature force due to surface distortion which bears the strider's weight [1], (c) liquid flow in heat pipes, (d) membrane distillation [2], and (e) ink-jet printing [3].

1.2.1 Liquid-Gas Interface and Surface Tension

The interfacial region is a surface between two homogeneous phases of matter in a distinct physical state of solid, liquid, or gaseous. The interface is a thin layer that exhibits different thermophysical properties from those of the bulk material in the gaseous, liquid or solid states. Thus, if interfaces are considered explicitly, new properties such as interfacial surface tension appear in the classical thermodynamic description of equilibrium state. It should be noted that even though the amount of matter in interfacial regions is negligible, the interfacial phenomena can influence the dynamic behavior of flow systems significantly. An interface is mathematically treated as a geometric surface in tension for flows with free boundaries such as capillary flows. Based on the equilibrium surface tension considerations, the normal component of fluid stress (pressure) is not continuous along a curved interface; however, the shear stress is continuous [4].

Cohesion between molecules in liquids, as intermolecular force which attracts the molecules of a liquid towards one another, originates from various forces. Unlike solid molecules that are limited to move about a fixed point, liquid molecules can move in such a way as to minimize the liquid surface. As illustrated in Fig. 1.2, the molecules inside the liquid, far away from the liquid surface, are subject to equal attractions in all directions by cohesive forces. However, the liquid molecules adjacent to the liquid-gas interface have less neighboring liquid molecules and are exposed to a net attraction force into the liquid phase. It is noted that the liquid molecules at the surface are attracted by the neighboring gas molecules; however, this attractive force is significantly smaller than the force exerted by other liquid molecules. Surface tension is

often described as energy per unit area, but it is also expressed in units of force per length [4,5].

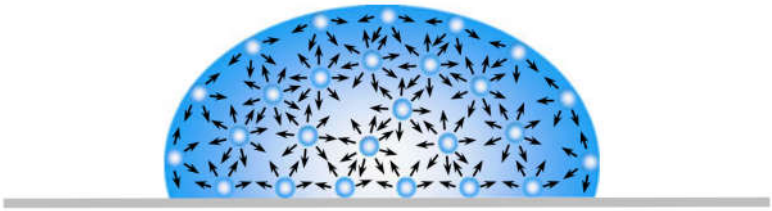

Fig. 1.2 Cohesive forces between molecules within a liquid drop and at the surface [6].

1.2.2 Contact Angle

If we consider a liquid drop placed on a smooth flat horizontal solid surface as shown in Fig. 1.3, a three-phase boundary line is formed where liquid, solid, and gas phases meet.

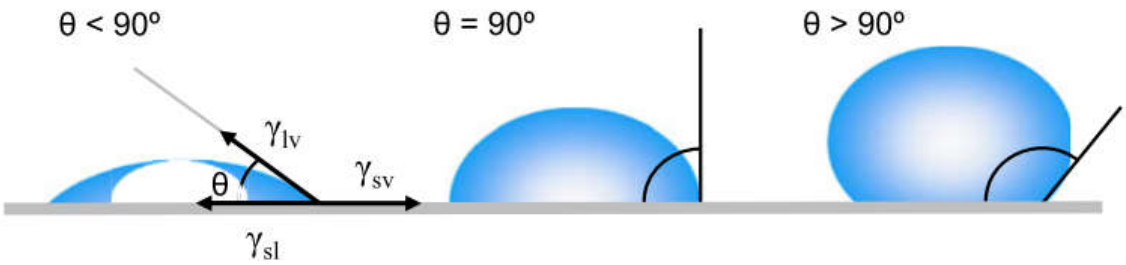

Fig. 1.3 Contact angles shown by a liquid drop on a smooth solid surface [6].

The liquid might remain as a single drop at equilibrium, forming a finite angle, θ, between the solid-liquid and liquid-gas interfaces. The contact angle is a quantitative measure of wetting of a solid by a liquid. It is determined as the angle between the tangent to the liquid-gas interface and the tangent to the solid-liquid interface and measured through the liquid. For the first time in 1805, the basic equation for the contact angle on an ideal (smooth, homogeneous, and insoluble) solid substrate was

proposed by Thomas Young [7]. *Young's equation* establishes a balance between the horizontal components of the interfacial force:

$$cos\theta = \frac{\gamma_{sv} - \gamma_{sl}}{\gamma_{lv}} \tag{1.1}$$

where the thermodynamic parameter γ is the surface tension and the subscripts sv, sl, and lv refer to the solid-gas, solid-liquid, and liquid-gas interfaces, respectively, and θ is the contact angle.

Regarding the contact angle value, liquids can be classified as *completely (or perfectly) wetting* ($\theta = 0°$), *partially wetting* ($0° < \theta < 90°$), or *nonwetting* ($90° < \theta < 180°$) [8]. Moreover, contact angles are not only limited to the liquid-vapor interface on a solid surface. They are also applicable to the liquid-liquid interface on a solid.

1.2.3 Rate of Liquid Rise in a Capillary Tube

When a narrow tube is brought in contact with a completely wetting liquid, some of the liquid rises within the tube until an equilibrium state is reached, as shown in Fig 1.4.

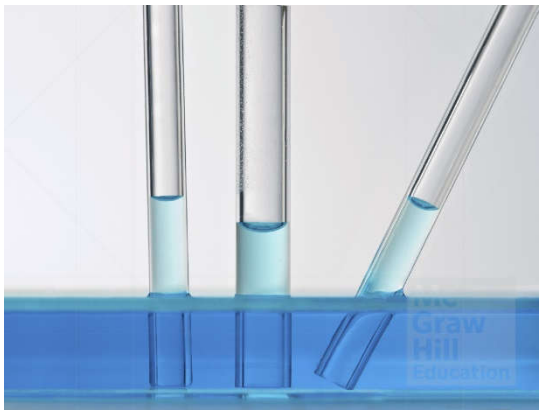

Fig. 1.4 Liquid rise in capillaries.

The fundamental expression for pressure difference across the curved liquid-gas interface due to capillary forces known as the *Young-Laplace equation* [9] is:

$$p_{cap} = p_v - p_l = \gamma\left(\frac{1}{r_1} + \frac{1}{r_2}\right) = \gamma(\mathrm{K}_1 + \mathrm{K}_2) \tag{1.2}$$

where, p_{cap} is the capillary pressure across the liquid-gas interface, γ is the surface tension of the liquid, r_1 and r_2 are the principal radii of curvature of the meniscus, and K_1 and K_2 are curvatures of the meniscus. A specific type of interface condition where the interface is curved is called *meniscus*. In other words, the Young-Laplace equation provides a relation between the curvature of a meniscus and the associated pressure jump across it. If the liquid wets the capillary tube inner surface, a concave liquid-gas interface will form. In the case of circular cross-section capillary with a very small radius, when the liquid completely wets the solid surface, and the two curvature radii are equal, a hemispherical interface is formed, and Eq. (1.2) is reduced to:

$$p_{cap} = \frac{2\gamma}{r} = 2\gamma\mathrm{K} \tag{1.3}$$

where *r* is the radius of the capillary.

In liquid-solid systems where the liquid is not completely wetting, Eq. (1.3) is expressed as:

$$p_{cap} = \frac{2\gamma cos\theta}{r} \tag{1.4}$$

where θ is the equilibrium (Young) contact angle.

In a vertical capillary, if *h* is the net height of the meniscus with respect to the liquid surface in the reservoir, the net pressure difference (Δp) that drives penetration is the capillary pressure minus the hydrostatic pressure of the liquid column in the capillary.

$$\Delta p = p_{cap} - \Delta\rho g h \tag{1.5}$$

where $\Delta\rho$, g, and h are the difference between the density of the liquid and that of gas, gravitational acceleration, and meniscus height, respectively.

Combining Eqs 1.4 and 1.5, and neglecting the density of gas due to the large density differences between the gas and liquid, the equilibrium height of liquid in the capillary is achieved when the net driving pressure difference is zero:

$$h_e = \frac{2\gamma cos\theta}{\rho g r} \tag{1.6}$$

where ρ is the liquid density and h_e is the equilibrium capillary height.

Capillary penetration phenomena occur when the liquid wets the capillary channel wall ($\theta < 90°$). If the liquid is nonwetting ($90° > \theta$), capillary depression occurs, which indicates that the capillary rise h_e obtained from Eq. (1.6) is negative, as illustrated in Fig. 1.5.

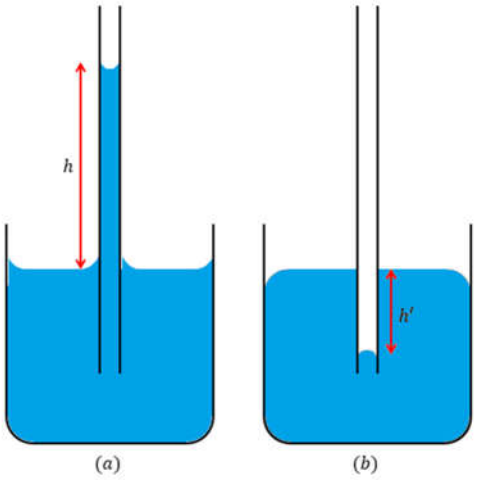

Fig. 1.5 (a) Capillary penetration in a hydrophilic capillary, (b) capillary depression in a hydrophobic capillary.

Generally, solid materials exhibit two different behaviors in interaction with water and are classified as hydrophilic or hydrophobic [10]. Hydrophilic materials are often characterized by their affinity for water; water completely spreads over the surface and a maximum contact area is achieved. On the other hand, hydrophobic materials repel water, causing droplets to form. The shape of the water droplet on a flat solid surface, specifically the contact angle between the edge of the water droplet and the surface beneath it, can be considered as a criterion for hydrophilic or hydrophobic properties of a material.

A hydrophilic surface is one on which a water droplet forms a contact angle smaller than 90° ($\theta_{hydrophilic} < 90°$), while on a hydrophobic surface, a droplet of water forms a contact angle greater than 90° ($\theta_{hydrophobic} > 90°$). Furthermore, if the contact angle is less than 5°, the surface is called super-hydrophilic ($\theta_{superhydrophilic} < 5°$), whereas surfaces made of materials such as polymer where the contact angles are between 150° and 180° are called super-hydrophobic ($150° < \theta_{superhydrophobic} < 180°$) [11].

In order to determine the hydrodynamic behavior and the corresponding flow rate in a capillary tube, Hagen-Poiseuille's law for viscous laminar flow through a pipe can be employed as a simplified approach. The resistance to air displacement can also be neglected due to the large difference between the viscosity of liquid and that of air. The volumetric flow rate of liquid in the tube can be expressed as:

$$\frac{dV}{dt} = \frac{\Delta p \pi r^4}{8\mu L} \tag{1.7}$$

where $\frac{dV}{dt}$ denote the volume flow rate, Δp is the pressure drop across the liquid column, r is the tube radius, μ is the dynamic viscosity of the liquid, and L is the length of tube. For vertical capillaries, combining Eqs. 1.5 and 1.7 an ordinary differential equation is derived as follows:

$$\frac{dh}{dt} = \frac{r^2}{8\mu}\left(\frac{\Delta p}{h} - \rho g\right) \tag{1.8}$$

Solving the above differential equation gives an expression for the height of liquid rise into a capillary tube:

$$\frac{h}{h_e} - ln\left(1 - \frac{h}{h_e}\right)^{-1} = -\frac{r^2 \rho g}{8\mu h_e} t \tag{1.9}$$

where t is the time and h is the instantaneous capillary height at time t.

In a particular case, at the early stage of the liquid rise within the capillary tube, when h is much smaller than h_e, the height of the meniscus vs. time can be described by a linear relationship known as the Washburn equation [12]:

$$h = \sqrt{\frac{r\gamma cos\theta}{2\mu} t} \tag{1.10}$$

Equation (1.10) indicates that at short times, the meniscus height is a function of the square root of time.

In capillaries of very small diameter, the viscous, gravity, and surface tension terms may have the same order of magnitude after the early stages of capillary penetration. However, for capillaries of larger diameters, inertia plays an important role, and the assumption of Poiseuille's flow is not valid anymore [13].

1.2.4 Dimensionless Numbers

There are some well-known dimensionless numbers that are frequently used in the analysis of capillary flow, as listed in Table 1.1. In the following equations, v is the liquid velocity.

Table 1.1 Dimensionless numbers for analysis of capillary flow.

Dimensionless number	Relation	Definition
Bond number (Bo)	$\frac{\rho g r^2}{\gamma}$	$\frac{gravity}{surface\ tension}$
Capillary Number (Ca)	$\frac{\mu v}{\gamma}$	$\frac{viscous}{surface\ tension}$
Froude number (Fr)	$\frac{v}{\sqrt{gr}}$	$\frac{inertia}{gravity}$
Galileo number (Ga)	$\frac{g\rho^2 r^3}{\mu^2}$	$\frac{gravity}{viscous}$
Ohnesorge number (Oh)	$\frac{\mu}{\sqrt{r\rho\gamma}}$	$\frac{viscous}{\sqrt{inertia.surface\ tension}}$
Reynolds number (Re)	$\frac{\rho r v}{\mu}$	$\frac{inertia}{viscous}$

1.2.5 Evaporating Meniscus

High heat transfer coefficients, typically associated with the evaporation (or condensation) process in multiphase heat transfer devices are strongly dependent on interfacial resistance. Evaporation is the phase change from the liquid phase to the gaseous phase at a free liquid-gas interface in contrast to boiling, in which the vapor phase is completely surrounded by the liquid phase. During evaporation process, the

flux of liquid molecules escaping to the vapor phase exceeds that of vapor molecules into the liquid phase.

Using the classical kinetic gas theory, the net mass flux at the liquid-gas interface, j, is modelled from the following equation, referred to as the Kucherov-Rikenglaz equation [4]:

$$j = \left(\frac{2\alpha}{2-\alpha}\right)\sqrt{\frac{M_w}{2\pi R_u}}\left(\frac{p_v}{\sqrt{T_v}} - \frac{p_l}{\sqrt{T_l}}\right) \tag{1.11}$$

where α is the accommodation coefficient, M_w is the molecular mass, and R_u is the universal gas constant, and p_l and p_v are the saturation pressures corresponding to T_l and T_v, respectively.

The meniscus temperature is not necessarily equal to the temperature of saturated vapor. The interfacial mass flux j at an evaporating meniscus can be related to the temperature jump across the interface using the concept of *thermal resistance* as follows:

$$K = \frac{T_{int} - T_v}{j} \tag{1.12}$$

where K is the interfacial thermal resistance and $T_{int} - T_v$ is the interfacial temperature jump. Using the Clausius-Clapeyron relation, Eq. (1.11) can be rewritten without pressure terms and the interfacial thermal resistance associated with evaporation can be expressed as:

$$K = \frac{{T_v}^{1.5}}{\alpha \rho_v h_{lv}}\left(\frac{2\pi R_u}{M_w}\right)^{0.5} \tag{1.13}$$

where ρ_v is the vapor density and h_{lv} is the latent heat of evaporation.

1.3 Interface Tracking Approaches

As noted before, a wide range of natural and engineering systems involve interfacial phenomena and capillary flow. Understanding the evolution of capillary flow is critical for the analysis of the transport phenomena in such a system. Numerical simulation of fluid flow problems, including fluid-fluid and/or fluid-solid interfaces, involves several challenges and complexities. One of the major difficulties originates from the fact that the position and shape of the interfaces are time-dependent and may involve heat and/or mass transfer in the case of evaporating menisci. Also, the interfaces evolve and may experience severe deformations that influence the nearby flow and thermal fields. Another challenge is modeling discontinuities in thermophysical properties across the interface, particularly large jumps in density. These moving boundaries play a significant role in the system, so their accurate representation has a great effect on the solution of the problem. In the computational treatment of a moving and/or deforming interface, several substantial points should be addressed, such as the representation of the interface on a finite grid, the time evolution of the interface, and the specification of boundary conditions at the interface. In general, numerical solutions of interfaces can be accomplished by Eulerian (fixed) or Lagrangian (moving) grids. Each method has its own advantages and disadvantages. In the following, different interface capturing/tracking techniques are briefly described, and the selected method for the present work is identified.

1.3.1 Lagrangian Method

In this method, the fluid particles and, consequently, the interface is tracked directly [14]. Lagrangian methods can accurately predict the evolution of the interface; however, they typically have a poor performance when the particle deformations are large. On the other hand, Eulerian methods are suited for modeling large deformations of materials; thus, most computational fluid dynamics codes employ Eulerian techniques.

1.3.2 Volume of Fluid Method (VOF)

The VOF method is one of the most widely used Eulerian techniques to predict multi-phase fluid flow problems. In this method, the Navier-Stokes equations are solved over a fixed grid together with a transient advection equation governing the evolution of the interface function that marks the position of the interface [15,16]. It is assumed that two or more fluids are not interpenetrating. For each phase, a phase indicator function is introduced as the *volume fraction* (ε) of the phase in the computational cell:

$$\varepsilon(x,t) = \begin{cases} 1 & if\ x\ is\ in\ the\ primary\ phase \\ 0 & if\ x\ is\ in\ the\ secondary\ phase \end{cases} \tag{1.14}$$

In each computational cell, the volume fractions of all phases sum to unity. When the volume fraction of a particular phase has a value between 0 and 1 in a computational cell, that cell can be regarded as an interfacial cell. Several special interpolation schemes have been developed to eliminate the numerical diffusion at an interface that results in loss of resolution and inaccurate or diverging solutions. Figure 1.6 shows two of the most widely used interpolation schemes: the *donor-acceptor scheme* [15], in which the interface in each cell is decomposed into either horizontal or vertical

segments, and the *piecewise linear reconstruction scheme* [17] which is a more refined interface interpolation technique and predicts the slope of the interface in each computational cell based on the gradient of the volume fraction function in neighboring cells.

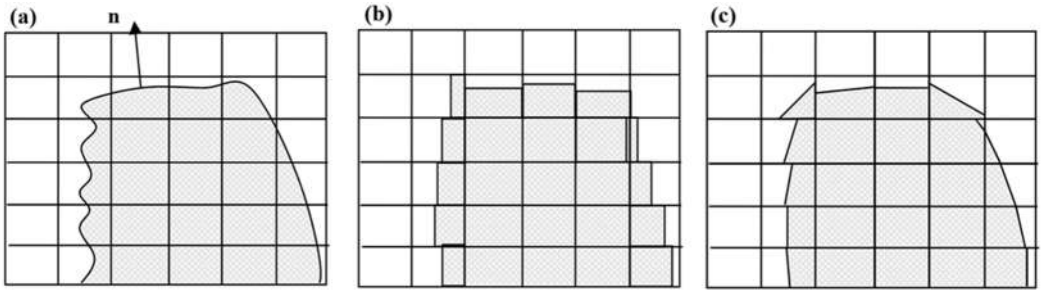

Fig. 1.6 Schematic of the computational treatment of the phase interface using various interpolation schemes in the VOF method (a) an actual interface, (b) using the donor-acceptor technique, and (c) using a piecewise linear reconstruction technique [4].

1.3.3 Level-Set Method

Among the interface modeling methods, the VOF method and the level-set method [18,19] are the most popular ones. While the VOF method benefits from the conservation of mass, the level-set technique has many advantages, such as accurate computation of surface normals and curvature. In this method, which belongs to the family of fixed grid methods, a level-set function is a signed-distance function $\phi(x,t)$, that represents the shortest distance to the interface, Γ:

$$|\phi(x,t)| = |x - x_\Gamma| \quad \rightarrow \quad \begin{cases} \phi > 0 \ \ is\ liquid \\ \phi = 0 \ \ is\ interface \\ \phi < 0 \ \ is\ gas \end{cases} \tag{1.15}$$

where x_Γ is the location on the interface that has the shortest distance to x, and ϕ has positive values on one side of the interface and negative values on the other side. So, the

interface is represented as an iso-surface of the signed-distance function, ϕ, of value zero. As such, $\phi > 0$ denotes liquid and $\phi < 0$ is gas. Fig. 1.7 depicts a comparison between two main interface modeling methods in the Eulerian framework, namely, the VOF method and the level set method.

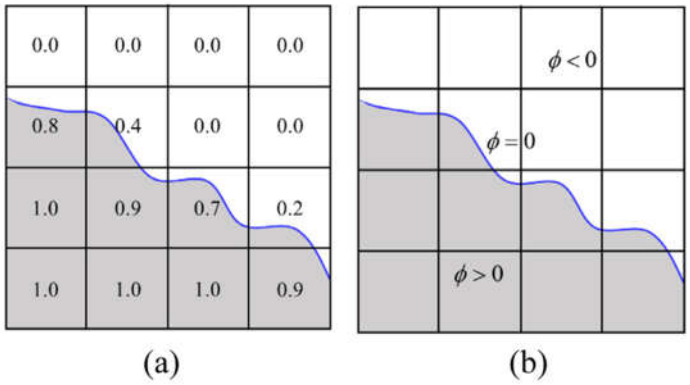

Fig. 1.7 Schematic representation of three interface modeling approaches (a) volume-of-fluid method (the numbers in cells denote the liquid volume fraction), (b) level set method [20].

1.3.4 Arbitrary Lagrangian-Eulerian (ALE) Method

Due to the drawbacks of using only the Lagrangian method or purely Eulerian method, generalized kinematical descriptions of the fluid domain known as arbitrary Lagrangian-Eulerian methods that integrate both Lagrangian and Eulerian advantages were developed [21,22]. Among the available moving-mesh methods, the ALE method is the most popular one and has been widely employed in flows with moving boundaries and interface computations. In this technique, as the shape of the fluid domain changes due to the movement and/or deformation of the interface, the grid moves to track the interface, provide the fine grid resolution adjacent to the interface, and adapt itself to the

change of shape. This occurs through a process known as the mesh update method. The mesh update process consists of moving the grid for as long as possible and remeshing as required for maintaining the quality of the computational element and minimizing the frequency of remeshing. One of the main advantages of the ALE methods is that the boundary condition can be accurately imposed since the moving boundary is exactly aligned with a control surface of the computational mesh.

In this work, because of the desirable capabilities and attractive features that are not available easily or at all in the fixed-grid methods, the ALE method is employed to track the dynamic behavior of the liquid-vapor interface. Interestingly, moving the fluid domain grid to track a fluid-vapor interface gives the ability to have better control on the grid resolution adjacent to the interface, high-resolution representation of the boundary layers, and achieve reliable predictions in the critical flow regions where high gradients emerge.

In ANSYS Fluent, application of the ALE method is possible through the “Dynamic Mesh Model” capability to simulate problems with moving boundaries in which the shape of the computational domain changes with time due to the motion of the domain boundaries [23,24]. The dynamic mesh model in ANSYS Fluent uses three main schemes, namely, *smoothing*, *layering*, and *remeshing*. A combination of these schemes can be implemented to overcome the most complicated moving mesh problems, including both rigid and deforming motions of the boundaries. In both cases, using the mesh update methods, the computational nodes are updated at each time step based on the new positions of the boundaries. As such, the dynamic mesh solutions are inherently

transient. In this work, several user-defined functions (UDFs) are developed to describe the motion of the moving zones.

1.4 Fundamentals of the Arbitrary Lagrangian-Eulerian approach

1.4.1 Overview of Lagrangian and Eulerian Approaches

Most of the multiscale problems in computational fluid dynamics are associated with large distortions of the continuum. Generally, there are two classical descriptions of motion, namely, the Lagrangian description and the Eulerian description.

In the Lagrangian approach, which is widely used in solid mechanics, each computational cell follows the associated material particle during motion, as schematically shown in Fig. 1.8. Thus, tracking free surfaces and interfaces between different materials is relatively easy. However, it is not possible to follow large distortions of the computational domain without a frequent remeshing process.

On the other hand, in the Eulerian approach, which is mainly preferred in fluid simulations, a control volume is defined. Flow variables such as pressure, velocity, acceleration, etc., are treated as continuum fields within the control volume. As illustrated in Fig. 1.8, the computational grid is fixed, and the fluid moves with respect to the mesh. Hence, the Eulerian description offers a better capability of handling larger distortions than the Lagrangian description, while precise interface definition and the detailed representation of flow are needed.

The arbitrary Lagrangian-Eulerian approach, as its name indicates, is an attempt to achieve the advantages and combining the best features of both the purely Lagrangian and the purely Eulerian descriptions while minimizing the drawbacks of the mentioned

classical kinematical descriptions. In this approach, the computational nodes can be moved flexibly as the material deforms like the Lagrangian mesh or can be held fixed in space similar to the Eulerian grid or, as shown in Fig. 1.8, can move in some arbitrary manner and provide a continuous rezoning capability. Therefore, this flexibility of mesh offered by the ALE approach allows it to handle severe degradation of the computational mesh while maintaining quite a regular mesh topology of the interface that cannot accommodate via a Lagrangian method [25].

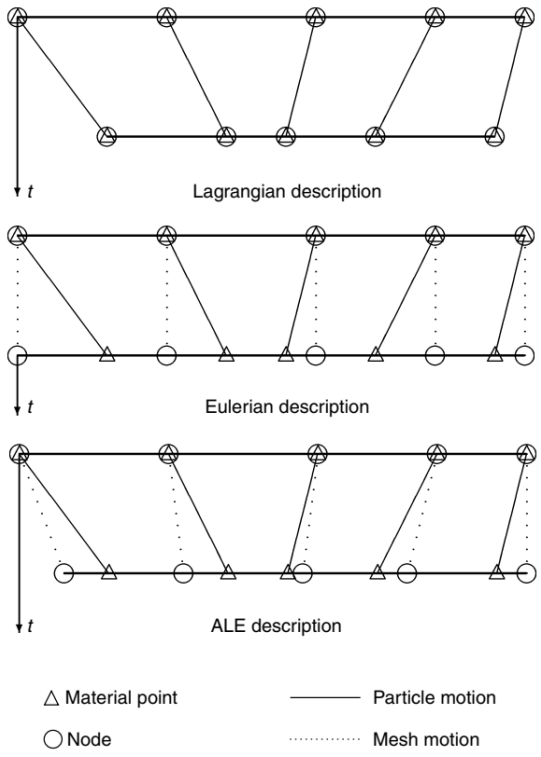

Fig. 1.8 Schematic of Lagrangian, Eulerian, and ALE mesh and particle motion [21].

In continuum mechanics, two domains are widely used, namely the material domain and spatial domain. The former consists of material points, while the latter is made up of spatial points. In the Lagrangian approach, the fluid particles (material points) are

followed as they move through the continuum. The material coordinates X are related to the spatial coordinates x as the material points move. It is defined using a one-to-one mapping φ as:

$$(X, t) \rightarrow \varphi(X, t) = (x, t) \tag{1.16}$$

or

$$(X, t) = \varphi^{-1}(x, t) \tag{1.17}$$

Since the material points coincide with the same grid points during the motion, it is important to keep in mind that the advective effects disappear in the Lagrangian description. Thus, the material derivative reduces to a simple time derivative. In problems involving large material deformations, like the formation of vortices in fluids, the Lagrangian formulation suffers from accuracy losses and a reduction of the explicit critical time step because of excessive distortions of the computational grid. This problem can be tackled with the Eulerian formulation.

The material velocity v at a given computational node is defined as the velocity of the material point coincident at the time t with the considered computational node.

$$v = v(x, t) \tag{1.18}$$

It is noted that in the Eulerian approach, the computational nodes and the material particles are dissociated from each other. Therefore, the Eulerian description includes the advective effect due to the relative motion between the deforming material and the computational mesh.

1.4.2 Kinematical Description of ALE Approach

The arbitrary Lagrangian-Eulerian method is based on three domains, namely, the material configuration (R_X), the spatial configuration (R_x), and the referential or ALE configuration (R_χ). The ALE description introduces a mesh motion independent of the material motion. In the ALE formulation, none of the material configuration or the spatial configuration is considered as the reference. In the referential configuration, the reference coordinates, χ, represent the grid points. The arbitrary movement of the referential domain is computed by a moving mesh formulation or specified in such a way to treat the moving boundaries.

As shown in Fig. 1.9, the referential domain is transferred into the material and spatial domains under the mappings of Ψ and Φ, respectively. The particle motion φ can be written as:

$$\varphi = \phi * \Psi^{-1} \tag{1.19}$$

It is clear that the mappings φ, ϕ, and Ψ are dependent.

The motion of the grid points in the spatial domain can be expressed as the mapping of ϕ from the referential domain to the spatial domain as follows:

$$(\chi, t) \rightarrow \phi(\chi, t) = (x, t) \tag{1.20}$$

So, the mesh velocity is:

$$v_{mesh}(\chi, t) = \left.\frac{\partial x}{\partial t}\right|_{\chi} \tag{1.21}$$

It is noted that both the material or the mesh moves with respect to the spatial domain. Also, we have:

$$(X, t) \rightarrow \Psi^{-1}(X, t) = (\chi, t) \tag{1.22}$$

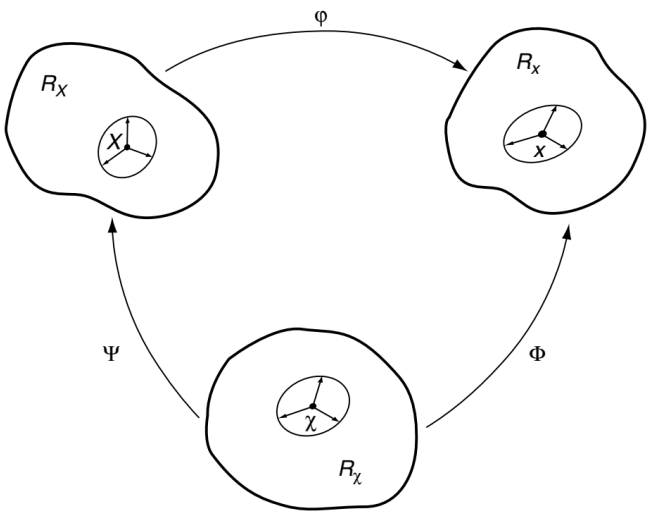

Fig. 1.9 Representation of the material configuration (R_X), the spatial configuration (R_x), and the referential or ALE configuration (Rχ) [21].

The particle velocity, w, in the referential domain is then expressed as:

$$w = \left.\frac{\partial \chi}{\partial t}\right|_X \tag{1.23}$$

Finally, after some mathematical manipulation, the relation between velocities v, v_{mesh}, and w can be achieved as:

$$c = v - v_{mesh} = \frac{\partial x}{\partial \chi} \cdot w \tag{1.24}$$

where c is the relative velocity between the material and the mesh which is called as advective velocity.

1.4.3 Fundamental Equation in ALE Framework

The relation between material and referential time derivatives is called the *fundamental ALE equation*. It is necessary to derive the conservation laws for mass, momentum, and energy in an ALE format.

If a scalar physical quantity is expressed by $f(x,t)$, $f^*(\chi,t)$ and $f^{**}(X,t)$ in the spatial, referential, and material configurations, respectively, the relation between the spatial and material descriptions of the physical quantity can be written as:

$$f^{**}(X,t) = f(\varphi(X,t),t) \tag{1.25}$$

After computation of the gradient of the relation above and block multiplication, a famous equation that relates the material and the spatial time derivatives is achieved:

$$\frac{\partial f^{**}}{\partial t} = \frac{\partial f}{\partial t} + \frac{\partial f}{\partial x} \cdot v \tag{1.26}$$

or

$$\left.\frac{\partial f}{\partial t}\right|_X = \left.\frac{\partial f}{\partial t}\right|_x + v \cdot \nabla f \tag{1.27}$$

If the material and spatial time derivatives are denoted as $\left.\frac{\partial .}{\partial t}\right|_X \equiv \frac{D.}{Dt}$ and $\left.\frac{\partial .}{\partial t}\right|_x \equiv \frac{\partial .}{\partial t}$, Eq. (1.27) can be written as:

$$\frac{Df}{Dt} = \frac{\partial f}{\partial t} + v \cdot \nabla f \tag{1.28}$$

Considering the mapping Ψ in Fig. 1.9,

$$f^{**} = f^* * \Psi^{-1} \tag{1.29}$$

After computation of the gradient of the relation above and block multiplication, the relation between the material and referential time derivatives is achieved:

$$\frac{\partial f^{**}}{\partial t} = \frac{\partial f^*}{\partial t} + \frac{\partial f^*}{\partial \chi} \cdot w \tag{1.30}$$

Using the definition of w, the preceding equation can be written into:

$$\frac{\partial f^{**}}{\partial t} = \frac{\partial f^*}{\partial t} + \frac{\partial f^*}{\partial x} \cdot c \tag{1.31}$$

Finally, the fundamental ALE relation between material and referential time derivatives and the spatial gradient is as follows:

$$\left.\frac{\partial f}{\partial t}\right|_X = \left.\frac{\partial f}{\partial t}\right|_\chi + \left.\frac{\partial f}{\partial x}\right|_x \cdot c = \left.\frac{\partial f}{\partial t}\right|_\chi + c \cdot \nabla f \tag{1.32}$$

In which the advective term c is the relative velocity between the material and reference domains. In the following sections, both the differential and integral ALE forms of the conservation equations for mass, momentum, and energy are derived.

1.4.4 Differential Form of Conservation Equations in ALE Framework

The Eulerian forms of the conservation equations for mass, momentum, and energy are:

Mass: $$\frac{D\rho}{Dt} = \left.\frac{\partial \rho}{\partial t}\right|_x + v \cdot \nabla \rho = -\rho \nabla \cdot v \tag{1.33}$$

Momentum: $$\rho \frac{Dv}{Dt} = \rho \left(\left.\frac{\partial v}{\partial t}\right|_x + (v \cdot \nabla) v \right) = \nabla \cdot \sigma + \rho b \tag{1.34}$$

Energy: $$\rho \frac{DE}{Dt} = \rho \left(\left.\frac{\partial E}{\partial t}\right|_x + v \cdot \nabla E \right) = \nabla \cdot (\sigma \cdot v) + v.\rho b \tag{1.35}$$

where ρ, v, σ, b, and E are the density, the material velocity vector, the Cauchy stress tensor, the specific body force vector, and the specific total energy, respectively. By replacing the material velocity v with the advective velocity c, the ALE differential forms of the conservation equations are obtained:

Mass: $$\left.\frac{\partial \rho}{\partial t}\right|_\chi + c \cdot \nabla \rho = -\rho \nabla \cdot v \tag{1.36}$$

Momentum: $$\rho \left(\left.\frac{\partial v}{\partial t}\right|_\chi + (c \cdot \nabla) v \right) = \nabla \cdot \sigma + \rho b \tag{1.37}$$

Energy: $$\rho\left(\left.\frac{\partial E}{\partial t}\right|_{\chi}+c\cdot\nabla E\right)=\nabla\cdot(\sigma\cdot v)+v.\rho b \tag{1.38}$$

It is noted that the arbitrary motion of the computational mesh is only reflected in the LHS of the above equations.

For time-dependent two-dimensional laminar incompressible flow of a Newtonian fluid with constant thermophysical properties and negligible viscous dissipation and natural convection effects, the conservation equations for mass, momentum, and energy in the ALE framework are:

Mass: $$\nabla\cdot v=0 \tag{1.39}$$

Momentum: $$\rho\left[\left.\frac{\partial v}{\partial t}\right|_{\chi}+((v-v_{mesh})\cdot\nabla)v\right]=-\nabla p+\mu\,\nabla^2 v+\rho g \tag{1.40}$$

Energy: $$\rho c_p\left[\left.\frac{\partial T}{\partial t}\right|_{\chi}+(v-v_{mesh})\cdot\nabla T\right]=k\,\nabla^2 T \tag{1.41}$$

where k, c_p, and μ are thermal conductivity, specific heat at constant pressure, and dynamic viscosity, p and T are the pressure and temperature, and v and v_{mesh} are the fluid velocity and mesh velocity vectors, respectively, and g is the gravity vector.

1.4.5 Integral Form of Conservation Equations in ALE Framework

In order to obtain the integral form of the conservation laws for mass, momentum, and energy, the rate of change of integrals of scalar and vector functions over a moving control volume is needed. To this end, Reynold's transport theorem (also known as the Leibniz-Reynolds transport theorem) is used to formulate the basic conservation laws of continuum mechanics, particularly fluid dynamics and large-deformation solid mechanics, as follows:

$$\left.\frac{\partial}{\partial t}\right|_{\chi}\int_{\Sigma(t)}\eta(x,t)dV=\int_{\Sigma(t)}\left.\frac{\partial\eta(x,t)}{\partial t}\right|_{x}dV+\int_{\partial\Sigma(t)}\eta(x,t)\,v_{mesh}\cdot n\,dA \tag{1.42}$$

In which η is a scalar function (defined in the spatial domain), $\Sigma(t)$ is an *arbitrary* time-dependent control volume which has a closed boundary of $\partial\Sigma(t)$. The boundary points at time t move with mesh velocity of v_{mesh}, n is the outward unit normal vector to the surface $\partial\Sigma(t)$, dV and dA are volume and surface elements at x. If the scalar $\eta(x,t)$ is replaced by the fluid density ρ, momentum ρv, and specific total energy ρE, one can obtain the integral form of the conservation laws for mass, momentum, and energy in the ALE framework as follows:

Mass:
$$\left.\frac{\partial}{\partial t}\right|_{\chi}\int_{\Sigma(t)}\rho dV+\int_{\partial\Sigma(t)}\rho\;c.n\;dA=0 \tag{1.43}$$

Momentum:
$$\left.\frac{\partial}{\partial t}\right|_{\chi}\int_{\Sigma(t)}\rho v dV+\int_{\partial\Sigma(t)}\rho v\;c.n\;dA=\int_{\Sigma(t)}(\nabla\cdot\sigma+\rho b)dV \tag{1.44}$$

Energy:
$$\left.\frac{\partial}{\partial t}\right|_{\chi}\int_{\Sigma(t)}\rho E dV+\int_{\partial\Sigma(t)}\rho E\;c.n\;dA$$
$$=\int_{\Sigma(t)}(v\cdot\rho b+\nabla\cdot(\sigma\cdot v)dV \tag{1.45}$$

It is noted that if $v_{mesh}=v$ $(c=0)$, the Lagrangian description is obtained. Also, $v_{mesh}=0$ $(c=v)$ corresponds to the Eulerian description.

1.5 Motivation for Dissertation and Research Objectives

Despite the advances in the theoretical and experimental study of meniscus dynamics, there remains a serious lack of computational simulations capable of capturing the

transient evolution of the meniscus shape and directly tracking the sharp liquid-gas interfaces. A literature review reveals that among available computational techniques, the full continuum mechanical solution of liquid flow in a capillary channel has received little attention. The primary objectives of the current study are to develop a robust computational model to investigate the dynamic response of a meniscus during the capillary flow subject to heat transfer and evaporation between vertical parallel plates using as few simplifying assumptions as possible. The existing simplified analyses assume the interface as a surface with fixed and prescribed curvature. However, in realistic applications, the interface forms in the shape of various curves. Instead of specifying the meniscus shape, the goal of this study is, for the first time, to compute them as part of the solution of the problem. Thus, special attention is paid in this work to the use of the arbitrary Lagrangian-Eulerian technique to directly track the formation and evolution of the meniscus shape in both cases of hydrophilic and hydrophobic capillary flows. In the next part of the dissertation, the developed model is devised further to account for the effects of interfacial phase change heat transfer (evaporation) on the meniscus dynamics. Finally, the developed model is employed to conduct parametric studies on the effect of important design and operating variables on flow and thermal fields emerging in evaporating capillary flows.

1.6 Dissertation Outline

The rest of the dissertation is organized as follows. Following the Introduction chapter, Chapter 2 presents the theoretical solution to the dynamic response of a meniscus between vertical parallel plates in the Lucas-Washburn framework. The first part of

Chapter 2 is devoted to the hydrodynamic characteristics of the transient behavior of a meniscus, and the second part addresses a meniscus subject to heat transfer and evaporation. Chapter 2 is concluded by detailed calculation of the recoil pressure exerted on an evaporating meniscus and the determination of steady-state meniscus shape. Chapter 3 describes the computational model developed in this work to simulate the hydrodynamics of non-evaporating capillary penetration or depression of liquid between hydrophilic and hydrophobic vertical parallel plates, including a review of the related literature, the problem statement, details of numerical procedure, validations, and the computational predictions. Chapter 4 explains the extended computational model to investigate the dynamic response of a meniscus subject to heat transfer and evaporation during the capillary flow between vertical parallel plates. The chapter includes a literature survey related to the transient behavior of evaporating meniscus, description of the physical system, computational methodology, validation process, numerical results, and parametric study. Finally, Chapter 5 summarizes the results and findings of the dissertation and presents recommendations for future work with respect to the research gaps.

CHAPTER 2: THEORETICAL MODELING OF MENISCUS DYNAMICS

As described in the previous chapter, if a liquid is brought in contact with conduits formed by solid surfaces, liquid transport occurs under the action of adhesion and cohesion forces. Based on the thermal conditions of the system, the meniscus can be subject to phase change. This chapter presents the derivation and solution of the mathematical equations for the transient behavior of liquid meniscus with and without evaporation in a parallel plate configuration. Also, the calculation of the recoil pressure exerted on an evaporating meniscus and the determination of equilibrium meniscus shape are discussed.

2.1 Theoretical Modeling of Capillary Penetration and Depression

The theoretical model is based on the Lucas-Washburn Equation (LWE) [26,27] and uses the following momentum balance applied to a control volume containing the liquid in the capillary channel:

$$\frac{\partial}{\partial t}\int_V \rho\vec{v}\, dV + \int_A \rho\vec{v}_b\,(\vec{v}_b \cdot \hat{n})dA = \sum \vec{F} \tag{2.1}$$

where the first and second terms on the left-hand side represent the rate of change of momentum of the liquid column and the net momentum crossing the boundaries of the control volume, respectively. The right-hand side represents the sum of the forces acting on the control volume. In the surface integral, $\vec{v}_b$ is the fluid velocity at the boundary of the control volume relative to the boundary. Several assumptions must be made to solve

Eq. (2.1) analytically, including the assumptions of a constant contact angle θ, constant and uniform curvature along the meniscus, and fully developed two-dimensional laminar flow between the parallel channel walls [28,29].

Denoting the average height of the liquid column relative to the free surface in the reservoir at time t by $h(t)$ and noting that momentum only crosses the boundary of the control volume at the column entrance, Eq. (2.1) can be rewritten as:

$$\rho w \frac{d}{dt}\left[(h(t)+h_0)\frac{dh(t)}{dt}\right] - \rho w v_b^2 = 2\sigma cos\theta - \rho g w h(t) - \frac{12\mu}{w}(h(t)+h_0)\frac{dh(t)}{dt} \tag{2.2}$$

where σ is the surface tension at the liquid-air interface, and θ is the contact angle. The terms on the RHS of the above equation represent the effects of surface tension, gravitational, and viscous forces per unit length, respectively. Equation (2.2) is subject to the following initial conditions:

$$h(0) = 0 \tag{2.3}$$

$$\left.\frac{dh}{dt}\right|_{t=0} = 0 \tag{2.4}$$

The equilibrium height of the liquid column, h_e, can be obtained by solving Eq. (2.2) at steady state:

$$h_e = \frac{2\sigma cos\theta}{\rho g w} \tag{2.5}$$

It should be noted that the equilibrium height of Eq. (2.5) is valid only for narrow capillary channels in which the liquid volume in the interface region (above the lowest point of the meniscus) is negligible [30].

Determination of the fluid velocity crossing the control volume boundary at the entrance of the capillary channel, v_b, requires further attention. As noted by Levine et al. [28], there are two possible limiting-case scenarios to consider. In the first scenario, it is supposed that the liquid in the reservoir is stagnant and achieves a fully developed velocity profile immediately *after* entering the capillary channel. Thus, the advective term (the third term) on the LHS of the Eq. (2.2) vanishes and the momentum balance reduces to:

$$\rho w \frac{d}{dt}\left[(h(t)+h_0)\frac{dh(t)}{dt}\right] = 2\sigma cos\theta - \rho g w h(t) - \frac{12\mu}{w}(h(t)+h_0)\frac{dh(t)}{dt} \tag{2.6}$$

The second scenario again assumes that the liquid in the reservoir has zero velocity, but the liquid enters the capillary at time t with an average velocity of $v_b = dh/dt$. In this case, Eq. (2.2) simplifies to:

$$\rho w(h(t)+h_0)\frac{d^2h(t)}{dt^2} = 2\sigma cos\theta - \rho g w h(t) - \frac{12\mu}{w}(h(t)+h_0)\frac{dh(t)}{dt} \tag{2.7}$$

The preceding treatments of the inertial terms lead to two analytical solutions that are identical except for the inertial terms. Both expressions have been used by previous investigators [29,31]. In this work, theoretical solutions referred to as *"Analytical 1"* and *"Analytical 2"* correspond to Eqs. (2.6) and (2.7), respectively. The above discussion about the specification of the fluid velocity at the entrance of the capillary channel is independent of the velocity direction and applies to both capillary penetration and depression cases. In other words, regardless of the velocity direction in the capillary channel, Eq. (2.6) is based on the assumption that the fluid at the channel entrance is at the reservoir velocity ($v_b = 0$), whereas Eq. (2.7) assumes that the fluid at the entrance

has the same velocity as the liquid in the channel ($v_b = dh/dt$). It is noted that because these scenarios represent limiting cases, the actual momentum entering the capillary channel is expected to lie in between these two bounds.

2.2 Theoretical Modeling of the Transient Response of the Evaporating Meniscus

The following mathematical model describes the fluid mechanics, heat transfer, and interfacial phenomena associated with the spontaneous flow of a superheated liquid between parallel plates that is subjected to saturated vapor above the meniscus. Applying a force balance to a control volume containing the liquid in the capillary channel and assuming fully developed laminar flow induced by the interplay of gravity, friction, and the surface tension forces yields the classical LWE [28]. The LWE does not account for the complex flow field at the entrance region of the capillary channel and in the vicinity of the moving meniscus. As discussed in the body of the paper, for a meniscus subject to phase change (evaporation/condensation), the LWE has been extended to account for the recoil force that arises due to the interfacial momentum jump [32]. Considering the submerged height (h_0) of the capillary channel below the free surface of the liquid in the reservoir, the equation of motion for a meniscus subject to evaporation/condensation between the parallel plates can be written as follows:

$$\underbrace{\rho w \frac{d}{dt}\left[(h(t)+h_0)\left(\frac{dh(t)}{dt}+\frac{j}{\rho_l}\right)\right]}_{inertia} = \underbrace{2\sigma cos\theta}_{surface\ tension} - \underbrace{\rho g w h(t)}_{gravity} - \underbrace{\frac{12\mu}{w}\left[(h(t)+h_0)\left(\frac{dh(t)}{dt}+\frac{j}{\rho_l}\right)\right]}_{viscous\ drag} - \underbrace{w\frac{j^2}{\rho_v}}_{vapor\ recoil} \tag{2.8}$$

where $h(t)$ denotes the average height of the liquid column relative to the free surface in the reservoir at time t. σ, θ, and j are the surface tension at the liquid-vapor interface, contact angle, and interfacial mass flux due to phase change, respectively. The following initial conditions are applied:

$$h(t=0)=0 \tag{2.9}$$

and

$$\left.\frac{dh}{dt}\right|_{t=0}=0 \tag{2.10}$$

The terms on the RHS of Eq. (2.8) represent the effects of surface tension, gravitational, viscous, and momentum jump forces per unit depth of the channel, respectively. It is noted that for the non-evaporating case, the interfacial mass flow rate is zero. However, when the phase change occurs (evaporation: $j>0$ and condensation: $j<0$), the momentum jump term emerges that exerts a downward force on the meniscus. The typical approach for the determination of the mass transfer rate at the liquid-vapor interface is the use of kinetic theory that relates the interfacial mass flux j to the interface temperature T_i [33]:

$$j = \frac{\alpha \rho_v h_{lv}}{T_v^{1.5}} \left(\frac{M_w}{2\pi R_u} \right)^{0.5} (T_{int} - T_v) \tag{2.11}$$

In the preceding equation, α is the accommodation coefficient ($0 < \alpha \leq 1$), M_w is the molecular mass, and R_u is the universal gas constant. There are several major simplifying assumptions and rather arbitrarily chosen variables in Eq. (2.11) that limit the accuracy of the model predictions. Some of the simplifying assumptions are:

- The coupling between the liquid and vapor phases during evaporation is neglected [34].
- It is challenging to determine the accurate value for the empirical parameter of mass accommodation coefficient.
- The temperature jump across the meniscus, $T_i - T_v$ in Eq. (2.11), is assumed to be equal to the temperature difference between the superheated liquid and saturated vapor. As such, application of kinetic theory neglects the thermal diffusion adjacent to the meniscus inside the liquid.
- Transient thermal effects cannot be captured by Eq. (2.11) since it provides a constant evaporation rate.

It should be noted that several researchers have employed the kinetic theory of gasses to simulate the evaporation and/or condensation processes across the meniscus [35,36]. The results of models based on kinetic theory are strongly dependent on the choice of the evaporation and condensation coefficients.

Figure 2.1 shows the sensitivity of the analytical solution with respect to the superheat, ΔT for two wall spacings of w = 0.5 mm and w = 0.7 mm. The results highlight the dependence of the water column on the superheat degree.

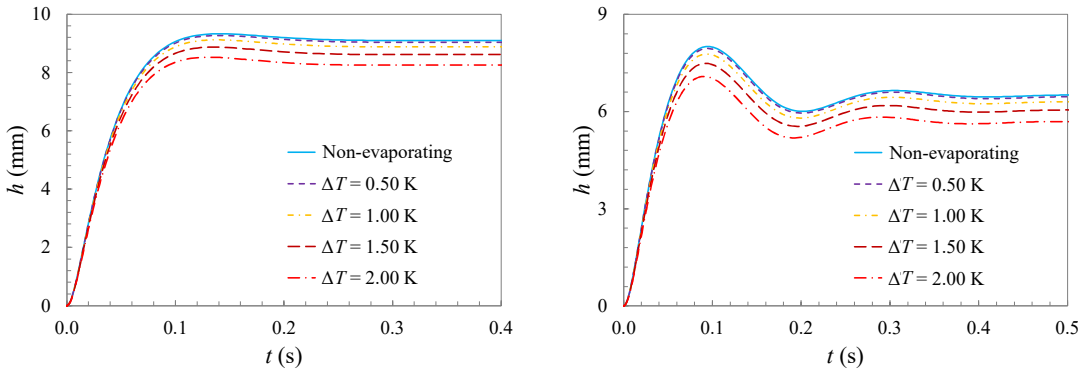

(a) (b)

Fig. 2.1 Theoretically predicted water column height between parallel copper plates and various values for ΔT (a) w = 0.5 mm and (b) w = 0.7 mm.

2.3 Theoretical Determination of the Vapor Recoil Pressure

To account for phase change at the liquid-vapor interface, several coupled mechanisms should be considered. Generally, a moving liquid particle with a low velocity at the meniscus undergoes high acceleration upon evaporation due to the significant density change. The accelerating evaporated mass exerts a pressure on the meniscus in the opposite direction that is known as vapor recoil in the literature [33]. In other words, vapor recoil emerges due to the velocity jump at the liquid-vapor interface. The interfacial mass flux due to evaporation can be expressed as:

$$j = \rho_l(\mathbf{V}_l - \mathbf{V}_i)\cdot\mathbf{n} = \rho_v(\mathbf{V}_v - \mathbf{V}_i)\cdot\mathbf{n} \tag{2.12}$$

where j is the interfacial mass flux, $\mathbf{n}$ is the outward normal unit vector, and $\mathbf{V}_l$, $\mathbf{V}_v$, and $\mathbf{V}_i$ refer to liquid velocity, vapor velocity, and interface velocity, respectively. The recoil pressure applied on the liquid-vapor interface is then given by:

$$p_{recoil} = -\frac{\rho_l - \rho_v}{\rho_l \rho_v} j^2 \tag{2.13}$$

And due to the large discrepancy between the densities of liquid and vapor ($\rho_l \gg \rho_v$) the recoil pressure can be reduced to:

$$p_{recoil} = -\frac{j^2}{\rho_v} \tag{2.14}$$

2.4 Theoretical Modeling of the Meniscus Shape at Steady-State

The performance of capillary-assisted passively pumped thermal management devices is strongly dependent on the shape of the curved liquid-vapor meniscus. The static steady-state meniscus shape between either hydrophilic or hydrophobic parallel plates can be obtained from the following equation below:

$$\rho g h(x) = \frac{\gamma_{lv} \frac{d^2 h(x)}{dx^2}}{\left(1 + \left(\frac{dh(x)}{dx}\right)^2\right)^{1.5}} = -\gamma_{lv} \mathrm{K} \tag{2.15}$$

in which x is the coordinate component measured along the capillary channel width that varies from zero at the left wall to w at the right wall, and K is the local mean curvature of the meniscus. The above ordinary differential equation can be considered as a boundary value problem with the following boundary conditions:

$$\left.\frac{dh}{dx}\right|_{x=0} = -tan\theta_1 \tag{2.16}$$

and

$$\left.\frac{dh}{dx}\right|_{x=w} = tan\theta_2 \tag{2.17}$$

It is noted that for walls with similar surface properties, the contact angle θ_1 at the left wall is the same as the contact angle θ_2 at the right wall. Obviously, for dissimilar

plates, the contact angles θ_1 and θ_2 are different, and consequently, meniscus evolves to have a shape which is asymmetric about the midpoint.

Eq. (2.15), along with boundary conditions (2.16) and (2.17), was solved in MATLAB to determine meniscus shape between parallel plates at the steady state.

CHAPTER 3: COMPUTATIONAL SIMULATION OF SPONTANEOUS LIQUID PENETRATION AND DEPRESSION BETWEEN VERTICAL PARALLEL PLATES

In the following chapter, a computational fluid dynamics model using dynamic mesh is developed to simulate the capillary penetration or depression of liquid between hydrophilic and hydrophobic vertical parallel plates.

3.1 Background

Capillary driven flows appear in a wide range of natural and engineering systems, including but not limited to water transport in plants, drainage of continuously produced tear fluid from the eye, liquid flow in heat pipes, liquid transport in the micro-gravity environment of satellites and space vehicles, oil recovery, and ink-jet printing [5]. Capillary action is the spontaneous movement of liquid within the voids or conduits formed by solid surfaces due to the interaction of adhesion, cohesion, and surface tension forces. The adhesion between the liquid and the solid walls of the capillary channel along with the surface tension force induced by the cohesion between the liquid molecules at the liquid-gas interface, creates the driving force for penetration of the liquid column inside the capillary channel. This force is countered by viscous forces as the liquid flows through the capillary channel and can be either countered or augmented by gravity forces acting on the liquid. The surface tension force, acting along the meniscus surface, induces a pressure jump across the liquid-vapor interface that can be determined using the Young-Laplace equation [37].

The earliest investigations of the transient rise of liquids in a vertical capillary channel were performed by Lucas [38] and Washburn [27]. In their analyses, a theoretical expression known as the Lucas-Washburn equation (LWE) was developed by balancing surface tension, viscous and gravity forces acting on the fluid control volume. Fisher and Lark [39] validated the LWE for small glass capillary channels using water and cyclohexane. The LWE, often considered as the classical model for describing the capillary phenomena, does not include the inertial effects in the momentum balance. As such, it fails to predict the early stages of liquid penetration when the gravitational and viscous forces are relatively small and inertial effects are the primary factor that balances the capillary force. In an effort to improve the LWE, Rideal [31] and Bosanquet [40] included the effects of inertia on the liquid rise in capillary channels and thereby eliminated the non-physical initial velocity observed in the early theoretical models. As the height of the liquid column increases, the gravity and viscous forces play a more important role and the effect of inertia weakens [41]. The capillary flow can be affected by the geometry of the capillary channel, the physical properties of the liquid, the solid surface type, and the influence of the liquid flow in a reservoir that might exist near the entrance of the capillary channel. Levine et al. [28] noted that the assumption of fully-developed Poiseuille flow in the fluid is not strictly valid and, hence, the classic LWE is not valid at the two ends of the fluid column, namely near the entry region and near the advancing meniscus. They accounted for the pressure field in the reservoir near the entry region of a circular capillary channel and developed one of the most comprehensive analytical models available in the literature.

Non-circular capillary channel geometries such as triangular and rectangular channels and parallel plates are also of importance [42,43]. For instance, rectangular channels with a high surface-to-volume ratio have been extensively used in microfluidic systems due to the potential for high rates of heat and mass transfer between the fluid and solid walls [44]. Several analyses similar to those associated with the LWE have been performed for non-circular capillary channels and parallel plates of finite length [45–51]. A unified formulation for the capillary flow in rectangular and circular capillary channels was derived by Xiao et al. [52]. They considered the influences of the entrance pressure difference, and the dynamic contact angle between the moving liquid front and the solid wall as a function of time. Bullard and Garboczi [30] implemented free energy minimization principles to obtain the equilibrium height and the meniscus shape for the capillary rise between vertical parallel plates.

Although considerable research has been devoted to understanding the penetration of a liquid into a capillary channel, the majority of past works have focused on the development of analytical models that employ major simplifying assumptions. Detailed CFD modeling can account for several important features that are often ignored in analytical models, such as the developing flow in the entrance region of the capillary channel, the slip flow condition at the advancing meniscus, and the inertial forces acting on the fluid in the reservoir. Among available CFD techniques, the volume of fluid (VOF) methodology has been one of the most popular [15]. In this method, the liquid-gas interface is confined to cells that have a liquid volume fraction between 0 and 1 and is reconstructed using various techniques including the donor-acceptor method [15] or piecewise linear interpolation method [53], among others. The main drawbacks of the

VOF techniques are that the exact interface location is uncertain because of the discrete volume fraction information, and the flow variables and fluxes at the interface are averaged over the computational cell. Gaulke and Dreyer [54] numerically simulated the capillary liquid rising between parallel perforated plates under microgravity conditions using the commercial CFD package Flow3D. They employed the VOF model and validated their predictions experimentally. An accuracy within the range of 10-15% was reported. A series of static and dynamic contact angle numerical simulations of the capillary rise between parallel plates was carried out by Schonfeld et al. [55] employing the commercial flow solver CFX4 and the VOF technique. In order to achieve mesh independent numerical results, they proposed a macroscopic slip range in the vicinity of the contact line along with an appropriate body force. Saha and Mitra [56] also used the VOF approach to study dynamic contact angle models for the capillary flow in a microchannel with integrated pillars. In a companion study, they employed the VOF method to investigate the capillary flow in a patterned microchannel with alternating layers of hydrophilic and hydrophobic walls [57]. More recently, Grunding et al. [58,59] conducted a computational analysis of a liquid rising between parallel plates using various numerical approaches including VOF and arbitrary Lagrangian-Eulerian (ALE) method. Following the assumption of the classic analytical model, they assumed that the meniscus was a circular arc and remained unchanged during the penetration of liquid into the capillary channel. In the ALE method, the computational grid is neither fixed in space nor follows the motion of the material elements. Instead, the mesh moves in an arbitrarily described manner to accommodate the motion or deformation of a boundary [60,61]. The effect of the mesh motion is

accounted for by modifications to the material derivative in the Navier-Stokes equations [62]. In this technique, frequent remeshing is required to avoid large mesh distortions and to maintain the mesh quality.

The review of the literature reveals that, despite the extensive volume of research conducted on capillary flow, there remains a lack of CFD modeling that can predict the transient evolution of the meniscus shape and directly track the sharp liquid-gas interface. Interestingly, among various computational methods, the full continuum mechanical solution to the penetration of a liquid in a capillary channel has received little attention. Therefore, the main objective of this study is to develop a CFD model capable of accurately simulating meniscus formation dynamics and capillary flow behavior of a liquid column between two vertical parallel plates. Unlike previous CFD studies, the meniscus profile will not be prescribed but allowed to dynamically evolve based on the interaction among the surface tension, adhesion, gravity and viscous forces. The two-dimensional transient conservation equations for mass and momentum will be solved with the ALE method in a finite volume formulation using the commercial CFD package ANSYS Fluent. The capillary pressure differential resulting from the curvature of the meniscus is applied as a boundary condition to the interface using user-defined functions (UDFs). A dynamic mesh method will be implemented to directly track the interface with no need to employ implicit interface tracking schemes. The developed sharp interface tracking method allows for more accurate prediction of meniscus and capillary channel height dynamics compared to previous VOF models. It is noted that complex physical phenomena related to the dynamic contact angle and

triple point hysteresis affect the dynamics of capillary flow, however, incorporation of these effects is out of the scope of the present study.

3.2 Problem Description

The capillary flow of water between vertical parallel plates is considered using the computational domain shown in Fig. 3.1. The physical domain consists of two main parts, namely the capillary channel and the reservoir. The capillary channel is formed by partially submerging two vertical parallel plates with a wall spacing of w into the large liquid reservoir. The reservoir has a width of 11 mm on each side of the capillary and is 10 mm (22 mm) tall for the hydrophilic silver (hydrophobic Teflon) plates. The initial height of the liquid in the reservoir is 2 mm less than the reservoir height for both silver and Teflon plates. The space above the liquid surface in the reservoir is filled with air. The contact angle θ between the liquid and the solid walls, measured relative to the vertical plane, is constant at 63° and 110° for silver (Ag) and Teflon (PTFE) walls, respectively [63,64]. The submerged section of the plates is 3 mm and 15 mm deep into the water for the silver and Teflon, respectively. The plates are 1 mm thick, and their spacing will be varied from 0.5 mm to 3 mm.

The initial height of the liquid between the vertical plates is assumed to be equal to the height of the water in the reservoir. The upward penetration (or downward depression) of water into (or out of) the capillary channel begins by changing the contact angle θ between the liquid and the walls from 90° at $t = 0$ to 63° (or 110°). As the liquid in the capillary channel rises (falls) the liquid in the reservoir recedes (advances). The time-varying interface location between the air and water in the reservoir is captured using a

VOF technique. It is noted that the changes of the liquid height in the reservoir are relatively small due to the significantly greater free surface area in the reservoir compared to that in the capillary channel. Both air and water were assumed to be incompressible and Newtonian fluids with constant properties shown in Table 3.1. A gravitational acceleration of 9.81 m/s^2 is applied in the negative y-direction.

Table 3.1 Physical properties of water and air.

Fluid	Water	Air
Density, ρ (kg/m^3)	998.2	1.225
Dynamic viscosity, μ (kg/m·s)	1.003×10^{-3}	1.7894×10^{-5}
Surface tension, σ (N/m)	0.0728	–

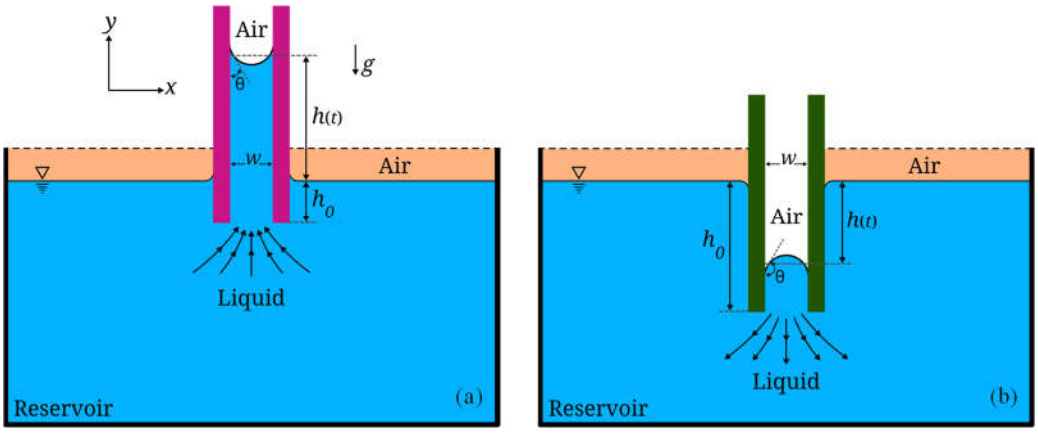

Fig. 3.1 Liquid in a vertical capillary channel with (a) penetration due to hydrophilic walls, and (b) depression due to hydrophobic walls.

3.3 Computational Model

Transient conservation equations for the mass and momentum for two-dimensional laminar flow with constant properties are:

$$\nabla \cdot \boldsymbol{V} = 0 \tag{3.1}$$

$$\rho\left[\left.\frac{\partial \boldsymbol{V}}{\partial t}\right|_{ref} + ((\boldsymbol{V} - \boldsymbol{V}_{mesh}) \cdot \nabla)\boldsymbol{V}\right] = -\nabla p + \mu \nabla^2 \boldsymbol{V} + \rho \boldsymbol{g} \tag{3.2}$$

where t, ρ, μ, $\boldsymbol{V}$, $\boldsymbol{V}_{mesh}$, p, and $\boldsymbol{g}$ are time, density, dynamic viscosity, velocity vector, mesh velocity vector, pressure, gravitaty vector, respectively. It should be noted that the first term in the left-hand side of the momentum equation represents the time derivate in the referential domain (i.e., the coordinate system following the moving mesh). The VOF approach was employed to capture the liquid-air interface in the reservoir. The evolution of the liquid volume fraction in the reservoir is described by:

$$\frac{\partial \alpha_l}{\partial t} + \boldsymbol{V} \cdot \nabla \alpha_l = 0 \tag{3.3}$$

where α_l is the liquid volume fraction. The air volume fraction is $\alpha_g = 1 - \alpha_l$.

No-slip conditions were applied at the walls, except at the moving contact line between the meniscus and the walls where the no-slip boundary condition is not valid due to the singularity in the viscous stress [65,66]. In the current study, after the enforcement of the contact angle the grid nodes on the contact line are moved with the same velocity as their immediate grid node neighbors to preserve the contact angle. Pressure boundary conditions were prescribed above the meniscus and at the top boundary of the reservoir.

An ALE scheme [60–62] with a dynamic mesh was employed in the fluid within the capillary channel to directly track the meniscus without using implicit interface tracking schemes. This technique is useful in the simulation of fluid flow problems with moving boundaries. The effect of the mesh motion in the governing equations (3.1) to (3.3) is

accounted for by calculating the advective terms at the surfaces of the control volumes using the velocity difference between the flow and the control surface.

The preceding equations and the related boundary conditions were solved using a finite volume scheme implemented in the commercial CFD package ANSYS Fluent. The SIMPLE algorithm [67] was used for the velocity-pressure coupling. The pressure, velocity, and volume fraction at the cell interfaces were interpolated using the PRESTO!, QUICK, and piecewise-linear interpolation schemes, respectively [53,67]. At each time step, the local capillary pressure difference across the meniscus, Δp, resulting from the local curvature of the water-air interface, K, was determined using Laplace's equation, $\Delta p = \sigma K$, where σ is the surface tension [68]. The pressure profile was then applied to the interfacial faces in the capillary channel and the governing equations were solved. The calculated velocities at the interfacial cells in the y-direction were used to update the position of the meniscus nodes. A new pressure profile was determined based on the updated meniscus shape and was applied as the boundary condition at the meniscus in the new time step.

Due to the large density and viscosity differences between the air and water, the air flow was neglected. Under-relaxation factors were adjusted when needed to enhance the convergence. The solution in each time step was considered to be converged when the scaled residuals for all the equations decreased to less than 10^{-4}. Due to the transient nature of the problem and the dependence of the mesh motion on the flow field, the *implicit update* feature of the dynamic mesh method in Fluent was enabled to update the mesh multiple times during a time step. This practice improved the stability and

convergence by enforcing a stronger coupling between the mesh motion and the evolving flow field in the liquid.

3.3.1 Calculation of the Meniscus Curvature

As noted previously, the water-air interface is assumed to be initially flat. At the initial time step, the first and last control surfaces on the meniscus (adjacent to the walls) are inclined at an angle equal to the contact angle between the liquid and the solid walls. The contact angle remains unchanged throughout the simulation. The initial local curvature imposed by the contact angle creates a pressure difference across the interface at the control surfaces adjacent to the wall. This pressure difference induces liquid motion near the walls. The liquid motion, initiated at the corners of the meniscus, propagates towards the middle interfacial control volumes due to the surface tension and diffusion effects. At each time step, the capillary pressure difference across each interfacial control surface is determined based on the local curvature of the liquid-gas interface through use of the Laplace equation. Figure 3.2 shows the curve fitting method employed to determine of the local meniscus curvature. To determine the curvature at each control surface, a third-degree polynomial curve fitting was applied using the coordinates of the endpoints of the control surface and the endpoints of the two neighboring surfaces. For example, the curvature at the control surface connecting nodes 3 and 4 in Fig. 3.2 was determined by using a cubic polynomial passing through nodes 2 to 5 (the dash-dot green curve). Using the equation of the curve, $y = f(x)$, the curvature at the midpoint of the control surface was approximated from $K = f''(x)/[1 + f'(x)^2]^{3/2}$, where x is the x-coordinate of the midpoint of the control

surface. The green square symbol between the nodes 3 and 4 in Fig. 3.2 shows where the curvature associated with the control surface 3-4 was calculated.

The preceding procedure was applied to all the control surfaces on the meniscus except the two control surfaces adjacent to the walls. For these corner control surfaces, a quadratic polynomial curve fitting was employed (the red dashed curve in Fig. 3.2). The quadratic curve fitting for the left-corner control surface used the coordinates of nodes 1 and 3 and the contact angle at the wall (see Fig. 3.2). The slope at the wall was used instead of the coordinates of node 2 to preserve the exact contact angle between the liquid and the wall. After the curve fitting, the curvature at the midpoint of the control surface 1-2 was approximated by using the coordinates shown by the red triangle between nodes 1 and 2, where x is the average x-coordinate of nodes 1 and 2, and y is the value of the quadratic function at x. Determination of the pressure profile at the meniscus and the associated mesh motion were implemented by using user-defined functions (UDFs) developed in C++ and hooked to ANSYS Fluent version 19.1. The non-uniform pressure profile along the meniscus obtained using the above procedure changed at each time step.

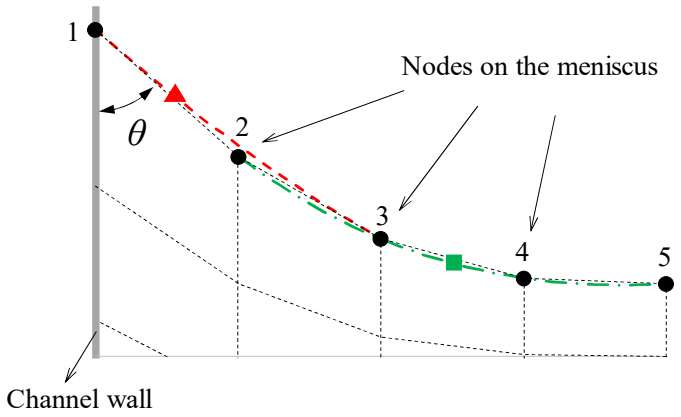

Fig. 3.2 Calculation of the local curvature of the meniscus. The red dashed curve is the quadratic polynomial used to obtain the curvature of the corner control surface (connecting nodes 1 and 2), and the green dash-dot curve is the cubic polynomial used to calculate the curvature at a representative middle control surface (connecting nodes 3 and 4). The triangular and square symbols show the point where the curvature is calculated.

3.4 Results and Discussion

This section is organized as follows. First, the independence of the results from the grid and time step size were verified. Next, the model was validated by comparing the predicted equilibrium capillary height and equilibrium meniscus shape to those predicted using existing theoretical models. The dynamics of the meniscus formation are presented next, followed by a description of the flow field at the advancing meniscus and in the vicinity of the channel entrance. Finally, the validated model is employed to study the effect of the wall spacing on the transient capillary flow in both hydrophilic and hydrophobic channels.

3.4.1 Grid and Time Step Size Independence

The grid was split into several blocks in order to achieve better control over the mesh in critical portions of the domain, especially in the capillary channel and in the reservoir in the vicinity of the capillary channel inflow region. The independence of the computational results from the grid and time step size was verified by systematically varying the mesh resolution and the time step size. Figure 3.3 depicts the height of the water column vs. time for the case of w = 0.7 mm and θ = 63° with five different grid densities in the capillary channel corresponding to N = 20 to 60 cells along the channel width. For each grid, the cell height in the *y*-direction was also changed to maintain a cell aspect ratio of about one. Here, the water column height is defined as the distance between the average y-location of the meniscus and the y-location of the liquid in the reservoir, as shown in Fig. 3.1. It can be seen in this figure that increasing the number of cells across the channel beyond 50 did not have a noticeable effect on the results. Additional discussion of the details of the transient response is presented in Sec. 3.4.4. It is noted that a similar study was carried out for the wall spacing of w = 2 mm and it was found that a grid containing 140 cells in the *x*-direction provided grid independent results.

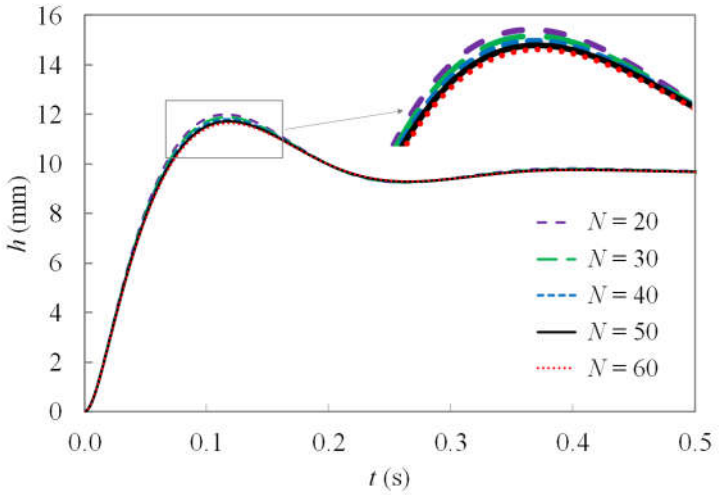

Fig. 3.3 Grid independence study for the rise of the liquid column vs. time for wall spacing of $\boldsymbol{w}$ = 0.7 mm, $\boldsymbol{\theta}$ = 63° and $\boldsymbol{\Delta t}$ = 10^{-5} s.

Figure. 3.4 shows the influence of the time step size, from 5×10^{-6} s to 2×10^{-5} s, on the predicted water column height for w = 0.7 mm and θ = 63°. As evident, decreasing the time step size to less than 10^{-5} s did not improve the accuracy of the results noticeably. Considering the results shown in Figs. 3.3 and 3.4, a computational grid consisting of 50 cells along the capillary channel width (~33,800 total cells) and a time step size of 10^{-5} s were used for the predictions of this study.

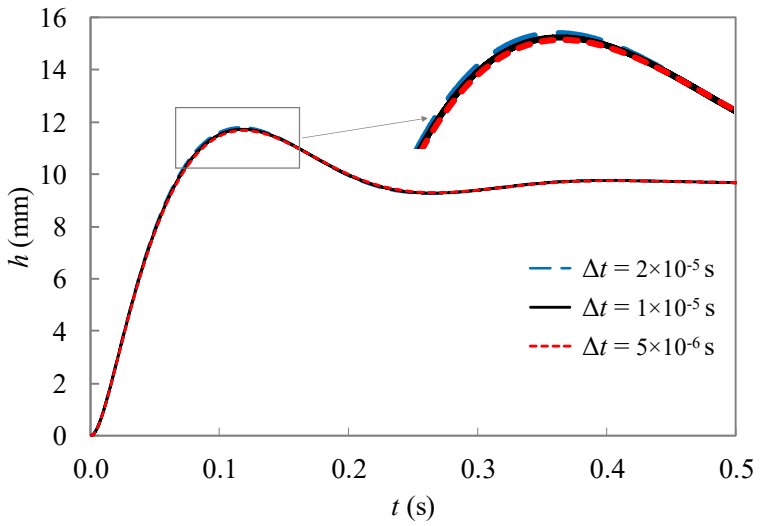

Fig. 3.4 Time step independence study for the rise of the liquid column vs. time for wall spacing of w = 0.7 mm, θ = 63° and N = 50.

3.4.2 Model Validation by Comparison to Theoretical Predictions

In the absence of experimental work on capillary flow between infinitely long parallel plates, the model was further validated by comparing the predicted equilibrium liquid height and meniscus shape to those obtained from available analytical models.

3.4.2.1 Equilibrium Capillary Liquid Height

The equilibrium capillary liquid height can be obtained by applying a balance between the surface tension and gravitational forces, resulting in $h_e = 2\sigma cos\theta/(\rho g w)$. The computationally determined equilibrium capillary heights for hydrophilic and hydrophobic parallel plates were compared with the analytically predicted values. For each case, two wall spacing values of 0.5 mm and 0.7 mm were examined. Silver and Teflon were considered to represent hydrophilic and hydrophobic walls with contact

angles of $\theta = 63°$ and $\theta = 110°$, respectively. The comparison results are shown in Table 3.2. As indicated in the table, the equilibrium heights predicted by the CFD model are in good agreement with the theoretical values, with differences less than 0.5%.

Table 3.2 Comparison of the computationally determined equilibrium heights with the theoretical equilibrium heights for hydrophilic (Ag) and hydrophobic (PTFE) walls with spacings of $w = 0.5$ mm and $w = 0.7$ mm.

	h_e (mm)			
	$w = 0.5$ mm		$w = 0.7$ mm	
	Ag	PTFE	Ag	PTFE
Analytical	13.501	-10.171	9.643	-7.265
CFD	13.562	-10.214	9.683	-7.284
Deviation (%)	0.45	0.42	0.41	0.26

3.4.2.2 Equilibrium Meniscus Shape

The accuracy of the present computational model in terms of the predicted steady-state meniscus shape was verified by comparing the shapes to those of the theoretical model presented by Bullard and Garboczi [30]. The model developed in [30] was programmed by the authors and used to simulate silver and Teflon capillary channels with a wall spacing of 0.7 mm. Figure 3.5 shows the comparison results. Note that the origin of the coordinate system in Fig. 3.5 is set at the left contact line. As evident, the CFD predictions are in excellent agreement with those of the theoretical model,

demonstrating the ability of the computational model to accurately predict the meniscus shape for either hydrophilic or hydrophobic capillary walls.

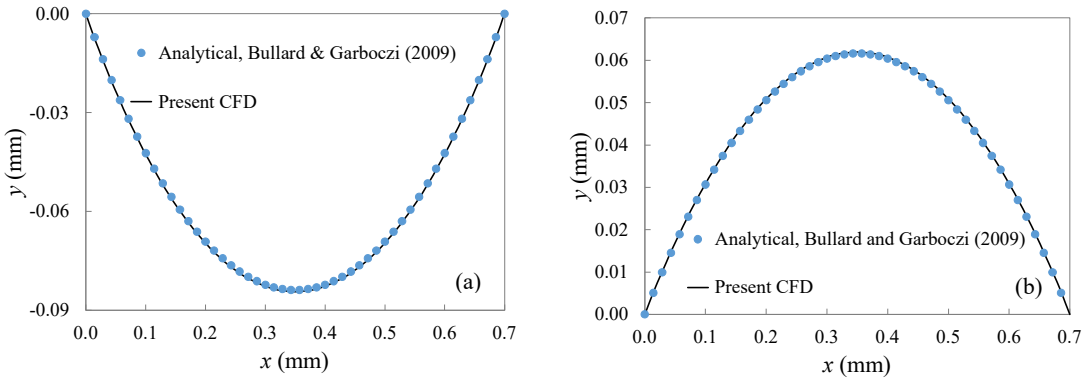

Fig. 3.5 Comparison of the predicted steady-state meniscus shape with those determined from the analytical model of [30] for water confined between parallel (a) silver and (b) Teflon plates with $\boldsymbol{w}$ = 0.7 mm.

3.4.3 Dynamics of the Meniscus Formation

Figure 3.6 shows the evolution of the meniscus shape (between parallel hydrophilic silver plates with a spacing of w = 0.7 mm. As evident in Fig. 3.6a, the initially flat interface evolves to a developed state in a relatively short time compared to the equilibrium time. The time required for the parabolic shape of the meniscus to form is about 0.5×10^{-3} s, whereas the equilibrium time of the capillary rise is about 0.5 s. For $t \gtrsim 5 \times 10^{-3}$ s, the meniscus shape continues to change slightly until it reaches a steady-state shape at equilibrium. It is noted that the initially flat interface is not physically viable, however, since the interface evolves to a parabolic shape within about 0.1% of the equilibrium time, the influence of the initial interface shape on the overall dynamic response is negligible. The meniscus pressure distribution across the capillary

channel is shown in Fig. 3.6b at the times corresponding to the meniscus profiles shown in Fig. 3.6a. As evident, the pressure profile varies significantly during the initial formation phase of the meniscus ($t \lesssim 5 \times 10^{-3}$ s) and reaches an almost uniform distribution for $t \gtrsim 5 \times 10^{-3}$ s.

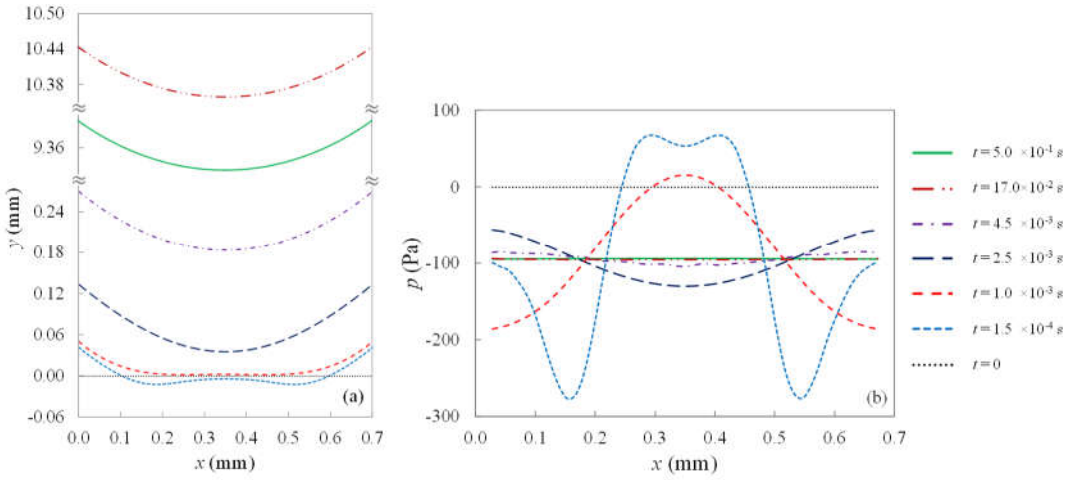

Fig. 3.6 (a) Evolution of meniscus profile between parallel silver plates with a wall spacing of $\boldsymbol{w}$ = 0.7 mm, and (b) meniscus pressure distribution across the capillary channel at different times.

Figure 3.7 shows the equilibrium meniscus shape and the computational mesh near the interface for the hydrophilic silver and hydrophobic Teflon walls. As evident, the mesh remains approximately uniform throughout the simulation, which improves convergence and minimizes numerical errors.

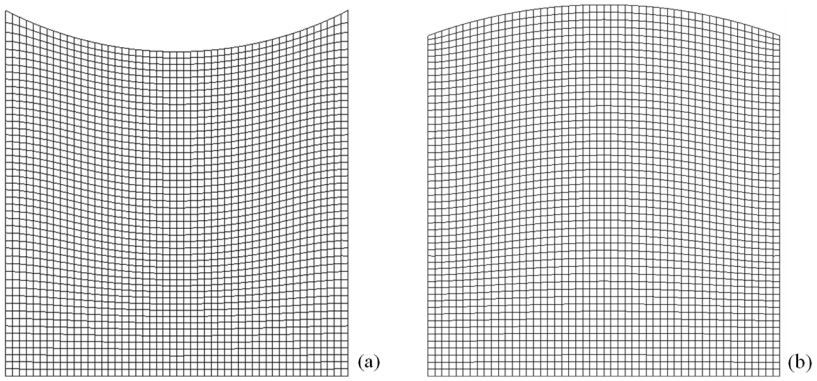

Fig. 3.7 Snapshot of the mesh at the steady state ($t \approx 0.5$ s) for (a) silver and (b) Teflon plates with $w = 0.7$ mm.

3.4.4 Flow Field at the Advancing Meniscus and Within the Entry Region

Figure 3.8 shows the velocity field for hydrophilic silver plates with a spacing of $w = 0.7$ mm at $t = 0.07$ s (equilibrium time ≈ 0.5 s). The results, which are drawn to scale, demonstrate three important features predicted by the present computational model that cannot be accurately captured in theoretical models, namely the slip condition at the contact line of the advancing meniscus and the walls, the developing flow in the entrance region of the channel, and the inertial effects within the reservoir. As evident in Fig. 3.8a, the velocity distribution within the entrance region of the channel is far from fully developed with growing boundary layer thicknesses along the walls and an increasing centerline velocity. The hydrodynamic entrance length is roughly equal to the capillary channel width. Also evident in Fig. 3.8a is the influence of the capillary flow on the velocity distribution in the reservoir. As evident in Fig. 3.8b, the velocity vectors near the advancing meniscus are nearly uniform along the meniscus. Far from the meniscus, however, the velocity vectors exhibit nearly fully developed parabolic behavior with the maximum velocity at the center of the capillary channel.

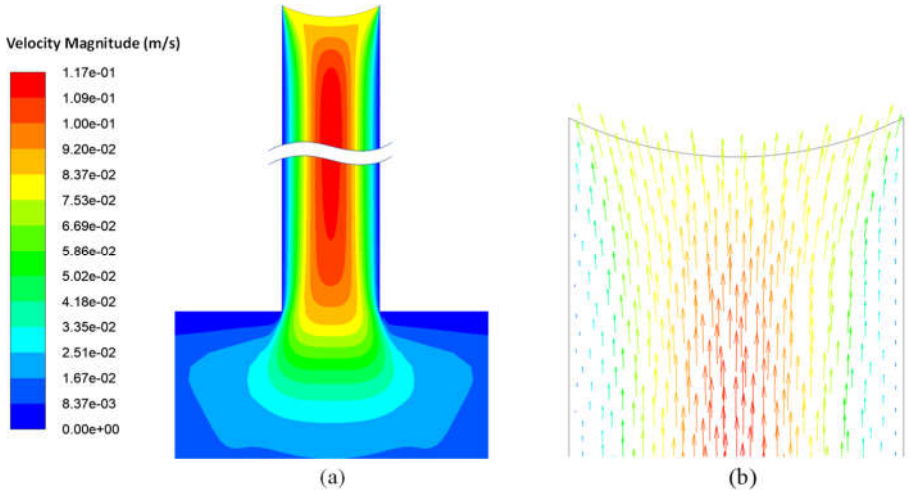

Fig. 3.8 (a) Velocity contours in the entry region and near the advancing meniscus, and (b) velocity vectors adjacent to the advancing meniscus, for silver plates with $w = 0.7$ mm at $t \approx 0.07$ s.

3.4.5 Parametric Study on the Effect of Wall Spacing

In this section, the transient capillary penetration responses for various wall spacings, obtained from the computational model, are compared with the responses predicted by theoretical modeling. The theoretical models were described in the Section 2.1 and are based on the LWE for which a momentum balance is applied to a control volume containing the entire liquid column inside the capillary channel. In the momentum balance, the surface forces (adhesion-cohesion and frictional forces) and the body force (weight of the liquid) are balanced by the time rate of change in momentum of the liquid column and the rate of momentum crossing the control volume at the entrance of the channel. As noted by Levine et al. [28], there are two possible approaches to quantify the rate of momentum flowing into or out of the capillary channel. In the first approximation, it is assumed that the liquid in the reservoir is stagnant but achieves a

fully developed velocity profile immediately *after* entering the capillary channel. In the second approximation it is assumed that the liquid in the reservoir again has zero velocity, except the liquid element which crosses the inlet boundary of the capillary channel is at a velocity equal to the rising velocity of the liquid column (dh/dt). Regardless of whether the velocity at the capillary channel inlet is zero (first approximation) or equal to liquid column velocity (second approximation) the resulting momentum balance equations are identical, except for the advective terms. Of course, these equations do not account for the details of the flow field in the reservoir and additional assumptions are made including an assumed constant and uniformly-distributed pressure distribution along the meniscus, fully-developed flow throughout the capillary channel, and no-slip conditions at the wall including at the advancing meniscus. The two forms of momentum balance were described in detail in the Section 2.1.

Figure 3.9 shows the capillary penetration versus time for hydrophilic silver channel walls and wall spacings from w = 0.5 mm to 3 mm. Alternatively, Fig. 3.10 shows the capillary depression for hydrophobic Teflon walls for w = 0.5 mm to 3 mm. From these figures it is evident that, as the wall spacing is increased, the liquid column exhibits an increasingly oscillatory behavior that eventually stabilizes at an equilibrium height. The oscillations are mainly driven by the interplay between the inertial and gravitational effects, both of which are volumetric phenomena [69–71]. Viscous forces serve to dampen the response and are proportional to the contact area between the liquid and solid walls. Increasing the wall spacing increases the volume-to-surface ratio that, in turn, leads to a slower decay of the oscillatory response. This phenomenon explains the

presence of the so called "critical capillary radius" [29,72] below which no oscillations occur.

As evident in Figs. 3.9 and 3.10, the damping effect of the viscous forces is severely underpredicted by the theoretical models at the large wall spacings. As w increases, the height-to-width ratio of the liquid column decreases, and a larger fraction of the column will reside within the entrance region. Therefore, the theoretical models, which neglect the relatively large viscous forces associated with the entrance region will, increasingly underestimate the actual viscous forces as the wall spacing increases. Hence, the results shown in Figs. 3.9 and 3.10 highlight an important advantage of the present computational model, specifically, the accurate prediction of the dynamic nature of the capillary rise and depression at larger wall spacings.

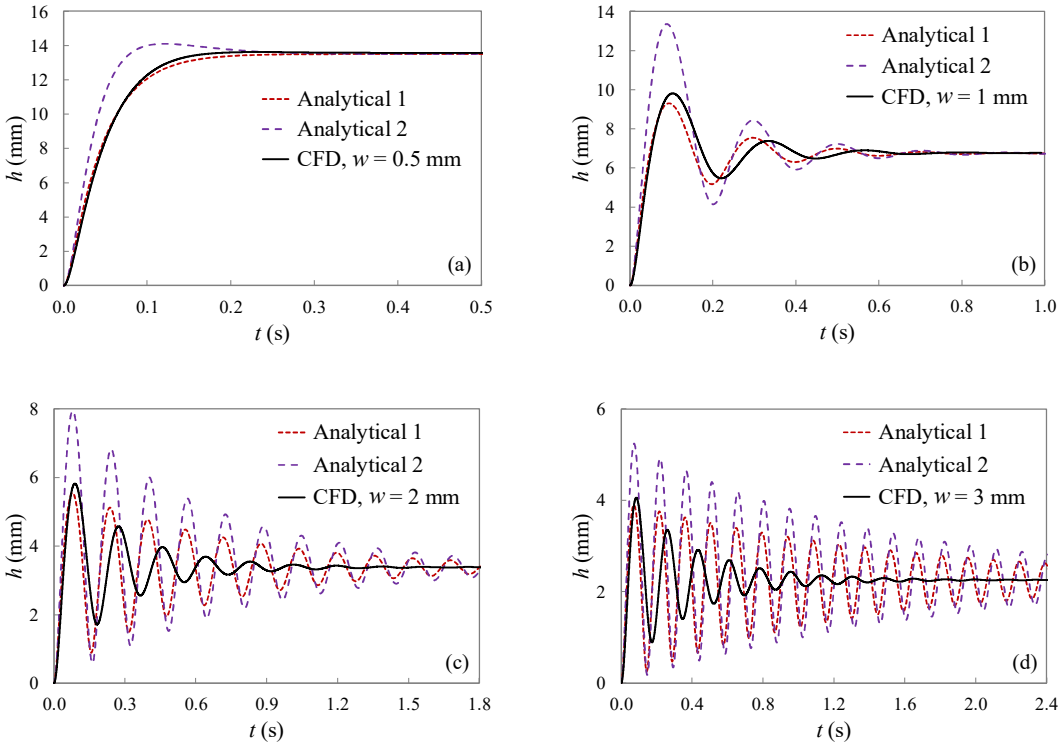

Fig. 3.9 Computationally and theoretically predicted water column height for silver plates for (a) w = 0.5 mm, (b) w = 1 mm, (c) w = 2 mm, and (d) w = 3 mm.

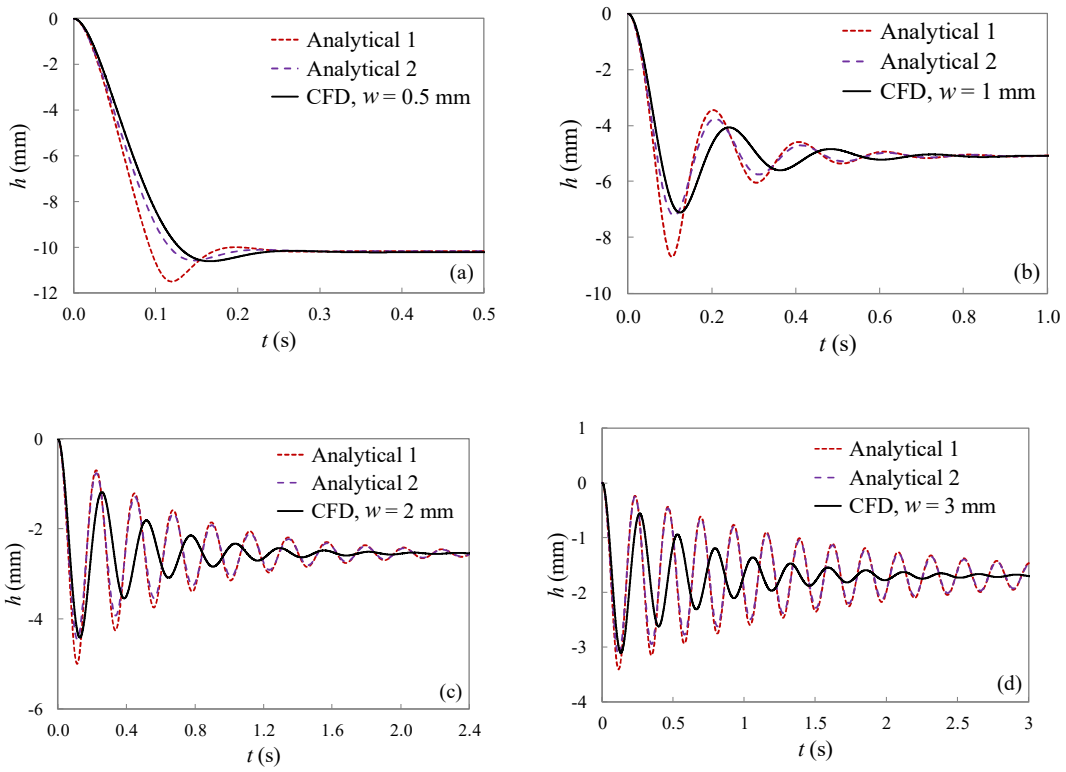

Fig. 3.10 Computationally and theoretically predicted water column height for Teflon plates for (a) w = 0.5 mm, (b) w = 1 mm, (c) w = 2 mm, and (d) w = 3 mm.

In order to obtain insight on the effect of wall spacing on the capillary penetration and depression, the computationally determined capillary height histories for silver and Teflon plates with various wall spacings are presented in Fig. 3.11. As evident, as the wall spacing is increased the equilibrium height is decreased, and a longer time is needed to reach equilibrium. This trend is consistent with previously reported results [29].

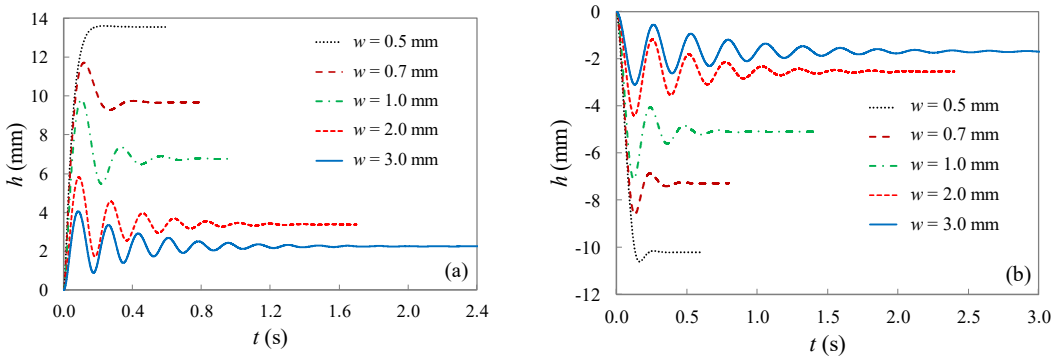

Fig. 3.11 Computational predictions of the capillary penetration of water between vertical parallel plates with various wall spacings, (a) silver and (b) Teflon plates.

To further examine the time needed to reach an equilibrium state, the equilibrium time, t_e, for various wall spacings for both hydrophilic and hyperbolic channels is shown in Fig. 3.12. To quantify the equilibrium time, a normalized oscillation amplitude was defined as the height difference between consecutive peaks and valleys of the $h(t)$ responses divided by the average height between that peak and valley, $NOA = 2\,(h_{max,i} - h_{min,i})/\left|h_{max,i} + h_{min,i}\right|$, where $h_{max,i}$ and $h_{min,i}$ are the capillary heights at peak and valley in the i^{th} half-cycle, respectively. As the time evolved, the first half-cycle in which NOA dropped below 1% was identified. During that half-cycle, the time at which the height reached the average height of the half-cycle was identified as the equilibrium time. Curve fitting was applied to the equilibrium data extracted from Fig. 3.11 to correlate the calculated equilibrium time with the wall spacing. As shown in the figure, the equilibrium time as a function of the wall spacing can be represented by quadratic and linear curves for the hydrophilic and hydrophobic capillary channels, respectively.

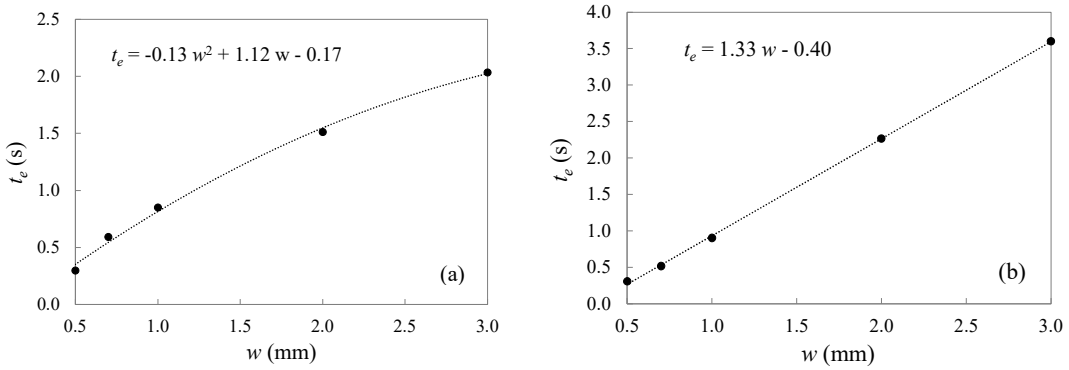

Fig. 3.12 The equilibrium time versus the wall spacings for (a) silver, and (b) Teflon plates.

Figure 3.13 shows the influence of the wall spacing on the dimensionless capillary pressure ($p^* = \Delta p_{cap} w/(2\sigma cos\theta)$) distribution along the dimensionless channel width, $x^* = x/w$, for both hydrophilic and hydrophobic wall cases. Note that a constant p^* along the channel width would correspond to a meniscus of constant curvature. As evident in Fig. 3.13a, the nondimensional pressure profile for w = 0.5 mm exhibits the least variation across the channel (the meniscus is closest to a circular arc). As the wall spacing increases, the pressure profile deviates more from a horizontal line, reflecting the stronger deviation of the meniscus shape from a circular arc. It is noted that as the wall spacing increased, the curvature at the center of the meniscus decreased, approaching a flat surface ($p^* \rightarrow 0$) in the limiting case of extremely large wall spacing.

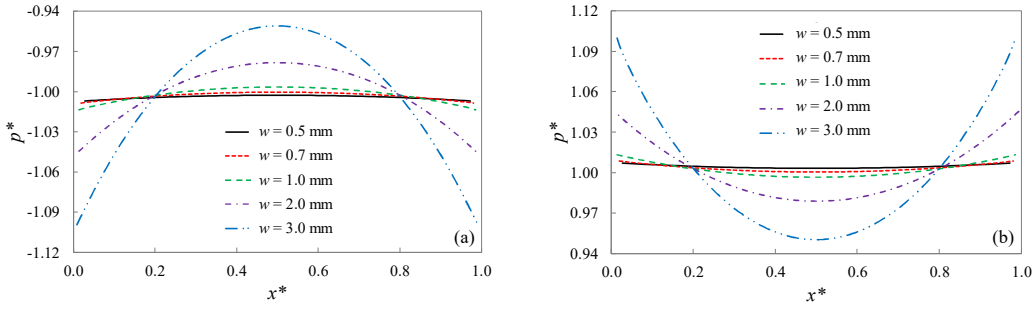

Fig. 3.13 Comparisons of normalized capillary pressure vs. normalized channel width for various wall spacings from w = 0.5 mm to w = 3 mm, (a) silver, and (b) Teflon plates.

3.5 Conclusions

A computational model has been developed to simulate the capillary penetration or depression of liquid between hydrophilic and hydrophobic vertical parallel plates with various wall spacings. A dynamic mesh method was employed to directly track the interface with no need for implicit interface tracking schemes. Excellent agreement was observed between the numerical predictions and the theoretical solutions for the steady-state capillary height and meniscus shape. The effect of the wall spacing on the dynamics of capillary flow was investigated. It was found that, as the wall spacing increased, the equilibrium height decreased and the time to reach equilibrium increased. The computational model was able to accurately predict the capillary penetration or depression regardless of the wall spacing, whereas the theoretical models fail to predict the dynamic response accurately for wider capillary channels. It was also shown that the meniscus shape deviated from circular arc as the wall spacing increased. An important feature of the present CFD model is the sharp interface

tracking and reconstruction. This feature might be particularly advantageous in problems involving interfacial heat and mass transfer where accurate specification of the interfacial fluxes is critical.

CHAPTER 4: A NOVEL COMPUTATIONAL MODEL OF THE DYNAMIC RESPONSE OF THE EVAPORATING LIQUID-VAPOR INTERFACE IN A CAPILLARY CHANNEL

In this chapter, the arbitrary-Lagrangian-Eulerian computational model discussed in the previous chapter is further extended to predict the dynamic response of an *evaporating meniscus* in the capillary flow of superheated liquids between vertical parallel plates.

4.1 Background

Interfacial liquid-vapor phase change phenomena play a significant role in a wide variety of natural and engineering systems, including transpiration in plants [73], membrane distillation [74], electronics cooling, and cooling devices such as heat pipes, capillary pumped loops, microfluidic devices, as well as in advanced energy systems and fuel cells [4,75–77]. There are several complex aspects involved in the fluid flow and heat transfer processes associated with the interfacial liquid-vapor phase change in capillary conduits including nonlinearity, transient behavior, interface displacement, dynamic interactions between the phases, and pressure as well as momentum jumps across the liquid-vapor interface. A substantial amount of research has been conducted on the hydrodynamic behavior of the meniscus in capillary structures. Lucas [26] and Washburn [27] established the first theoretical solutions to the problem of liquid rise in a capillary tube, neglecting the inertia effect. Thereafter, other researchers included the inertia effects in the Lucas-Washburn Equation (LWE) and extended the formulation, accounting for more effective factors and using various geometries for the capillary

channel [30,31,78,79]. Using the extended models, several detailed hydrodynamic aspects such as monotonic and oscillatory flow regimes and the transition between them were also investigated [59,71,80]. A relatively small number of studies have been conducted on the interfacial heat transfer and phase change at the meniscus. In the following discussion, some of the most relevant studies concerning the characteristics of liquid-vapor meniscus subject to phase change are reviewed.

Inspired by the transpiration phenomenon in plants, Rand [81] theoretically analyzed the dynamics of an evaporating pinned liquid-air meniscus in a vertical capillary glass tube. A nonlinear differential-integral equation was derived to describe the meniscus motion due to a step-change in the evaporation. The obtained governing equation was then linearized, yielding a nondimensional parameter which can be used as a criterion for the transition from monotonic to oscillatory behavior of the meniscus.

Ramon and Oron [32] pioneered the extension of the LWE [26,27] by including the effect of interfacial mass transfer due to phase change on the dynamic evolution of a completely wetting meniscus in a capillary tube. The evaporation was assumed to be driven by a constant temperature difference between the meniscus and the liquid in the capillary tube. The evaporation rate was calculated using an equation based on the kinetic theory [82]. It was argued that in the presence of either evaporation or condensation two mechanisms, mass transport and vapor recoil, determine the characteristics of the capillary flow such as equilibrium height, the transition threshold from monotonic to oscillatory regimes, and the frequency of the oscillations. It was also noted that if the phase change rate is high enough, instability could appear in the liquid oscillations.

In a related study, Sanches et al. [83] presented an analytical solution for the LWE coupled with a one-dimensional energy equation to investigate the penetration of a condensing meniscus in a capillary tube. The meniscus was assumed to be flat and at a constant saturation temperature. The authors analyzed the results of the moving interface subject to the condensation as a function of the non-dimensionalized parameters.

Polansky and Kaya [84] performed experiments associated with a modified LWE-type analytical model to study the dynamics of capillary rise under evaporation conditions using various liquids, capillary tube diameters, and thermal loads. Unlike the model developed by Roman and Oron [32], the mass flux at a flat liquid-vapor interface was assumed to vary with time by adding an asymptotic transient mass function. The results showed that predictions of the analytical model agreed with experimental results in the case of a 1 mm diameter capillary tube, while for capillary diameters of 0.5 mm and 2 mm a noticeable difference in the amplitude and phase of oscillations was observed between the analytical and experimental results. It was also found that modifications to the model did not reduce the discrepancy between the analytical and experimental results.

More recently, Benselama et al. [85] developed a theoretical model in the same framework as [21-23] to show the effect of an electric field on an evaporating dielectric liquid between metallic parallel plates (electrodes). Compared to the previous work of Ramon and Oron [32] that considered the recoil pressure term in the LWE, Benselama et al. [85] introduced an additional term for the electrostatic pressure due to the dielectrophoretic force. They also modified the momentum equation to include the

thermo-electrohydrodynamic effects. The electrodes used as the capillary channel walls were subjected to heat loads, and cryofreezing fluids (hfe-7100™ and hfe-7300™) were used as the working fluid. The contact angle was assumed to be constant. The findings revealed that the equilibrium height of the meniscus depends on both the applied electric field and the input heating power.

Rao et al. [86] experimentally studied the dynamics of thermally driven oscillatory flows in a vertical capillary tube including both evaporator and condenser sections, with the application of interest being pulsating heat pipes. Using a high-speed camera, the meniscus contact angles during downward and upward motions were measured. Antao et al. [87] examined the shape of evaporating liquid-vapor interfaces in silicon micropillar arrays using the transient laser interferometry technique. Deionized water was the working fluid. The evolution of the meniscus shape from flat to having a maximum curvature, and location of the meniscus were determined for various micropillar geometries and heating powers. Additionally, a computer code, Surface Evolver [88], was employed to solve the Young-Laplace equation to obtain the shape of the liquid-vapor interface by minimizing the surface energy.

Soma and Kunugi [89] experimentally evaluated the impact of macroscopic curvature and contact-line length on the evaporating meniscus of water located between vertical parallel glass plates with wall spacing from 0.3 mm to 1.5 mm. The plates were of 26 mm width, 76 mm height, and 1.0 mm thickness and the findings revealed that by increasing the curvature, the evaporation rate and the evaporation flux increased. In an experimental and theoretical study by the same researchers [90], evaporation in two capillary geometries, namely in a glass tube and between parallel plates, was studied.

The inner diameter of the capillary tube and the wall spacing of the parallel plates were identical. The variations of evaporation rate and flux with the meniscus shape were discussed, and an analytical scaling law was obtained to relate the rates and fluxes to the shapes.

Although there are several investigations of the steady-state evaporation from menisci having a prescribed fixed shape, only a few studies have focused on the transient response of evaporating menisci. Among them, none considers the evolution of the meniscus profile under evaporation. Moreover, to the authors' knowledge, no computational modeling of the transient response of an evaporating meniscus in capillary channels has been reported. Therefore, the objective of this study is to develop a computational model to directly simulate the dynamic response of the evaporating meniscus between parallel plates. The model removes the limitations of the theoretical treatments, such as the assumption of a fixed meniscus shape, specification of a pre-determined evaporation rate, and utilization of a simplified hydrodynamic model, by using a direct interface tracking method implemented on a deforming computational grid. Unlike the previous investigations, the meniscus shape and interfacial mass flow rate are not specified, but will be obtained as part of the solution of the problem. Once validated, the model is employed to conduct a detailed parametric study of the effects of wall spacing and liquid superheat on the dynamic response of the evaporating water meniscus.

The manuscript is organized as follows. In Section 4.2, the problem description is presented. The governing equations and associated boundary conditions, along with the numerical procedure are presented in Section 4.3. Specifically, an arbitrary Lagrangian-

Eulerian (ALE) approach, implemented in the commercial CFD package Ansys FLUENT 19.1, is employed to solve the governing equations. Section 4.4 presents the model validation, the simulation results, and related discussion. Concluding remarks are provided in Section 4.5.

4.2 Description of the Physical System

The two-dimensional computational domain of Fig. 4.1 consists of two infinitely wide vertical parallel plates with a spacing of w, partially dipped into a large reservoir containing liquid water. The infinitely thin parallel plates are assumed to have the wetting characteristics of copper and are 23 mm high in the y-direction, the bottom 3 mm of which is initially submerged in the liquid. The reservoir is 10 mm tall in the y-direction and has a length of 10 mm on each side of the capillary channel in the x-direction. Initially, the liquid height in the reservoir is 8 mm. Inside the reservoir, superheated liquid water is assumed to be in equilibrium with superheated water vapor that fills the top of the reservoir. Within the capillary channel, the meniscus is exposed to saturated water vapor filling the space above the meniscus. The initial shape of the liquid-vapor interface in the capillary channel is assumed to be flat (θ=90°) and is at the same height as the free surface of the liquid in the reservoir. The vapor in the reservoir and all the liquid in the computational domain are initially superheated, whereas the meniscus and the vapor above it in the capillary channel are at saturation temperature. To start the simulations, the contact angle between the interfacial control surfaces immediately adjacent to the wall is switched to the prescribed value, θ = 72° (relative to the vertical plane) which is for water in contact with the copper walls [91]. As the

simulation proceeds, the temperature difference between the superheated liquid in the capillary channel and the saturated vapor adjacent to the liquid-vapor interface drives the heat transfer and the related evaporation process. Both liquid and vapor are assumed to be incompressible Newtonian fluids with constant thermophysical properties, as listed in Table 4.1. A gravitational acceleration of 9.81 m/s^2 in the negative y-direction is specified.

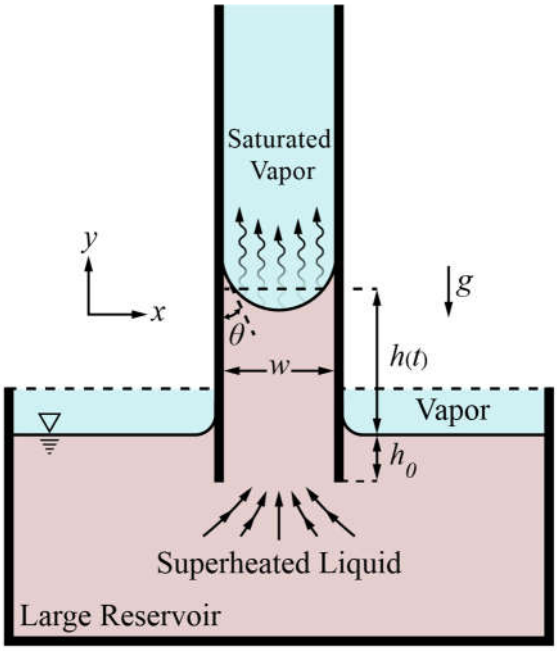

Fig. 4.1 Schematic of the partially wetting, evaporating liquid-vapor meniscus in a capillary channel.

Table 4.1 Thermophysical properties of liquid water and water vapor at 25°C [4].

	Water	
	Liquid	*Vapor*
Density, ρ (kg/m^3)	997.5	2.57×10^{-3}
Dynamic viscosity, μ (kg/m·s)	9.14×10^{-4}	9.88×10^{-3}
Latent heat of evaporation, h_{fg} (kJ/kg)	2442	-
Molecular weight, M_w (kg/kmol)	18	18
Specific heat, c_p (J/kg·K)	4183	1912
Surface tension, σ (N/m)	0.072	-
Thermal conductivity, k (W/m·K)	0.61	1.86×10^{-2}

4.3 Governing Equations and Numerical Methodology

The governing equations, boundary and initial conditions, and details of the computational model and specific treatment of evaporation at the liquid-vapor interface are now presented.

4.3.1 Governing Equations

The following assumptions are made in the development of the computational model. Both the liquid and vapor are considered to be Newtonian fluids with constant thermophysical properties, the flow is laminar and incompressible, and viscous dissipation as well as natural convection are negligible. Furthermore, since the widths of capillary channels studied range from 0.3 to 0.7 mm, the influence of intermolecular

forces on the evaporation heat transfer rate from the meniscus is assumed to be negligible [92].

Considering the preceding assumptions, the two-dimensional, time-dependent conservation equations for mass, momentum, and energy in the ALE framework are [21]:

$$\rho \nabla \cdot \mathbf{V} + S_{mass} = 0 \tag{4.1}$$

$$\rho \left[\left. \frac{\partial \mathbf{V}}{\partial t} \right|_{ref} + \left((\mathbf{V} - \mathbf{V}_m) \cdot \nabla \right) \mathbf{V} \right] = -\nabla p + \mu \, \nabla^2 \mathbf{V} + \rho \mathbf{g} \tag{4.2}$$

$$\rho c_p \left[\left. \frac{\partial T}{\partial t} \right|_{ref} + (\mathbf{V} - \mathbf{V}_m) \cdot \nabla T \right] = k \, \nabla^2 T \tag{4.3}$$

where t, ρ, k, c_p, and μ are time, density, thermal conductivity, specific heat at constant pressure, and dynamic viscosity, p and T are the pressure and temperature, and $\mathbf{V}$ and $\mathbf{V}_m$ are the fluid velocity and mesh velocity vectors in the spatial domain, respectively, S_{mass} is the volumetric mass source term, and $\mathbf{g}$ is the gravity vector. Equations (4.1) - (4.3) are applied to both the liquid and the vapor throughout the entire computational domain. Boundary and initial conditions are presented in Section 4.3. It is noted that S_{mass} in Eq. (4.1) is zero everywhere except in the vapor domain adjacent to the meniscus.

The first terms in the LHS of Eqs. (4.2) and (4.3) represent the time derivative in the *referential domain* (i.e., the coordinate system that coincides with the moving mesh). Moreover, $\mathbf{V} - \mathbf{V}_m$ represents the *advective velocity*, that is, the relative velocity between the fluid and the mesh. Thus, the arbitrary motion of the computational mesh is only reflected in the LHS of the momentum and energy equations [21].

Unlike the liquid-vapor interface in the capillary channel that is tracked directly using the dynamic mesh, the liquid-vapor interface in the reservoir is captured using the VOF method with a fixed grid [15]. The liquid volume fraction, ε_l , distribution in the reservoir is determined by solving the following scalar transport equation:

$$\frac{\partial \varepsilon_l}{\partial t} + \mathbf{V} \cdot \nabla \varepsilon_l = 0 \tag{4.4}$$

where ε_l is the ratio of the computational cell's volume occupied by liquid to its total volume. Obviously, the volume fraction of vapor satisfies $\varepsilon_v = 1 - \varepsilon_l$. No evaporation occurs in the reservoir since the liquid and vapor are in thermal equilibrium.

4.3.2 Computational Domain

In this study, the computational domain is divided into two subdomains: Ω_v which includes the saturated vapor above the liquid in the capillary channel, and Ω_l which contains the rest of the system, i.e., all the liquid and the superheated vapor in the reservoir. In the following, the term *liquid subdomain* refers to Ω_l. As noted previously, the flow and energy equations are solved for both Ω_l and Ω_v. The two subdomains share the liquid-vapor interface (Γ_{l-v}) in the capillary channel as their common boundary ($\Gamma_{l-v} = \Omega_l \cap \Omega_v$). Figure 4.2 shows the schematic view of the overlapped interfaces of Ω_l and Ω_v. The two subdomains are coupled through boundary conditions applied at the meniscus whose time-varying shape and position is determined by solving for the flow field in Ω_l under a spatially varying and time-dependent pressure boundary condition applied along the meniscus. Once the updated positions of all the interfacial nodes are determined at any time, *t*, the grid is deformed in both subdomains to move the meniscus to the new position at time $t+\Delta t$.

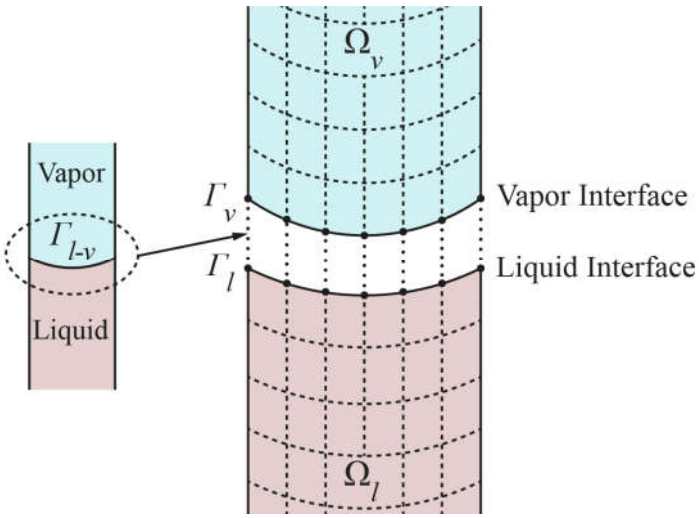

Fig. 4.2 Representation of computational subdomains in the vicinity of the liquid-vapor interface.

4.3.3 Boundary, Initial, and Interfacial Conditions

An initial velocity of zero is applied throughout the entire domain. No-slip and adiabatic conditions are applied at the interior vertical wall surfaces of the capillary channel and the reservoir walls. However, the moving contact line between the meniscus and the capillary channel walls is treated differently since the no-slip boundary condition is not valid due to the singularity in the viscous stress [65,66]. Specifically, the prescribed contact angle at the two interfacial control surfaces adjacent to the walls is imposed by incorporating a User-Defined-Function (UDF) developed in C++. The computational nodes representing the contact line are moved along the wall at the same velocity as the liquid flow in the control volume adjacent to the wall. This approach is more accurate than the traditional CFD models of the capillary flow, such as VOF-based models, since it removes the unrealistic no-slip condition at the contact line. It is noted that the present model does not incorporate the assumption of a constant pressure difference across the

meniscus along its length. Instead, the local pressure differences across each interfacial control surface are calculated based on the local curvature of the meniscus and the local pressure exerted by the vapor. Furthermore, unlike previous studies where a fixed meniscus shape was prescribed throughout the entire simulation [59,83], the evolution of the meniscus shape in the current simulation is obtained as a part of the solution. Finally, a gauge pressure of zero is applied at the top boundaries of the vapor subdomain and reservoir. Detailed discussion of the hydrodynamic component of the modeling is presented elsewhere by the authors [93,94]. At the top boundaries of the vapor subdomain and the reservoir, constant temperatures equal to saturation temperature and superheated temperature are imposed, respectively.

4.3.3.1 Heat Transfer, Mass Flux, and Boundary Conditions at the Liquid-Vapor Meniscus

Meniscus boundary conditions in the vapor subdomain:

As noted in Section 4.3.2, the liquid-vapor interface in the capillary channel links the two computational subdomains and represents two overlapping boundaries for the liquid and vapor subdomains to which different boundary conditions are applied. In Ω_v, the meniscus is treated as a no-slip wall boundary condition that is impermeable to flow. The vapor generation due to evaporation is simulated using a vapor mass source term applied to the first layer of vapor cells adjacent to the meniscus. The temperature of the meniscus in Ω_v is calculated as the saturation temperature corresponding to the local vapor pressure. It is noted that the vapor pressure changes along the vapor subdomain are found to be negligibly small compared to the operating vapor pressure.

Meniscus boundary conditions in the liquid subdomain:

The meniscus in Ω_l is treated with a pressure boundary condition. The value of the pressure is obtained from the application of the Young-Laplace equation at each interfacial control surface, superimposed with the vapor pressure exerted on the meniscus. In each time-step, the capillary pressure difference across each interfacial control surface is calculated using the local curvature of the liquid interface by applying the Laplace equation [93]. The pressure exerted on the meniscus by the vapor is obtained from the solution of the vapor flow field. This pressure stems from the forces attributed to the momentum of the vapor ejected from the evaporating meniscus, and the vapor pressure buildup adjacent to the meniscus to overcome the shear force at the interface of the vapor and the channel wall. The meniscus temperature in the liquid subdomain is the same as in the vapor subdomain, that is, it is the saturation temperature at the corresponding vapor pressure. The saturation temperature boundary condition in the liquid subdomain is implemented by creating a very thin layer of cells (3 μm thick) adjacent to the meniscus, as illustrated in Fig. 4.3. The saturation temperature throughout this layer is enforced using an energy source term applied via a UDF. Further, the effects of hydrostatic vapor pressure on the meniscus are neglected.

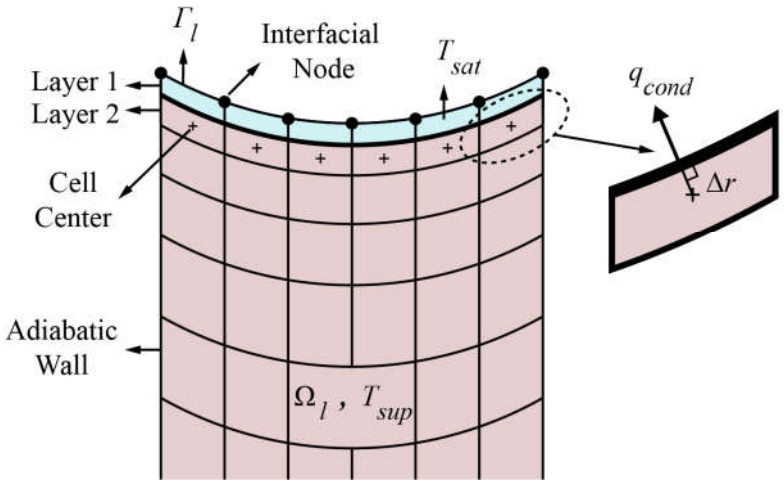

Fig. 4.3 Thermal boundary condition imposed at the liquid-vapor meniscus in the liquid subdomain.

Evaporation rate at the meniscus:

The evaporation is driven by applying initial liquid superheats ranging from 1 K to 5 K throughout the entire domain, except at the meniscus boundary that is maintained at the saturation temperature. The amount of liquid in the reservoir is relatively large, therefore its temperature is maintained at the superheated value throughout the entire evaporation process.

For the calculation of the interfacial heat transfer rate, the shortest distance between the cell-centroids of the second layer of cells adjacent to the meniscus and the common faces between the first and second layers is calculated (see Fig. 4.3). The local heat transfer rate reaching each of the interfacial control surfaces is obtained from:

$$q_{cond} = k_l A \frac{\Delta T}{\Delta r} \tag{4.5}$$

where, k_{liq}, A, and Δr refer to the liquid thermal conductivity, the surface area per unit depth of the control surface between the first and second layers of cells adjacent to the

meniscus, and the shortest distance between the cell-centroids of the second layer and the common faces of the first and second layers, respectively.

Once the heat transfer rate per unit depth is known, the local evaporation rate per unit depth from each interfacial control surfaces is obtained from:

$$\dot{m}_{evp} = \frac{q_{cond}}{h_{fg}} \tag{4.6}$$

where h_{fg} is the latent heat of vaporization. The corresponding local vapor mass source applied to the first layer of vapor cells adjacent to the meniscus is:

$$S_{mass} = \dot{m}_{evp}/V_{cell} \tag{4.7}$$

where S_{mass} and V_{cell} denote the local mass source term and volume of the related control volume in the vapor subdomain, respectively. No mass source was employed in the liquid subdomain to mimic the mass loss due to evaporation. Instead, the local evaporating velocity based on the local evaporation rate is calculated and assigned to the meniscus to account for the receding meniscus velocity due to evaporation:

$$V_{evp} = -\dot{m}_{evp}/\rho_l A_y \tag{4.8}$$

where A_y is the y-component of the interfacial control surfaces.

Net velocity of the evaporating meniscus

The *mass removal velocity*, which represents the rate of recession of the meniscus height due to mass removal by evaporation, is applied to the interfacial nodes and is always downward regardless of whether the meniscus is rising or falling. The net velocity of each node on the evaporative meniscus is determined as:

$$V_{node} = V_{cap} + V_{mr} \tag{4.9}$$

where V_{cap} is the capillary-induced meniscus velocity with no heat transfer effects, and V_{mr} is the receding component of the meniscus velocity due to evaporation. It is noted that the evaporated liquid leaves the computational model from the top of the capillary channel, and vapor enters the domain from the top of the reservoir to replace the evaporated liquid. Overall, the total mass contained in the computational domain decreases over time as liquid is replaced by vapor in the reservoir.

4.4 Numerical Model Validation, Results, and Discussion

The governing equations are solved using a pressure-based finite volume scheme implemented in the commercial CFD package Ansys FLUENT 19.1. The pressure and velocity were coupled through the SIMPLE algorithm [67]. The advective terms in the governing equations were discretized using the Quick differencing scheme while a PRESTO! method was chosen for evaluation of the pressure gradient term. Also, the compressive scheme was used to discretize the volume fraction equation. An implicit scheme was adopted for discretization in time. Several UDFs were created and hooked to the solver for (*i*) specification of the time-dependent pressure boundary condition at the meniscus, (*ii*) movement of the meniscus in each time step, (*iii*) specification of the evaporation rate from the meniscus and the corresponding vapor generation, and (*iv*) the enforcement of the saturation temperature at the meniscus. Under-relaxation factors of 0.2, 0.4, and 0.6 were employed for the solution of the pressure, momentum, and energy equations, respectively. The solution was considered to be converged in each time step when the scaled residual decreased to 10^{-5} for the continuity, momentum, and energy equations.

4.4.1 Grid and Time Step Size Independence

A multi-block structured mesh with tetrahedral elements was created. The mesh resolution was increased within the capillary channel, specifically in the vicinity of the channel entrance region within the reservoir and adjacent to the liquid-vapor interface where the largest gradients of velocity and temperature occur. A boundary layer mesh was created on both sides of the meniscus. In order to achieve grid-independent numerical results, the effect of grid size on the transient capillary height, h, was examined for a liquid superheat of $\Delta T = 2$ K, and the results are shown in Fig. 4.4. Note that the capillary height is defined as the average meniscus height above the liquid free surface in the reservoir. As can be observed from close inspection of this figure, the refinement of the grid from $N = 40$ cells to $N = 50$ cells along the width of the capillary channel and simultaneously in the y-direction does not significantly affect the results. Thus, a grid consisting of 40 cells across the channel is considered to yield grid-independent results. A time-step size independence study was also performed, and $\Delta t = 10^{-5}$ s was determined to be the optimal time-step size for the simulations.

It is noted that a channel width of 0.5 mm was used as the benchmark in Fig. 4.4, and the cell size that was found to yield grid-independent results guided the mesh creation for both smaller and larger wall spacings. To this end, the grid for the wall spacing values of $w = 0.3$ mm and $w = 0.7$ mm contained 24 and 56 cells along the width of the capillary channel, respectively.

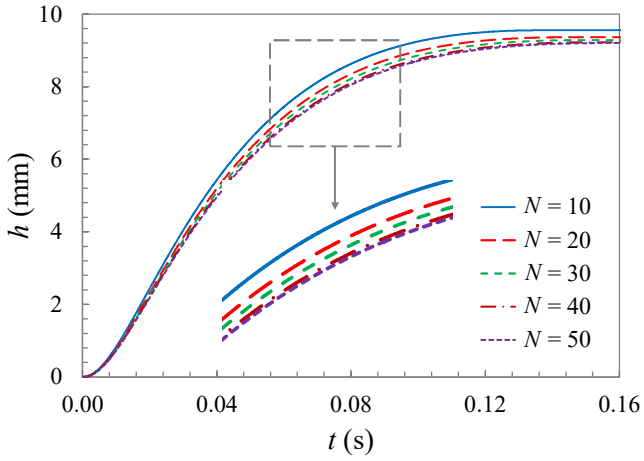

Fig. 4.4 Grid independence test for the capillary height vs. time for wall spacing of $w = 0.5$ mm, $\Delta t = 10^{-5}$ s, and $\Delta T = 2$ K.

4.4.2 Model Validation

In the absence of experimental data on the evaporating capillary flow between infinitely long parallel plates, the present numerical model was validated by comparing the predicted equilibrium liquid height to those obtained from theoretical models developed for an evaporating meniscus involving superheated liquids. These models usually use LWE-type equations to describe the capillary flow and use a kinetic theory-based equation (Eq. 2.11 of Section 2.2) for calculation of the evaporation rate. One of the caveats of the widely used kinetic theory-based equation for the calculation of the evaporation rate is the presence of an empirically determined accommodation coefficient, α. This accommodation coefficient is a measure of deviation from the maximum evaporation rate predicted by the kinetic theory, caused by the reflection of vapor molecules at the interface. Various studies have utilized different definitions and a wide range of accommodation coefficients have been used that span three orders of magnitude [34,95–97]. Moreover, the accommodation coefficient varies as different

fluids and solid-liquid interactions are considered. A similar theoretical model was developed by the authors and was employed for validation of the present CFD model. A detailed description of the theoretical model used here was presented in Section 2.2. Since the present CFD model accounts for the thermal diffusion phenomenon adjacent to the meniscus, the temperature gradient at the interface is significantly smaller than the jump condition considered in the theoretical models. Thus, to be consistent with the theoretical solution presented in Section 2.2, a specific CFD case, hereafter referred to as the *modified CFD model*, was simulated in which a fixed temperature jump equal to the degree of superheat of the liquid was enforced across the interface, thereby eliminating the effect of thermal diffusion in the vicinity of the meniscus. To do so, an energy source term was applied in the first layer of control volumes adjacent to the meniscus in the liquid subdomain to create a temperature difference equal to the superheat degree between the meniscus and the underlying liquid. Furthermore, since the effect of vapor viscous drag on the moving meniscus is not considered in the mathematical solution, the capillary channel walls in the vapor subdomain were prescribed with zero-shear stress boundary conditions for consistency of the comparison.

Figure 4.5 compares predictions of the transient response of the capillary height obtained using the modified CFD model (with no thermal diffusion) and the theoretical model of Section 2.2. Three liquid superheat conditions of $\Delta T = 0$ K (non-evaporating), 2 K, and 3 K, and two wall spacings of $w = 0.5$ mm and $w = 0.7$ mm are considered.

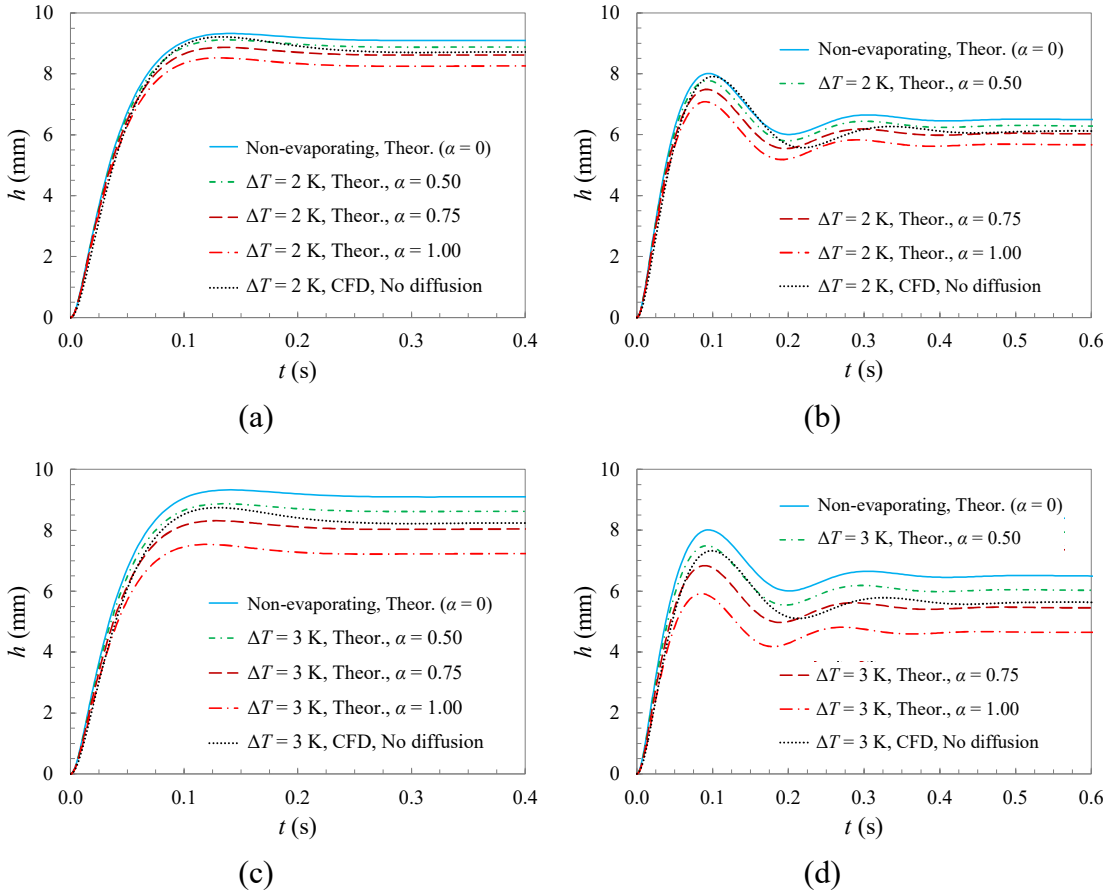

Fig. 4.5 Comparison of computationally determined capillary heights for $\Delta T = 2$ K and $\Delta T = 3$ K without thermal diffusion to theoretically determined capillary heights with various α, (a) and (c) $w = 0.5$ mm, (b) and (d) $w = 0.7$ mm.

As evident, the theoretical results underpredict the maximum capillary height for the non-evaporating case ($\Delta T = 0$ K) compared to the CFD results, and this discrepancy increases with increasing wall spacing. This trend is consistent with previous results [93]. However, the computational and theoretical results are in excellent agreement at steady state.

Table 4.2 lists the equilibrium height of the evaporating water column as obtained from the modified CFD model ($h_{ss,CFD}$), the corresponding theoretical values obtained using

various accommodation coefficients, α ($h_{ss,theor}$), and the normalized difference between the theoretical and computational values (Δh_{ss} = ($h_{ss,theor}$ - $h_{ss,CFD}$)/ $h_{ss,theor}$). The results are related to superheat degrees of ΔT = 2 K and ΔT = 3 K with wall spacings of w = 0.5 mm and w = 0.7 mm.

It can be observed from Fig. 4.5 that, for all cases, $h_{ss,CFD}$ lies between theoretical solutions with accommodation coefficients of $\alpha = 0.5$ and $\alpha = 0.75$. For superheat degrees of ΔT = 2 K and ΔT = 3 K with wall spacings of w = 0.5 mm and w = 0.7 mm, the values of α for which the theoretical results h_{ss} are within 1% of those predicted by the modified CFD model are presented in Table 4.3. Overall, the results presented in Tables 4.2 and 4.3 show that the CFD predictions are in general agreement with those of theoretical model when similar assumptions are adopted.

Table 4.2 Comparison of h_{ss} for the evaporating cases (ΔT = 2 K and ΔT = 3 K) obtained from the modified CFD model to theoretical results with w = 0.5 mm and w = 0.7 mm.

	α	w	h_{ss} ΔT = 2 K	$\frac{h_{ss,theor} - h_{ss,CFD}}{h_{ss,theor}}$ ΔT = 3 K	h_{ss} ΔT = 3 K	$\frac{h_{ss,theor} - h_{ss,CFD}}{h_{ss,theor}}$ ΔT = 3 K
CFD	-	0.5	8.718	-	8.239	-
Theor.	0.25		9.041	3.57%	8.974	8.19%
	0.50		8.882	1.85%	8.621	4.26%
	0.75		8.621	-1.13%	8.040	-2.48%
	1.00		8.259	-5.56%	7.231	-13.94%
CFD	-	0.7	6.122	-	5.633	-
Theor.	0.25		6.441	4.95%	6.376	11.65%
	0.50		6.286	2.61%	6.028	6.55%
	0.75		6.028	-1.56%	5.452	-3.32%
	1.00		5.669	-7.99%	4.650	-21.14%

Table 4.3 Estimated values of α obtained from the modified CFD model for ΔT = 2 K and ΔT = 3 K and w = 0.5 mm and w = 0.7 mm.

	Estimated α using CFD model	
	w = 0.5 mm	w = 0.7 mm
ΔT = 2 K	0.657	0.659
ΔT = 3 K	0.664	0.671

4.4.3 Transient Meniscus Shape and Capillary Penetration

Figure 4.6 reveals the detailed meniscus shape and the computational mesh near the meniscus for both liquid and vapor domains for the case of $\Delta T = 2$ K at various times. It is evident that the initially flat meniscus evolves to a developed state rapidly ($t \approx 0.5$ ms) compared to the equilibrium time ($t \approx 0.5$ s) making the overall system response relatively insensitive to the initial specified shape.

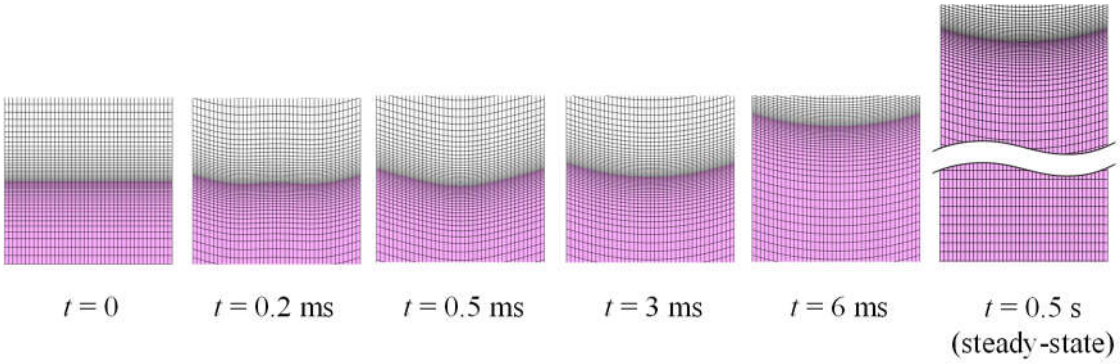

Fig. 4.6 Time evolution of dynamic mesh in the vicinity of the liquid-vapor interface for both liquid and vapor subdomains with $w = 0.5$ mm and $\Delta T = 2$ K.

The wall spacing and liquid superheat were varied to determine their influence on evaporation from the liquid-vapor meniscus. Figure 4.7 shows the computationally determined transient capillary penetration height of an evaporating meniscus for various degrees of superheat, including a superheat of zero (non-evaporating case). The predicted responses indicate that, in all cases, increasing evaporation rates reduce the capillary rise, as expected. The influence of evaporation is more significant at early times and the capillary height depression is more profound for smaller wall spacing. At steady state, the capillary height difference between the evaporating and non-

evaporating cases is relatively small. This behavior is in contradiction with the results of Fig. 4.5 for the modified CFD model (no thermal diffusion), as well as with the theoretical modeling results for which a noticeable difference existed between the steady-state capillary heights of evaporating and non-evaporating menisci [32]. The difference between the steady-state results of Figs. 4.5 and 4.7 highlights the important role of thermal diffusion in the vicinity of the meniscus on the overall hydrodynamic response of the evaporating meniscus.

Computationally determined transient capillary penetration heights for the non-evaporating case and for the evaporating meniscus at $\Delta T = 5$ K for wall spacings of $w =$ 0.3 mm, 0.5 mm, and 0.7 mm are shown in Fig. 4.8. As evident in all cases, as the capillary penetration progresses the deviation between the capillary height of non-evaporating and evaporating cases approaches zero. This is due to the fact that as the interfacial temperature gradient decreases with time due to thermal diffusion, the evaporation rate diminishes, and all cases approach the non-evaporating condition. It is evident that for $w = 0.5$ mm, unlike the non-evaporating case where a peak in the capillary heigh is observed at $t \approx 0.12$ s, the height of the evaporating meniscus exhibits a monotonic rise until it reaches steady-state. Also, for $w = 0.7$ mm, evaporation decreases the amplitude of oscillations compared to the non-evaporating case. As such, it can be inferred that when the flow regime is oscillatory, evaporation tends to dampen the oscillations.

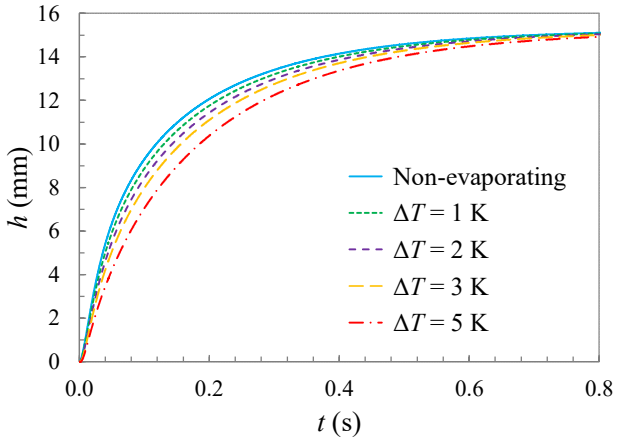

(a)

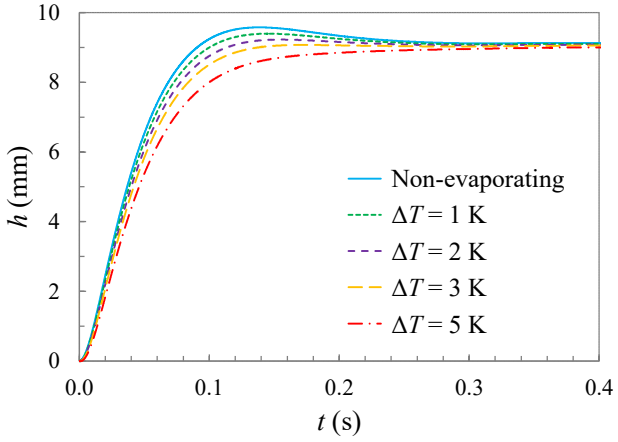

(b)

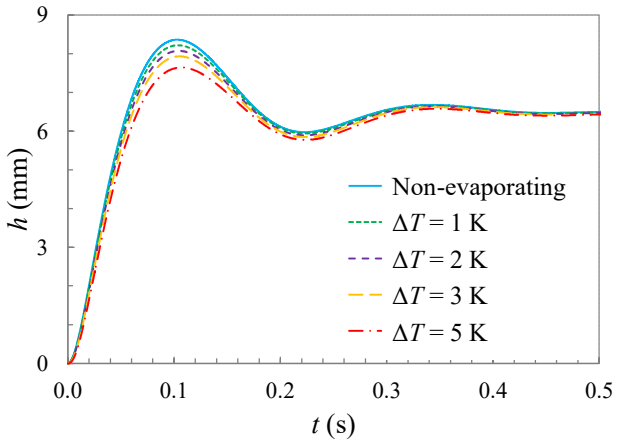

(c)

Fig. 4.7 Computational predictions of the capillary penetration of non-evaporating and evaporating water menisci for various degrees of superheat and (a) $w = 0.3$ mm, (b) $w = 0.5$ mm, and (c) $w = 0.7$ mm.

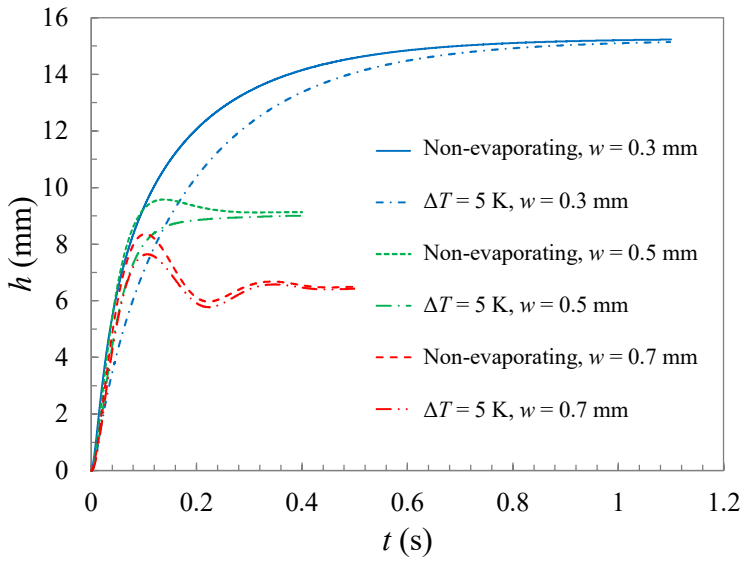

Fig. 4.8 Computational predictions of the capillary penetration of non-evaporating and evaporating water menisci with $\Delta T = 5$ K between vertical parallel copper plates with various wall spacings.

4.4.4 Transient Thermal Response at the Meniscus

As discussed previously, the thermal energy reaching the meniscus from the liquid side drives evaporation. The average heat fluxes along the meniscus are shown in Fig. 4.9 for various degrees of superheat. As evident, heat transfer rates are proportional to the liquid superheat and decrease with time. This is attributed to the thermal diffusion adjacent to the meniscus being driven by the temperature difference between the superheated liquid and the interface which is at the saturation temperature. In general, there are two competing effects controlling the heat transfer rate to the meniscus, namely the thermal diffusion adjacent to the meniscus, and the liquid delivery to the meniscus to sustain the evaporation. The former tends to lower the temperature of the liquid near the meniscus, whereas the latter increases the temperature near the meniscus

by delivery of superheated liquid. The liquid flow to the meniscus is driven by evaporation and depends on the interfacial temperature gradient that is inversely proportional to the intensity of the thermal diffusion effects. As such, the thermal diffusion adjacent to the meniscus and the liquid delivery to the meniscus are coupled. Results shown in Fig. 4.9 suggest that as the capillary penetration progresses, the diffusion effect prevails and the heat transfer rate to the meniscus decreases gradually.

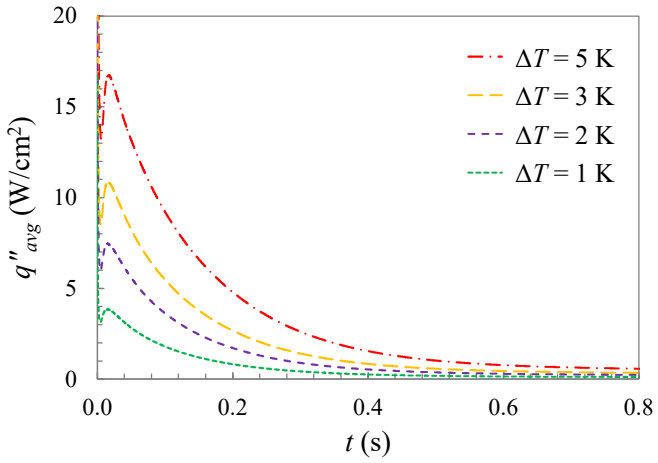

(a)

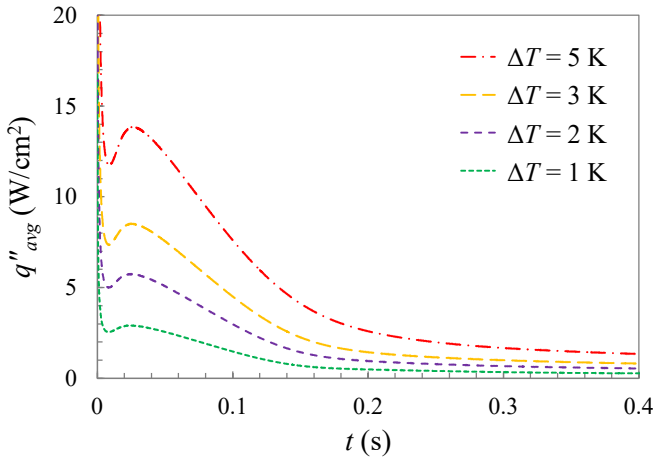

(b)

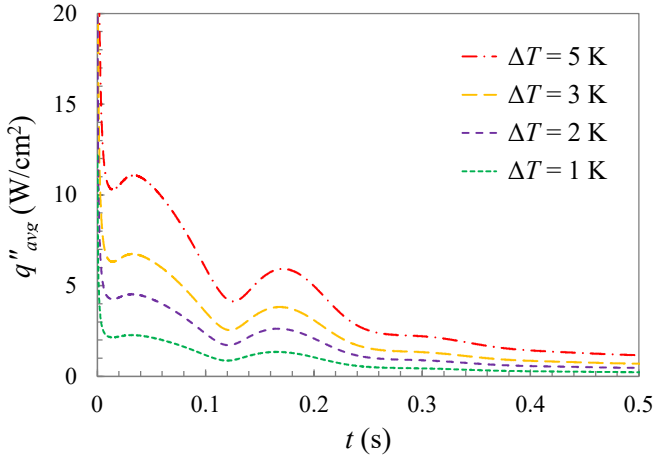

(c)

Fig. 4.9 Computationally predicted average interfacial heat flux for various degrees of superheat with (a) w = 0.3 mm, (b) w = 0.5 mm, and (c) w = 0.7 mm.

4.4.5 Transient Liquid Velocity and Thermal Response

Figure 4.10 shows the *y*-velocity contours in the upper part of the liquid column at various times for various wall spacings and $\Delta T = 2$ K. Note that the channel widths for various wall spacings are normalized to be identical. Inspection of the velocity contours at the two ends of the meniscus shows that the model successfully captures the slip condition at the contact line of the advancing (or receding) evaporating meniscus and the walls. The monotonic (Fig. 4.7a, $w = 0.3$ mm) and oscillatory (Fig. 4.7b, $w = 0.5$ mm and Fig. 4.7c, $w = 0.7$ mm) flow regimes are also reflected in the velocity contours. The occurrence and strength of the oscillations, which are asymmetric in nature, are generally a function of the liquid properties, the solid-liquid interaction, and the capillary channel spacing. For each wall spacing the contours at $t = 0.7$ s show near steady state conditions with vanishing velocities. Also, at $t = 0.001$ s, the boundary layer thicknesses along the walls are growing in time for all the cases, and over time the velocity field which is not in the immediate vicinity of the meniscus exhibits nearly fully developed parabolic axial velocity distribution behavior with the maximum velocity at the center of the channel.

Figure 4.11 shows the evolution of the temperature field near the meniscus for various wall spacings and $\Delta T = 2$ K. As discussed earlier, the temperature of the liquid-vapor interface is equal to the saturation temperature at the corresponding vapor pressure, which results in large thermal diffusion rates near the interface. As observed in Fig. 4.11, the relatively low temperature of the meniscus propagates downward with time.

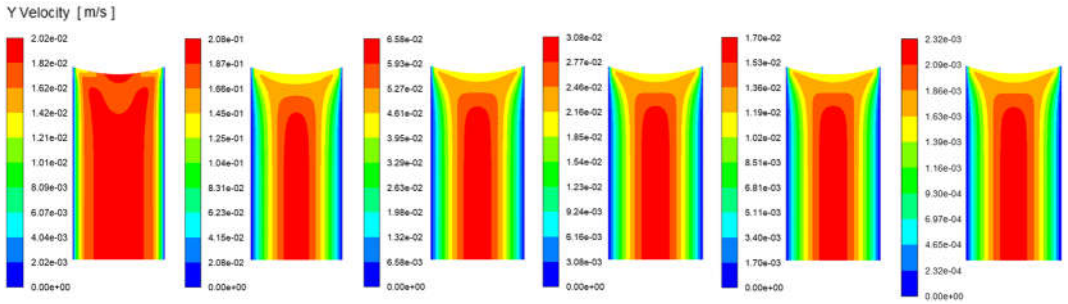

(a) $w = 0.3$ mm

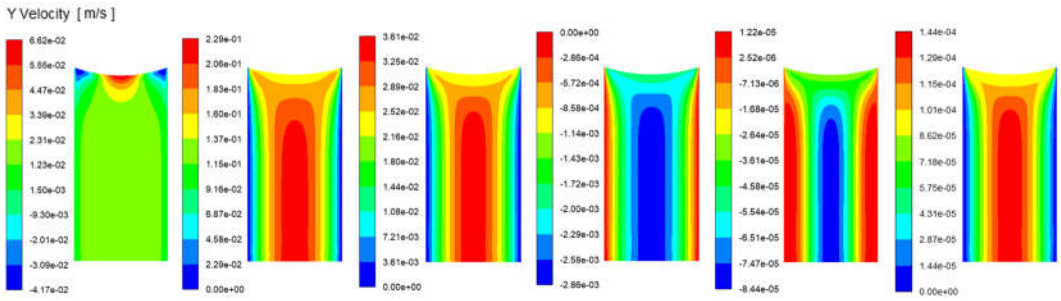

(b) $w = 0.5$ mm

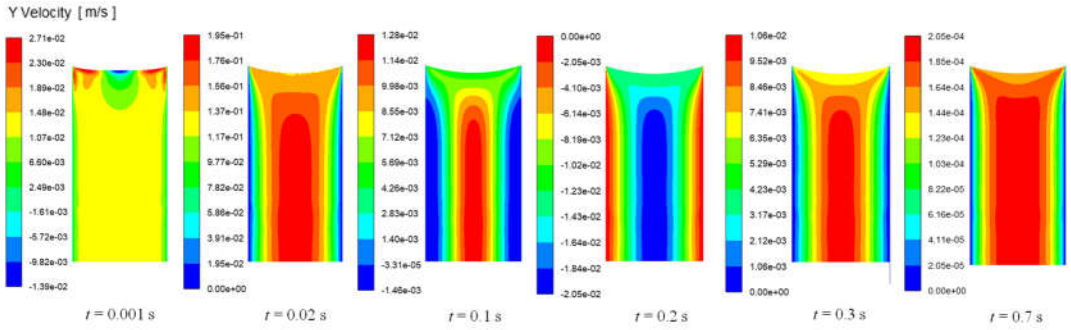

(c) $w = 0.7$ mm

Fig. 4.10 Evolution of the y-velocity field near the evaporating meniscus for various wall spacings and $\Delta T = 2$ K.

Inspection of temperatures in the upper part of the liquid column in Fig. 4.11 also reveals that, during the upward motion of the flow the fluid temperature in the central zone of the channel exceeds that of the fluid near the walls. As the meniscus rises,

relatively hot liquid from the lower part of the channel and reservoir is pulled upward. In the region near the channel walls and close to the meniscus, the velocity of the liquid is relatively small, and the liquid initially at temperatures close to that of the meniscus will take longer to be replaced with relatively hot liquid from the lower part of the channel and the reservoir. For $w = 0.7$ mm at $t = 0.2$ s, unlike other times shown the top middle region of the channel has a low temperature relative to that of the liquid next to the channel walls. To explain this temperature distribution, attention should be paid to the velocity contours in the top part of the capillary channel shown in Fig. 4.10. Near the meniscus, the velocity is relatively uniformly distributed across the channel. However, farther from the meniscus, the velocity profile approaches a parabolic shape. Thus, during the downward motion of the meniscus, flow is funneled from the near-wall region in the vicinity of the meniscus to the channel center. Since the temperature close to the meniscus is relatively small, the flow funneled to the channel center advects the relatively cold temperature down the channel center. It is noted, that at the same time ($t = 0.2$ s) for $w = 0.5$ the liquid is also moving downward, however, the temperature contours are not showing the same pattern as for $w = 0.7$. This can be explained by comparing the velocities shown in Fig. 4.10 for $w = 0.5$ mm and $w = 0.7$ mm at $t = 0.2$ s. As can be seen, the downward velocity for $w = 0.7$ mm at $t = 0.2$ s is an order of magnitude greater than that for $w = 0.5$ mm. Thus, the advection of the relatively cold liquid down the channel center is significantly stronger for $w = 0.7$ s. For $w = 0.7$ mm at $t = 0.3$ s, as the flow direction changed, the relatively warm liquid that moves upward from inside the reservoir acts against thermal diffusion and leads to increase in the temperature in the middle zone of the capillary channel. For $w = 0.5$ mm and $w = 0.7$

mm at $t = 0.7$ s, since the flow reaches steady state, the temperature distribution is more uniformly distributed across the channel width.

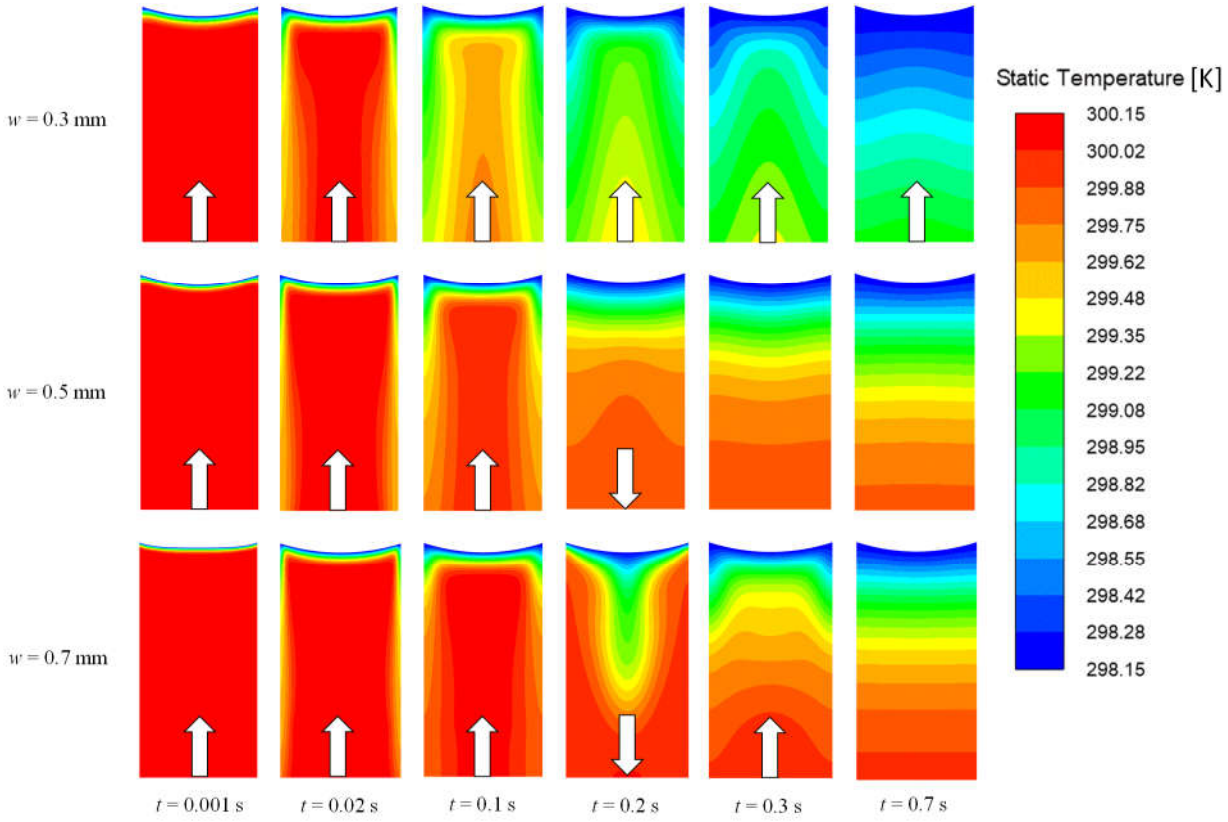

Fig. 4.11 Evolution of the temperature field near the evaporating meniscus for various wall spacings and $\Delta T = 2$ K. Arrows show the direction of the mean y-velocity in the capillary channel.

Figure 4.12 shows local heat flux variations along the evaporating meniscus at various times and wall spacings for $\Delta T = 2$ K. The content of Fig. 4.12a implies that the maximum local heat flux (i.e., evaporation rate) occurs at the center of the meniscus which corresponds to the higher temperature of the liquid at this location (Fig. 4.10). As the thermal diffusion in the vicinity of the meniscus weakens over time, the rate of

change of local heat flux along the meniscus decreases, and the heat flux becomes more uniformly distributed. A similar trend is observed for wall spacings of 0.5 mm and 0.7 mm; however, the meniscus experiences smaller local heat fluxes at larger wall spacings. The smaller heat fluxes associated with larger wall spacings are attributed to the opposing effects of thermal diffusion and upward velocity that tend to decrease and increase the temperature near the meniscus, respectively. Whereas the former is independent of the channel width, the latter decreases with increasing the channel width. As such, at larger wall spacings, the cooling effect of thermal diffusion is more dominant than the heating effect associated with the upward velocity, leading to comparatively smaller heat fluxes. As evident in Fig. 4.12c, the local heat flux profile along the evaporating meniscus for $w = 0.7$ mm at $t = 0.2$ s is markedly different from the others. Specifically, unlike the other cases the center of the meniscus is characterized by the minimum local heat flux. This anomaly is attributed to the overall downward motion of the flow at this time and the corresponding downward advection at cool liquid beneath the center of the meniscus (Fig. 4.10c), resulting in smaller temperature gradients near the middle of the meniscus zone. A similar phenomenon occurs for $w = 0.5$ mm at $t = 0.2$ s. However, since the liquid velocity is relatively small, thermal advection is not sufficiently strong to alter the shape of the heat flux distribution significantly.

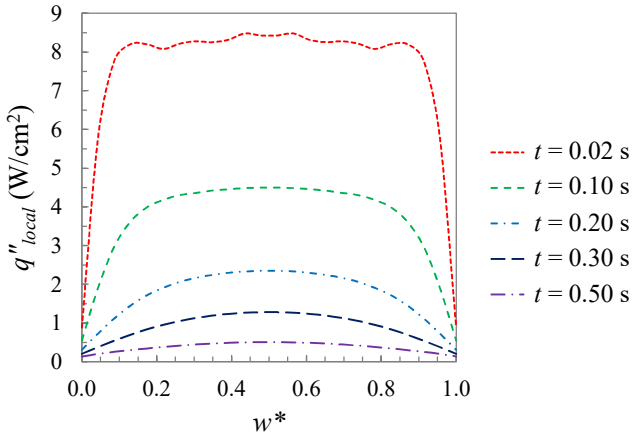

(a) w = 0.3 mm

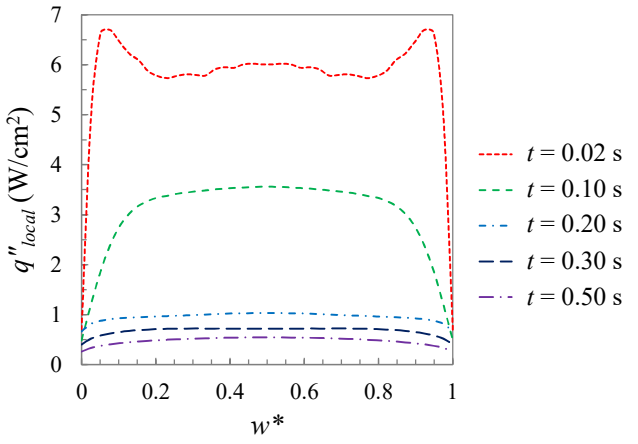

(b) w = 0.5 mm

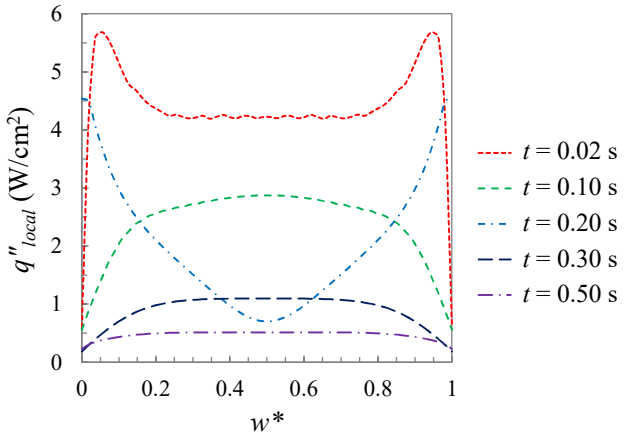

(c) w = 0.7 mm

Fig. 4.12 Computationally predicted local heat flux variations along the evaporating meniscus ($w^* = x/w$) for various wall spacings and ΔT = 2 K.

4.4.6 Transient Vapor Velocity

The y-velocity field near the evaporating meniscus in Ω_v for various wall spacings and $\Delta T = 2$ K at $t = 0.1$s is reported in Fig. 4.13. As noted previously, the evaporated liquid creates an upward laminar flow in the vapor subdomain independent of the flow direction of the liquid column. For all cases, it is evident that the velocity profile evolves to the fully-developed conditions relatively quickly and as the wall spacing increases, the maximum velocity at the core of the capillary channel decreases. The average vapor velocity is larger for smaller wall spacings.

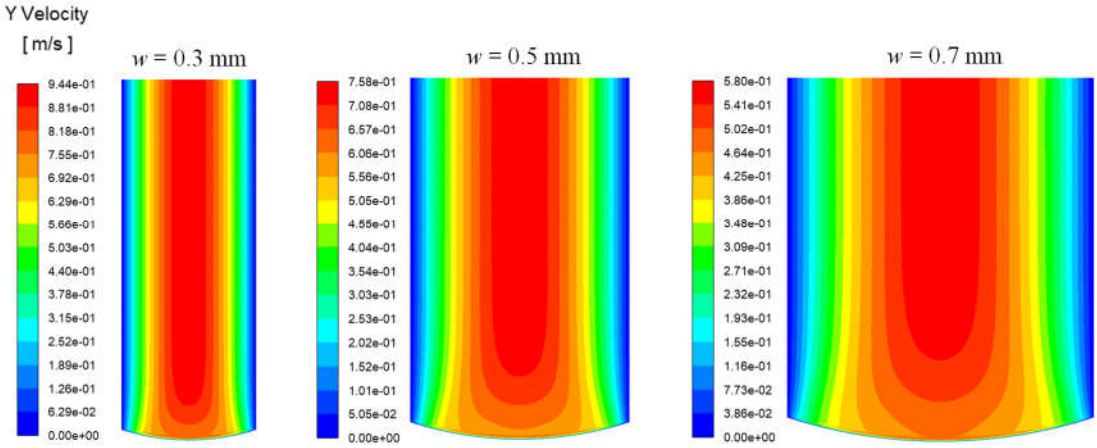

Fig. 4.13 The y-velocity field near the evaporating meniscus in Ω_v for various wall spacings and $\Delta T = 2$ K at $t = 0.1$ s.

4.4.7 Transient Pressure Response

It was noted in Section 4.3.3.1 that the pressure exerted on the meniscus by the vapor flow affects the capillary flow dynamics. The liquid column is pushed downward by the recoil pressure induced by the vapor that is ejected from the meniscus (Additional details regarding calculation of the recoil pressure were given in Section 2.3). In the

CFD model, in addition to the recoil force, the meniscus is subjected to a pressure that is built up at the bottom of the vapor domain to overcome viscous forces at the wall-vapor interface. Figure 3.14 shows the computationally predicted total pressure exerted by the vapor on the meniscus for various wall spacings and degrees of superheat. It can be seen that the increased superheat degree increases the vapor pressure on the meniscus due to the larger evaporation mass flow rates. Similar behavior was found for the other wall spacings. Besides, as the wall spacing increases, the total pressure exerted by the vapor decreases. It is worth noting that for the largest wall spacing of $w = 0.7$ mm, in which the flow exhibits oscillatory behavior, the pressure exerted by the vapor follows a similar oscillatory trend. In all cases, the pressure exerted by the vapor decreases over time due to decreasing evaporation rates. A comparison of Figs. 4.9 and 4.13 demonstrates a proportionality between the average heat flux reaching the meniscus and the pressure exerted by the vapor, which suggests that the contribution of the recoil force is small relative to that of the vapor drag force.

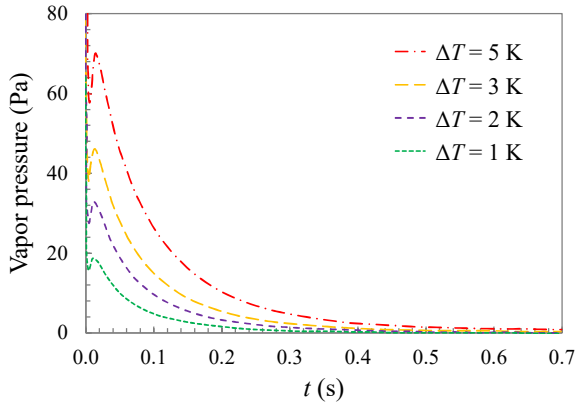

(a)

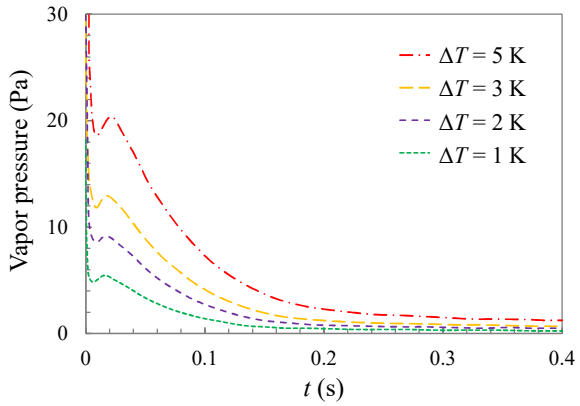

(b)

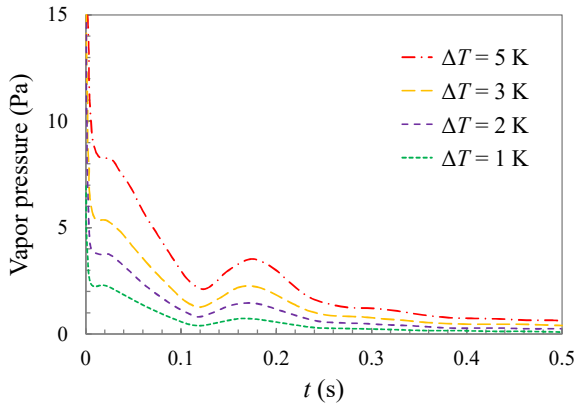

(c)

Fig. 4.14 Computationally predicted pressure exerted on the meniscus induced by the coupling of vapor recoil and vapor drag forces at various degrees of superheat for (a) w = 0.3 mm, (b) w = 0.5 mm, and w = 0.7 mm.

4.5 Conclusions

An arbitrary-Lagrangian-Eulerian computational model was developed to predict the dynamic response of an evaporating meniscus in the capillary flow of superheated liquids between vertical parallel plates. A dynamic mesh method was employed to directly predict the meniscus shape and to track its movement with no need for implicit interface tracking schemes. Several important physical phenomena, including thermal diffusion adjacent to the meniscus, depression of the capillary height due to the evaporation, and development of pressure exerted on the meniscus by the vapor ejected from the meniscus, are accounted for. Computational predictions were validated by comparison with those of the available theoretical model. It was shown that thermal diffusion in the vicinity of the evaporating meniscus plays an important role in the heat transfer process, and ignoring it leads to significant overprediction of the evaporation rate. A detailed parametric study was carried out to elucidate the effects of the wall spacing and superheat degrees on the dynamics of the evaporating meniscus. It was found that depression in the capillary height and the pressure exerted on the meniscus by the vapor both increase by increasing the superheat degree of the liquid. Further, as the wall spacing increases, the total pressure exerted by the vapor on the meniscus decreases. The findings of this study [98,99] provide fundamental insight into the dynamics of the evaporating liquid-vapor interfaces in capillary structures and might be used as a benchmark in further computational investigations.

CHAPTER 5: CONCLUDING REMARKS AND FUTURE WORK

5.1 Conclusions

The goal of this research was to develop a robust computational model to accurately simulate the dynamics of the transient process of meniscus formation and capillary flow between vertical parallel plates with and without phase change heat transfer.

In the first part of the study, a two-dimensional simulation model was developed in the arbitrary Lagrangian-Eulerian (ALE) framework. The model was capable of predicting the formation and evolution of the meniscus during spontaneous liquid penetration and depression within capillary channels of various widths.

In the second phase of the investigation, the previously developed ALE model was extended to directly track the formation and evolution of the evaporating meniscus during spontaneous liquid penetration in a capillary channel.

The commercial CFD Package ANSYS Fluent ver. 19.1 with the power of User Defined Functions was used to apply the numerical procedure such as (i) specification of the transient pressure boundary condition at the meniscus, (ii) meniscus movement in each time step, (iii) specification of the evaporation rate from the meniscus and the corresponding vapor generation, and (iv) keeping the meniscus temperature fixed and equal to the saturation temperature.

Also, the numerical procedure was validated against the available transient theoretical results for proposed model of capillary flow. It was followed by a thorough discussion of parametric studies carried out to illustrate the influence of effective parameters such as wall spacing, contact angle, and liquid superheat degree on the meniscus dynamics.

The devised numerical method was shown to perform well over the wide range of parameters of interest.

In the first part of this work, it was found that, as the wall spacing increased, the equilibrium height decreased and the time to reach equilibrium increased. The computational model was able to accurately predict the capillary penetration or depression regardless of the wall spacing, whereas the theoretical models fail to predict the dynamic response accurately for wider capillary channels. It was also shown that the meniscus shape deviated from circular arc as the wall spacing increased.

Moreover, in the second part of the study, it was shown that thermal diffusion in the vicinity of the evaporating meniscus plays an important role in the heat transfer process, and ignoring it leads to significant overprediction of the evaporation rate. It was also revealed that that depression in the capillary height and the pressure exerted on the meniscus by the vapor both increase by increasing the superheat degree of the liquid. Further, as the wall spacing increases, the total pressure exerted by the vapor on the meniscus decreases.

5.2 Recommendations for Future Work

The work presented in this dissertation can be expanded in the following areas.

5.2.1 Simulation of Dynamic Contact Angle

The current study does not include the effects of contact angle hysteresis. It is assumed that the contact angle between the liquid and solid surface is constant and equal to equilibrium contact angle. However, the dynamic contact angle is always larger/smaller

than its expected equilibrium value and depends extremely on the meniscus rising/falling velocity. In fact, the contact angle hysteresis at the three-phase meniscus contact line is influenced by both the meniscus velocity and the flow direction and plays a major role in meniscus dynamics, specifically when the meniscus is subject to phase change [100–102]. Since the dynamic behavior of meniscus is strongly sensitive to details of the dynamic contact angle, thus correlating continuous contact angle changes with the advancing/receding meniscus velocity during upward/downward motion of meniscus can capture more aspects of physics and improve the numerical accuracy in prediction of hydrodynamic and thermal characteristics near moving contact lines. This remains as an active future research area in the investigation of meniscus dynamics.

5.2.2 Simulation of Heated Capillary Walls

In the present model, adiabatic conditions are applied at the interior vertical wall surfaces of the capillary channel and the evaporation is driven by applying initial liquid superheats throughout the entire liquid subdomain, except at the meniscus boundary that is fixed at the saturation temperature. So, the surface tension along the meniscus was assumed to be constant. In general, surface tension depends on temperature, the surface tension will not be uniform if the temperature, along the liquid-vapor interface, is nonuniform. Therefore, considering capillary channel walls exposed to heat fluxes and consequently incorporation of the complex physical mechanism related to the temperature gradient from the capillary channel walls to the meniscus center ($d\sigma/dT$)

that results in thermocapillary Marangoni convection affect the dynamics of evaporating meniscus [103–105]. Due to Marangoni convection, the liquid in the lower surface tension region in the vicinity of the liquid-vapor interface will be pulled toward the region with higher surface tension. This would be an interesting open problem that can be investigated by taking the advantage of the sharp interface tracking method proposed by the current computational model having direct access to the flow variables and transport fluxes at the meniscus with no need for averaging techniques.

5.2.3 Prediction of the Equilibrium Time in Capillary Flow

Equilibrium time is an important operational parameter in the analysis of dynamic response of meniscus in capillary systems. One of the parameters that strongly affects the equilibrium time in a parallel plate configuration is the distance between the walls and as disused before, for larger spacings the theoretical models fail to predict the dynamic response accurately. To the best knowledge of the author, none of the studies comprehensively analyzed and reported the equilibrium time in a wide range of wall spacings that cover both monotonic and oscillatory regimes. Thus, further studies to achieve the optimal equilibrium time also remain to be explored.

LIST OF REFERENCES

[1] D.L. Hu, B. Chan, J.W.M. Bush, The hydrodynamics of water strider locomotion, Nature. 424 (2003) 663–666. https://doi.org/10.1038/nature01793.

[2] M.M.A. Shirazi, A. Kargari, A review on applications of membrane distillation (MD) process for wastewater treatment, J. Membr. Sci. Res. 1 (2015) 101–112. https://doi.org/10.22079/jmsr.2015.14472.

[3] S. Roh, D.P. Parekh, B. Bharti, S.D. Stoyanov, O.D. Velev, 3D Printing by Multiphase Silicone/Water Capillary Inks, Adv. Mater. 29 (2017) 1–7. https://doi.org/10.1002/adma.201701554.

[4] A. Faghri, Y. Zhang, Fundamentals of Multiphase Heat Transfer and Flow, 1st ed., Springer, Cham, 2020. https://doi.org/https://doi.org/10.1007/978-3-030-22137-9.

[5] Y.D. Shikhmurzaev, Capillary flows with forming interfaces, CRC Press, 2007.

[6] Y. Yuan, T.R. Lee, Surface science techniques, in: Surf. Sci. Tech., Springer, Berlin, Heidelberg, 2013: pp. 3–34. https://doi.org/10.1007/978-3-642-34243-1.

[7] T. Young, III. An essay on the cohesion of fluids, Philos. Trans. R. Soc. 95 (1805) 65–87. https://doi.org/https://doi.org/10.1098/rstl.1805.0005.

[8] P.-G. de Gennes, F. Brochard-Wyart, D. Quéré, Capillarity and Wetting Phenomena, 2004. https://doi.org/10.1007/978-0-387-21656-0.

[9] A.W. Adamson, Alice P. Gast, Physical Chemistry of Surfaces, 6th ed., John Wiley & Sons, Inc, 1967.

[10] D. Ahmad, I. van den Boogaert, J. Miller, R. Presswell, H. Jouhara, Hydrophilic and hydrophobic materials and their applications, Energy Sources, Part A

Recover. Util. Environ. Eff. 40 (2018) 2686–2725. https://doi.org/10.1080/15567036.2018.1511642.

[11] A.R. Alharbi, I.M. Alarifi, W.S. Khan, R. Asmatulu, I. Engineering, A.-Majmaah, P.O. Box, Highly Hydrophilic Electrospun Polyacrylonitrile / Polyvinypyrro- lidone Nanofibers Incorporated with Gentamicin as Filter Medium for Dam Water and Wastewater Treatment, J. Membr. Sep. Technol. 5 (2016) 38–56.

[12] M. Landeryou, Liquid uptake by fibrous absorbent materials, University of London, University College London, 2001.

[13] A.A. Jeje, Rates of spontaneous movement of water in capillary tubes, J. Colloid Interface Sci. 69 (1979) 420–429. https://doi.org/10.1016/0021-9797(79)90131-0.

[14] B.P.J. Shopovt, P.D. Minev, Interaction of a deformable bubble with a rigid wall at moderate Reynolds numbers, J. Fluid Mech. 219 (1990) 241–271. https://doi.org/https://doi.org/10.1017/S0022112090002932.

[15] C.W. Hirt, B.D. Nichols, Volume of fluid (VOF) method for the dynamics of free boundaries, J. Comput. Phys. 39 (1981) 201–225. https://doi.org/10.1016/0021-9991(81)90145-5.

[16] D. Gueyffier, J. Li, A. Nadim, R. Scardovelli, S. Zaleski, Volume-of-Fluid Interface Tracking with Smoothed Surface Stress Methods for Three-Dimensional Flows, J. Comput. Phys. 152 (1999) 423–456. https://doi.org/10.1006/jcph.1998.6168.

[17] D.L. Youngs, Time-dependent multimaterial flow with large fluid distortion, in:

Numer. Methods Fluid Dyn., Academic Press, Cambridge, 1982: pp. 273–285.

[18] M. Sussman, P. Smereka, S. Osher, A level set approach for computing solutions to incompressible two-phase flow, J. Comput. Phys. 114 (1994) 146–159. https://doi.org/10.1006/jcph.1994.1155.

[19] J.A. Sethian, Evolution, Implementation, and Application of Level Set and Fast Marching Methods for Advancing Fronts, J. Comput. Phys. 169 (2001) 503–555. https://doi.org/10.1006/jcph.2000.6657.

[20] K. Luo, C. Shao, M. Chai, J. Fan, Level set method for atomization and evaporation simulations, Prog. Energy Combust. Sci. 73 (2019) 65–94. https://doi.org/10.1016/j.pecs.2019.03.001.

[21] J. Donea, A. Huerta, J. Ponthot, A. Rodriguez-Ferran, Chapter 14: Arbitrary Lagrangian-Eulerian Methods, in: Encycl. Comput. Mech., 1st ed., Wiley, 2004: pp. 413–437. https://doi.org/https://onlinelibrary.wiley.com/doi/abs/10.1002/0470091355.ecm009.

[22] A. Masud, Effects of mesh motion on the stability and convergence of ALE based formulations for moving boundary flows, Comput. Mech. 38 (2006) 430–439. https://doi.org/10.1007/s00466-006-0062-9.

[23] ANSYS Fluent Theory Guide, Release 15, ANSYS Inc., USA, 2013. http://www.ansys.com.

[24] ANSYS Fluent User's Guide, Release 15, ANSYS Inc., USA, 2013. http://www.ansys.com.

[25] K. Riemslagh, J. Vierendeels, E. Dick, An arbitrary Lagrangian-Eulerian finite-

volume method for the simulation of rotary displacement pump flow, Appl. Numer. Math. 32 (2000) 419–433. https://doi.org/https://doi.org/10.1016/S0168-9274(99)00061-6.

[26] R. Lucas, Ueber das Zeitgesetz des kapillaren Aufstiegs von Flüssigkeiten, Kolloid-Zeitschrift. 23 (1918) 15–22. https://doi.org/10.1007/BF01461107.

[27] E.W. Washburn, The Dynamics of Capillary Flow, Phys. Rev. 17 (1921) 273. https://doi.org/https://doi.org/10.1103/PhysRev.17.273.

[28] S. Levine, P. Reed, E.J. Watson, G. Neale, A theory of the rate of rise of a liquid in a capillary, in: Colloid Interface Sci., Academic Press, 1976: pp. 403–419. https://doi.org/https://doi.org/10.1016/B978-0-12-404503-3.50048-3.

[29] A. Hamraoui, T. Nylander, Analytical approach for the Lucas-Washburn equation, J. Colloid Interface Sci. 250 (2002) 415–421. https://doi.org/10.1006/jcis.2002.8288.

[30] J.W. Bullard, E.J. Garboczi, Capillary rise between planar surfaces, Phys. Rev. E - Stat. Nonlinear, Soft Matter Phys. 79 (2009) 4–10. https://doi.org/10.1103/PhysRevE.79.011604.

[31] E.K. Rideal, CVIII. On the flow of liquids under capillary pressure, London, Edinburgh, Dublin Philos. Mag. J. Sci. 44 (1922) 1152–1159. https://doi.org/10.1080/14786441008634082.

[32] G. Ramon, A. Oron, Capillary rise of a meniscus with phase change, J. Colloid Interface Sci. 327 (2008) 145–151. https://doi.org/10.1016/j.jcis.2008.08.016.

[33] J.P. Burelbach, S.G. Bankoff, S.H. Davis, Nonlinear stability of evaporating/condensing liquid films, J. Fluid Mech. 195 (1988) 463–494.

https://doi.org/10.1017/S0022112088002484.

[34] A.H. Persad, C.A. Ward, Expressions for the evaporation and condensation coefficients in the Hertz-Knudsen relation, Chem. Rev. 116 (2016) 7727–7767. https://doi.org/10.1021/acs.chemrev.5b00511.

[35] M. Matsumoto, K. Yasuoka, Y. Kataoka, Molecular Simulation of Evaporation and Condensation, Fluid Phase Equilib. 104 (1995) 431–439. https://doi.org/https://doi.org/10.1016/0378-3812(94)02667-P.

[36] T. Tsuruta, H. Tanaka, T. Masuoka, Condensation/evaporation coefficient and velocity distributions at liquid-vapor interface, Int. J. Heat Mass Transf. 42 (1999) 4107–4116. https://doi.org/10.1016/S0017-9310(99)00081-2.

[37] E. Hernández-Baltazar, J. Gracia-Fadrique, Elliptic solution to the Young-Laplace differential equation, J. Colloid Interface Sci. 287 (2005) 213–216. https://doi.org/10.1016/j.jcis.2005.01.102.

[38] V.R. Lucas, Cleber das Zeitgesetz des kapillaren P, ufstiegs yon Fliissigkeiten., Kolloid-Zeitschrift. 23 (1918) 15–22.

[39] L.R. Fisher, P.D. Lark, An experimental study of the washburn equation for liquid flow in very fine capillaries, J. Colloid Interface Sci. 69 (1979) 486–492. https://doi.org/10.1016/0021-9797(79)90138-3.

[40] C.H. Bosanquet, LV. On the flow of liquids into capillary tubes , London, Edinburgh, Dublin Philos. Mag. J. Sci. 45 (1923) 525–531. https://doi.org/10.1080/14786442308634144.

[41] N. Fries, M. Dreyer, An analytic solution of capillary rise restrained by gravity, J. Colloid Interface Sci. 320 (2008) 259–263.

https://doi.org/10.1016/j.jcis.2008.01.009.

[42] G. Mason, N.R. Morrow, Capillary behavior of a perfectly wetting liquid in irregular triangular tubes, J. Colloid Interface Sci. 141 (1991) 262–274. https://doi.org/10.1016/0021-9797(91)90321-X.

[43] M. Dong, I. Chatzis, The imbibition and flow of a wetting liquid along the comers of a square capillary tube, J. Colloid Interface Sci. 172 (1995) 278–288. https://doi.org/https://doi.org/10.1006/jcis.1995.1253.

[44] N. Ichikawa, K. Hosokawa, R. Maeda, Interface motion of capillary-driven flow in rectangular microchannel, J. Colloid Interface Sci. 280 (2004) 155–164. https://doi.org/10.1016/j.jcis.2004.07.017.

[45] P.R. Waghmare, S.K. Mitra, A comprehensive theoretical model of capillary transport in rectangular microchannels, Microfluid. Nanofluidics. 12 (2012) 53–63. https://doi.org/10.1007/s10404-011-0848-8.

[46] V. Thammanna Gurumurthy, I. V. Roisman, C. Tropea, S. Garoff, Spontaneous rise in open rectangular channels under gravity, J. Colloid Interface Sci. 527 (2018) 151–158. https://doi.org/10.1016/j.jcis.2018.05.042.

[47] Z. Wu, Y. Huang, X. Chen, X. Zhang, Capillary-driven flows along curved interior corners, Int. J. Multiph. Flow. 109 (2018) 14–25. https://doi.org/10.1016/j.ijmultiphaseflow.2018.04.004.

[48] M. Dreyer, A. Delgado, H.J. Path, Capillary rise of liquid between parallel plates under microgravity, J. Colloid Interface Sci. 163 (1994) 158–168. https://doi.org/10.1006/jcis.1994.1092.

[49] F.G. Wolf, L.O.E. dos Santos, P.C. Philippi, Capillary rise between parallel

plates under dynamic conditions, J. Colloid Interface Sci. 344 (2010) 171–179. https://doi.org/10.1016/j.jcis.2009.12.023.

[50] P. Wu, H. Zhang, A. Nikolov, D. Wasan, Rise of the main meniscus in rectangular capillaries: Experiments and modeling, J. Colloid Interface Sci. 461 (2016) 195–202. https://doi.org/10.1016/j.jcis.2015.08.071.

[51] P.R. Waghmare, S.K. Mitra, On the derivation of pressure field distribution at the entrance of a rectangular capillary, J. Fluids Eng. Trans. ASME. 132 (2010) 0545021–0545024. https://doi.org/10.1115/1.4001641.

[52] Y. Xiao, F. Yang, R. Pitchumani, A generalized analysis of capillary flows in channels, J. Colloid Interface Sci. 298 (2006) 880–888. https://doi.org/10.1016/j.jcis.2006.01.005.

[53] D.L. Youngs, Time-dependent multi-material flow with large fluid distortion., Numer. Methods Fluid Dyn. (1982).

[54] D. Gaulke, M.E. Dreyer, CFD Simulation of Capillary Transport of Liquid Between Parallel Perforated Plates using Flow3D, Microgravity Sci. Technol. 27 (2015) 261–271. https://doi.org/10.1007/s12217-015-9449-6.

[55] F. Schönfeld, S. Hardt, Dynamic contact angles in CFD simulations, Comput. Fluids. 38 (2009) 757–764. https://doi.org/10.1016/j.compfluid.2008.05.007.

[56] A. Ashish Saha, S.K. Mitra, Effect of dynamic contact angle in a volume of fluid (VOF) model for a microfluidic capillary flow, J. Colloid Interface Sci. 339 (2009) 461–480. https://doi.org/10.1016/j.jcis.2009.07.071.

[57] A.A. Saha, S.K. Mitra, Numerical study of capillary flow in microchannels with alternate hydrophilic-hydrophobic bottom wall, J. Fluids Eng. Trans. ASME.

(2009). https://doi.org/10.1115/1.3129130.

[58] D. Gründing, M. Smuda, T. Antritter, M. Fricke, D. Rettenmaier, F. Kummer, P. Stephan, H. Marschall, D. Bothe, Capillary Rise -- A Computational Benchmark for Wetting Processes, (2019) 1–38. http://arxiv.org/abs/1907.05054.

[59] D. Gründing, An enhanced model for the capillary rise problem, Int. J. Multiph. Flow. 128 (2020) 103210. https://doi.org/10.1016/j.ijmultiphaseflow.2020.103210.

[60] C.W. Hirt, A.A. Amsden, J.L. Cook, An arbitrary Lagrangian-Eulerian computing method for all flow speeds, J. Comput. Phys. (1974). https://doi.org/10.1016/0021-9991(74)90051-5.

[61] M. Souli, D.J. Benson, Arbitrary Lagrangian-Eulerian and Fluid-Structure Interaction, 2013. https://doi.org/10.1002/9781118557884.

[62] H.H. Hu, N.A. Patankar, M.Y. Zhu, Direct Numerical Simulations of Fluid-Solid Systems Using the Arbitrary Lagrangian-Eulerian Technique, J. Comput. Phys. 169 (2001) 427–462. https://doi.org/10.1006/jcph.2000.6592.

[63] V.G. Stepanov, Wetting contact angles for some systems, Journals Eng. Phys. Thermophys. 32 (1977) 1000–1003.

[64] S. Goswami, S. Klaus, J. Benziger, Wetting and absorption of water drops on nafion films, Langmuir. 24 (2008) 8627–8633. https://doi.org/10.1021/la800799a.

[65] C. Huh, L.E. Scriven, Hydrodynamic model of steady movement of a solid/liquid/fluid contact line, J. Colloid Interface Sci. 35 (1971) 85–101. https://doi.org/10.1016/0021-9797(71)90188-3.

[66] S.L. Lee, H.D. Lee, Evolution of liquid meniscus shape in a capillary tube, J. Fluids Eng. 129 (2007) 957-965 (9 pages). https://doi.org/10.1115/1.2746898.

[67] S. V. Patankar, Numerical heat transfer and fluid flow., 1st ed., CRC Press, Taylor & Francis Group, Boca Raton, 1980. https://doi.org/https://doi.org/10.1201/9781482234213.

[68] J. Gaydos, The Laplace equation of capillarity, Stud. Interface Sci. (1998). https://doi.org/10.1016/S1383-7303(98)80018-5.

[69] A.A. Duarte, D.E. Strier, D.H. Zanette, The rise of a liquid in a capillary tube revisited: A hydrodynamical approach, Am. J. Phys. 64 (1996) 413–418. https://doi.org/10.1119/1.18256.

[70] D. Quéré, Inertial capillarity, Europhys. Lett. 39 (1997) 533–538. https://doi.org/10.1209/epl/i1997-00389-2.

[71] D. Quéré, É. Raphaël, J.Y. Ollitrault, Rebounds in a capillary tube, Langmuir. 15 (1999) 3679–3682. https://doi.org/10.1021/la9801615.

[72] R. Masoodi, E. Languri, A. Ostadhossein, Dynamics of liquid rise in a vertical capillary tube, J. Colloid Interface Sci. 389 (2013) 268–272. https://doi.org/10.1016/j.jcis.2012.09.004.

[73] R.H. Rand, Fluid mechanics of green plants., Annu. Rev. Fluid Mech. 15 (1983) 29–45.

[74] J. Lee, T. Laoui, R. Karnik, Nanofluidic transport governed by the liquid/vapour interface, Nat. Nanotechnol. 9 (2014) 317–323. https://doi.org/10.1038/nnano.2014.28.

[75] V.P. Carey, Liquid-vapor phase-change phenomena: an introduction to the

thermophysics of vaporization and condensation processes in heat transfer equipment, 3rd ed., CRC Press, Taylor & Francis Group, Boca Raton, 2020. https://doi.org/https://doi.org/10.1201/9780429082221.

[76] G. Yarin, L. P., Mosyak, A., Hetsroni, Fluid Flow, Heat Transfer and Boiling in Micro-Channels, 1st ed., Springer, Berlin, Heidelberg, 2009. https://doi.org/10.1007/978-3-540-78755-6.

[77] B. Zhao, J.S. Moore, D.J. Beebe, Surface-directed liquid flow inside microchannels, J. Sci. 291 (2001) 1023–1026. https://doi.org/10.1126/science.291.5506.1023.

[78] J. Szekely, A.W. Neumann, Y.K. Chuang, The rate of capillary penetration and the applicability of the Washburn equation, J. Colloid Interface Sci. 35 (1971) 273–278. https://doi.org/10.1016/0021-9797(71)90120-2.

[79] S. Levine, J. Lowndes, E.J. Watson, G. Neale, A theory of capillary rise of a liquid in a vertical cylindrical tube and in a parallel-plate channel. Washburn equation modified to account for the meniscus with slippage at the contact line, J. Colloid Interface Sci. 73 (1980) 136–151. https://doi.org/10.1016/0021-9797(80)90131-9.

[80] Q. Wang, L. Li, J. Gu, N. Weng, A dynamic model for the oscillatory regime of liquid rise in capillaries, Chem. Eng. Sci. 209 (2019) 115220. https://doi.org/10.1016/j.ces.2019.115220.

[81] R.H. Rand, The dynamics of an evaporating meniscus, Acta Mech. 29 (1978) 135–146. https://doi.org/10.1007/BF01176632.

[82] R.W. Schrage, A Theoretical Study of Interphase Mass Transfer, Columbia

University Press, New York Chichester, West Sussex, 1953. https://doi.org/10.7312/schr90162.

[83] S. Sánchez, F. Méndez, O. Bautista, Capillary rise in a circular tube with interfacial condensation process, Int. J. Therm. Sci. 50 (2011) 2422–2429. https://doi.org/10.1016/j.ijthermalsci.2011.07.005.

[84] J. Polansky, T. Kaya, An experimental and numerical study of capillary rise with evaporation, Int. J. Therm. Sci. 91 (2015) 25–33. https://doi.org/10.1016/j.ijthermalsci.2014.12.020.

[85] A.M. Benselama, A. Voirand, Y. Bertin, Electric and capillary instability of liquid rising between heated/cooled parallel plates and subjected to phase change: DC on perfect dielectric liquids, Colloids Surfaces A Physicochem. Eng. Asp. 556 (2018) 167–176. https://doi.org/10.1016/j.colsurfa.2018.08.003.

[86] M. Rao, F. Lefèvre, S. Khandekar, J. Bonjour, Understanding transport mechanism of a self-sustained thermally driven oscillating two-phase system in a capillary tube, Int. J. Heat Mass Transf. 65 (2013) 451–459. https://doi.org/10.1016/j.ijheatmasstransfer.2013.05.067.

[87] D.S. Antao, S. Adera, Y. Zhu, E. Farias, R. Raj, E.N. Wang, Dynamic Evolution of the Evaporating Liquid-Vapor Interface in Micropillar Arrays, Langmuir. 32 (2016) 519–526. https://doi.org/10.1021/acs.langmuir.5b03916.

[88] K.A. Brakke, The surface evolver, Exp. Math. 1 (1992) 141–165. https://doi.org/10.1080/10586458.1992.10504253.

[89] S. Soma, T. Kunugi, Water evaporation in parallel plates, Int. J. Heat Mass Transf. 110 (2017) 778–782.

https://doi.org/10.1016/j.ijheatmasstransfer.2017.03.085.

[90] S. Soma, T. Kunugi, Theoretical scaling law for predicting evaporation rate from meniscus, Int. J. Heat Mass Transf. 134 (2019) 143–148. https://doi.org/10.1016/j.ijheatmasstransfer.2019.01.032.

[91] S.M. Smith, B.S. Taft, J. Moulton, Contact angle measurements for advanced thermal management technologies, Front. Heat Mass Transf. 5 (2014). https://doi.org/10.5098/hmt.5.6.

[92] R. Ranjan, J.Y. Murthy, S. V. Garimella, A microscale model for thin-film evaporation in capillary wick structures, Int. J. Heat Mass Transf. 54 (2011) 169–179. https://doi.org/10.1016/j.ijheatmasstransfer.2010.09.037.

[93] M. Naghashnejad, H. Shabgard, T. Bergman, Computational Simulation of Spontaneous Liquid Penetration and Depression Between Vertical Parallel Plates, J. Fluids Eng. 143 (2021) 051302 (11 pages). https://doi.org/10.1115/1.4049683.

[94] M. Naghashnejad, H. Shabgard, NUMERICAL ANALYSIS OF THE TRANSIENT LIQUID RISE WITHIN A CAPILLARY CHANNEL, in: 5th-6th Therm. Fluids Eng. Conf., 2021: pp. 269–278. https://doi.org/http://dx.doi.org/10.1615/TFEC2021.cmd.036699.

[95] S. Raja, K.T. Valsaraj, Uptake of aromatic hydrocarbon vapors (benzene and phenanthrene) at the air-water interface of micron-size water droplets, J. Air Waste Manag. Assoc. 54 (2004) 1550–1559. https://doi.org/10.1080/10473289.2004.10471013.

[96] P.L. Barclay, J.R. Lukes, Curvature dependence of the mass accommodation coefficient, Langmuir. 35 (2019) 6196–6202.

https://doi.org/10.1021/acs.langmuir.9b00537.

[97] R. Marek, J. Straub, Analysis of the evaporation coefficient and the condensation coefficient of water, Int. J. Heat Mass Transf. 44 (2001) 39–53. https://doi.org/https://doi.org/10.1016/S0017-9310(00)00086-7.

[98] M. Naghashnejad, H. Shabgard, H. Rahimi, NUMERICAL MODELING OF EVAPORATING MENISCUS IN A PARALLEL-PLATE CHANNEL, in: 5th-6th Therm. Fluids Eng. Conf., 2021: pp. 281–290. https://doi.org/http://dx.doi.org/10.1615/TFEC2021.cmd.036700.

[99] M. Naghashnejad, H. Shabgard, T.L. Bergman, A Novel Computational Model of the Dynamic Response of the Evaporating Liquid-Vapor Interface in a Capillary Channel, Submitt. to Interanational J. Heat Mass Transf. (2021).

[100] T.S. Jiang, O.H. Soo-Gun, J.C. Slattery, Correlation for dynamic contact angle, J. Colloid Interface Sci. 69 (1979) 74–77. https://doi.org/10.1016/0021-9797(79)90081-X.

[101] P. Joos, P. Van Remoortere, M. Bracke, The kinetics of wetting in a capillary, J. Colloid Interface Sci. 136 (1990) 189–197. https://doi.org/10.1016/0021-9797(90)90089-7.

[102] J.E. Seebergh, J.C. Berg, Dynamic wetting in the low capillary number regime, Chem. Eng. Sci. 47 (1992) 4455–4464. https://doi.org/10.1016/0009-2509(92)85123-S.

[103] C. Buffone, K. Sefiane, Controlling evaporative thermocapillary convection using external heating: An experimental investigation, Exp. Therm. Fluid Sci. 32 (2008) 1287–1300. https://doi.org/10.1016/j.expthermflusci.2008.02.009.

[104] H. Wang, J.Y. Murthy, S. V. Garimella, Transport from a volatile meniscus inside an open microtube, Int. J. Heat Mass Transf. 51 (2008) 3007–3017. https://doi.org/10.1016/j.ijheatmasstransfer.2007.09.011.

[105] H.K. Dhavaleswarapu, J.Y. Murthy, S. V. Garimella, Numerical investigation of an evaporating meniscus in a channel, Int. J. Heat Mass Transf. 55 (2012) 915–924. https://doi.org/10.1016/j.ijheatmasstransfer.2011.10.017.